The New (g – 2) Experiment:

A Proposal to Measure the Muon Anomalous Magnetic Moment to ±0.14 ppm Precision

Submitted to the DOE Office of High Energy Physics

April 5, 2010

New (g – 2) Collaboration

The New $g-2$ Experiment: A Proposal to Measure the Muon Anomalous Magnetic Moment to ± 0.14 ppm Precision

New $g-2$ Collaboration: R.M. Carey[1], K.R. Lynch[1], J.P. Miller[1], B.L. Roberts[1], W.M. Morse[2], Y.K. Semertzidis[2], V.P. Druzhinin[3], B.I. Khazin[3], I.A. Koop[3], I. Logashenko[3], S.I. Redin[3], Y.M. Shatunov[3], E.P. Solodov[3], Y. Orlov[4], R.M. Talman[4], B. Casey[5], B. Drendel[5], K. Genser[5], J. Johnstone[5], A. Jung[5], D. Harding[5], A. Klebaner[5], A. Leveling[5], J-F. Ostiguy[5], N.V. Mokhov[5], J. P. Morgan[5], V. Nagaslaev[5], D. Neuffer[5], A. Para[5], C.C. Polly[5], M. Popovic[5], M. Rominsky[5], A. Soha[5], P. Spentzouris[5], S.I. Striganov[5], M.J. Syphers[5], G. Velev[5], S. Werkema[5], F. Happacher[6], G. Venanzoni[6], M. Martini[6], D. Moricciani[7], J.D. Crnkovic[8], P.T. Debevec[8], M. Grosse-Perdekamp[8], D.W. Hertzog[8], P. Kammel[8], N. Schroeder[8], P. Winter[8], K.L. Giovanetti[9], K. Jungmann[10], C.J.G. Onderwater[10], N. Saito[11], C. Crawford[12], R. Fatemi[12], T.P. Gorringe[12], W. Korsch[12], B. Plaster[12], V. Tishchenko[12], D. Kawall[13], T. Chupp[14], R. Raymond[14], B. Roe[14], C. Ankenbrandt[15], M.A Cummings[15], R.P. Johnson[15], C. Yoshikawa[15], A. de Gouvêa[16], T. Itahashi[17], Y. Kuno[17], G.D. Alkhazov[18], V.L. Golovtsov[18], P.V. Neustroev[18], L.N. Uvarov[18], A.A. Vasilyev[18], A.A. Vorobyov[18], M.B. Zhalov[18], F. Gray[19], D. Stöckinger[20], S. Baeßler[21], M. Bychkov[21], E. Frlež[21], and D. Počanić[21]

[1]Department of Physics, Boston University, Boston, MA 02215, USA

[2]Brookhaven National Laboratory, Upton, NY 11973, USA

[3]Budker Institute of Nuclear Physics, 630090 Novosibirsk, Russia

[4]Newman Laboratory, Cornell University, Ithaca, NY 14853, USA

[5]Fermi National Accelerator Laboratory, Batavia, IL 60510, USA

[6]Laboratori Nazionali di Frascati, INFN, I-00044 Frascati (Rome), Italy

[7]Dipartimento di Fisica dell'Università di Roma "Tor Vergata" and INFN Sezione di Roma Tor Vergata, Roma, Italy

[8]Department of Physics, University of Illinois, Urbana-Champaign, IL 61801, USA

[9]Department of Physics, James Madison University, Harrisonburg, VA 22807, USA

[10]Kernfysisch Versneller Instituut, University of Groningen, NL-9747 AA Groningen, The Netherlands
[11]KEK, High Energy Accelerator Research Organization, Tsukuba, Ibaraki 305-0801, Japan
[12]Department of Physics, University of Kentucky, Lexington, Ky 40506, USA
[13]Department of Physics, University of Massachusetts, Amherst, MA 01003, USA
[14]Physics Department, University of Michigan, Ann Arbor, MI 48109, USA
[15]Muons, Inc., Batavia, IL 60510, USA
[16]Physics & Astronomy Department, Northwestern University, Evanston, IL 60208, USA
[17]Department of Physics, Osaka University, Toyonaka, Osaka 560-0043, Japan
[18]Petersburg Nuclear Physics Institute, Gatchina 188350, Russia
[19]Department of Physics and Computational Science, Regis University, Denver, CO 80221, USA
[20]Technische Universität Dresden, Institut für Kern- und Teilchenphysik, D-01062 Dresden, Germany
[21]Department of Physics, The University of Virginia, Charlottesville, VA 22904, USA

Contactpersons: David W. Hertzog (hertzog@illinois.edu, 217-333-3988)
B. Lee Roberts (roberts@bu.edu, 617-353-2187)

Abstract

We propose to measure the muon anomalous magnetic moment, a_μ, to 0.14 ppm—a fourfold improvement over the 0.54 ppm precision obtained in the Brookhaven E821 experiment. The muon anomaly is a fundamental quantity and its precise determination will have lasting value. The current measurement was statistics limited, suggesting that greater precision can be obtained in a higher-rate, next-generation experiment. We outline a plan to use the unique Fermilab complex of proton accelerators and rings to produce high-intensity bunches of muons, which will be directed into the relocated BNL muon storage ring. The goal of our experiment is a precision on the muon anomaly of 16×10^{-11}, which will require 21 times the statistics of the BNL measurement, as well a factor of 3 reduction in the overall systematic error. Our goal is well matched to anticipated advances in the worldwide effort to determine the standard model (SM) value of the anomaly. The present comparison, $\Delta a_\mu(\text{Expt.} - \text{SM}) = (255 \ \pm \ 80) \ \times \ 10^{-11}$, is already suggestive of possible new physics. Assuming that the current theory error of 49×10^{-11} is reduced to 30×10^{-11} on the time scale of the completion of our experiment, a future Δa_μ comparison would have a combined uncertainty of $\approx 34 \times 10^{-11}$. That would result in a 7.5σ deviation from the SM if the central value remained unchanged. In any case, a_μ will be a sensitive and complementary benchmark for proposed standard model extensions. The experimental data acquired in this effort will also be used to improve the muon EDM limit by up to a factor of 100 and it can be used to make a higher-precision test of Lorentz and CPT violation.

We describe in this Proposal why the Fermilab complex provides a unique and ideal facility for a next-generation $g-2$ experiment. The experiment is compatible with the fixed-target neutrino program; indeed, it requires only the unused Booster batch cycles and can acquire the desired statistics in less than two years of running. The proton beam preparations are largely aligned with the new Mu2e requirements and completion of these preparations for $g-2$ will be mutually beneficial. The $g-2$ experiment itself is based on the solid foundation of E821 at BNL, with modest improvements related to systematic error reduction. We outline the motivation, conceptual plans, and details of the project elements, a completed budget exercise, and an updated timeline in this proposal.

Contents

I. EXTENDED EXECUTIVE SUMMARY

The muon anomalous magnetic moment a_μ is a low-energy observable, which can be both measured and computed to high precision. The comparison between experiment and the standard model (SM) therefore provides a sensitive search for new physics. At present, both measurement and theory have sub-part-per-million (ppm) uncertainties, and the "$g-2$ test" is being used to constrain standard model extensions. As described below, the difference between experiment and theory, $\Delta a_\mu(\text{Expt} - \text{SM}) = (255 \pm 80) \times 10^{-11}$ (3.2 σ), is a highly cited result and a possible harbinger of new TeV-scale physics. Potential explanations of the deviation include: supersymmetry, lepton substructure, dark matter loop effects etc., all well motivated by theory and consistent with other experimental constraints. Fermilab Proposal-989 describes a plan to reduce the experimental uncertainty by a factor of 4 or more. This reduction will lead to a more definitive result—a $> 5\sigma$ "discovery-level" deviation from the SM—if the central value remains unchanged. A precise $g-2$ test, no matter where the final value lands, will sharply discriminate among models and will enter as one of the central observables in a global analysis of any New Standard Model extension. This Proposal describes a credible plan that can achieve this goal in a timely and cost-efficient manner. It is anchored by the re-use of the existing precision muon storage ring, an efficient and parasitic use of the Fermilab proton complex, and it will be carried out by an experienced collaboration. During the same time period required to mount, run and analyze the New $g-2$ Experiment, a vigorous worldwide effort to reduce the uncertainty on the SM contributions will continue.

P-989 was presented to the Fermilab Program Advisory Committee (PAC) in March 2009. They endorsed the physics case and recommended an independent assessment of the costs, which was completed under the leadership of Ron Ray at Fermilab. Following their report, the Collaboration, supported by the Fermilab Directorate, embarked on specific studies that most affected the budgeting estimates. These included a full Conventional Facilities design by FESS, for siting of the storage ring, and a joint University-Fermilab effort to evaluate the accelerator implications and costs. In the fall of 2009, these tasks were completed and the *Design and Cost Update for Proposal P-989* report was submitted to the PAC, and presented to them in November. The PAC reaffirmed the interest in the physics and concluded that the experiment "meets the criteria for Stage-1 approval." The PAC further recommended that

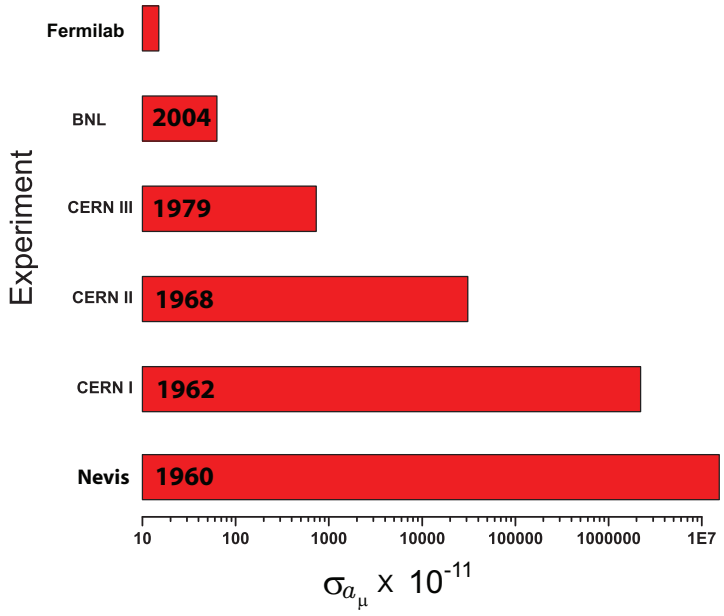

FIG. 1: Graphical display of the achieved uncertainties in the measurement of the muon anomaly, beginning with the Nevis lab experiment in 1960. The goal of our Fermilab experiment improves on the Brookhaven result by a factor of 4.

"the Laboratory clarify with the DOE the prospects for obtaining support for P-989." The PAC reports and the Directorate letters are attached in Appendix A. In February, Roberts and Hertzog presented an update to the DOE Office of High-Energy Physics, and also to the NSF, who are expected to partner in the support of specific experimental equipment and participating groups. The present proposal is intended to gather the latest technical and budget information and to sharpen the physics motivation.

In this Extended Summary, we describe the Experimental Goal, the Standard Model Status, the Physics Motivation, the Experimental Method, and the Budget, Collaboration and Timeline for the project. It does not replace the main body of the Proposal and the Appendices, which provide significantly more detailed discussions.

A. Experimental Goal

The measurement of the muon anomaly has steadily improved over more than five decades, with increased experimental precision being matched by commensurate advances in theory. Figure 1 shows the evolution in the reduction of uncertainty, along with the new goal

for our proposed Fermilab experiment. The current experimental uncertainty—determined by Brookhaven E821—has an uncertainty of 63×10^{-11} (0.54 ppm), which is dominated by the statistical error (0.46 ppm). This suggests that a further increase in precision is possible if a higher integrated number of stored muons can be obtained. We propose to measure a_μ at Fermilab to an uncertainty of 16×10^{-11} (0.14 ppm), derived from a 0.10 ppm statistical sample and roughly equal 0.07 ppm systematic uncertainties from the measurement of the magnetic field and from the measurement of the muon precession frequency. Twenty-one times more events are required compared to E821, which completed its data taking in 2001. Our proposal efficiently uses the unique properties of the Fermilab beam complex—parasitically to the high-energy neutrino program—to produce the necessary flux of muons, which will be injected and stored in the (relocated) muon storage ring. In less than two years of running, the statistical goal can be achieved for positive muons. A follow-up run using negative muons is possible, depending on future scientific motivation. Two additional physics results will be obtained from the same data: a new limit on the muon's electric dipole moment (up to 100 times better); and, a more stringent limit on possible CPT or Lorentz violation in muon spin precession. A technically driven schedule permits data taking to begin by the end of 2014.

To achieve a statistical uncertainty of 0.1 ppm, the total data set must contain more than 1.8×10^{11} detected positrons with energy greater than 1.8 GeV, and arrival time greater than 30 μs after injection into the storage ring. The plan uses 6 out of 20 of the 8-GeV Booster proton batches in 15 Hz operational mode, each subdivided into four bunches of intensity 10^{12} p/bunch. The proton bunches fill the muon storage ring at a repetition rate of 18 Hz, to be compared to the 4.4 Hz at BNL. The proton bunch hits a target in the antiproton area, producing a 3.1 GeV/c pion beam that is directed along a 900 m decay line. The resulting pure muon beam is injected into the storage ring. The full statistics, plus commissioning time and systematic study runs, will require 4×10^{20} protons on target (POT), an easily achievable goal at present accelerator complex intensities.

Commensurate with the reduction in statistical error is a plan to reduce the systematic uncertainties associated with the determination of both the muon-averaged magnetic field, ω_p, and the muon precession frequency, ω_a. The magnetic field uncertainty is tied to the quality of the shimming of the magnet and the procedure to monitor and measure the field *in situ*. The already impressive 0.17 ppm uncertainty obtained at Brookhaven can

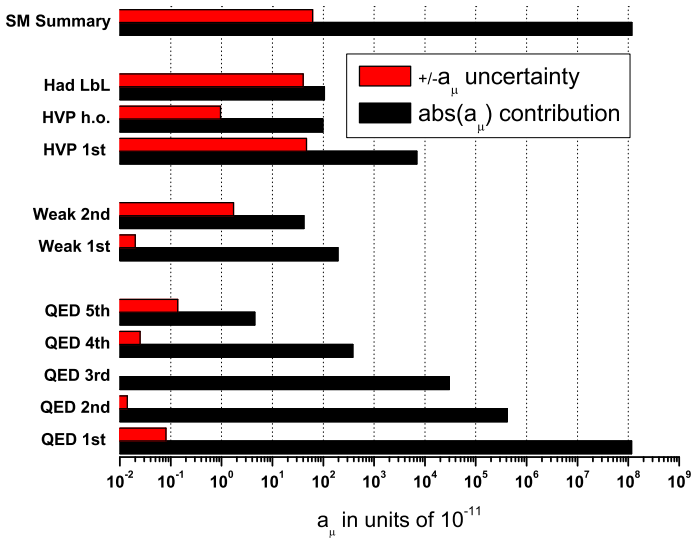

FIG. 2: Summary of standard model contributions (black) and their uncertainties (red) for QED, weak, and hadronic terms, order by order.

be further improved in a straight-forward manner following tested procedures and using existing shimming tools. The reduction in the precession frequency systematic uncertainties must address the "hadronic flash" at injection, effects related to coherent beam motion in the storage ring, and the control of pileup. At Fermilab, the longer decay beamline is central to the reduction of the background hadronic flash; an improved storage ring kicker is aimed at minimizing stored beam motions; and, the higher storage ring fill frequency and the segmentation of the electromagnetic calorimeters will reduce pileup.

B. Standard Model Status

The standard model (SM) theory for the muon $(g-2)$ involves QED, weak-interaction, and hadronic loops. Figure 2 displays the relative size of the contributions order-by-order, and the uncertainty that now exists on each term. The QED and weak loops have been calculated to very high precision; consequently, the uncertainty on these terms is negligible. A summary is given in [1] and [2].

Loops involving strongly interacting particles are less well known, with present uncertainties being only slightly smaller than experiment. Leading-order hadronic vacuum polariza-

tion (HVP) can be determined from ($e^+e^- \to$ hadrons) cross section data using a dispersion relation, and in principle, from hadronic tau decays. The latter requires significant isospin corrections, which remain somewhat uncertain (see Ref. [3] for an update). Since the publication of the final E821 result, high-statistics e^+e^--based data sets have been acquired and analyzed by the KLOE and BaBar collaborations using the initial-state-radiation (ISR) technique, and by the SND and CMD-II collaborations using the energy-scan method. While the key improvements have been in the dominant low-energy $\pi\pi$ channel, the higher-energy multi-hadron channels are also important; many of these channels are now measured well by the BaBar Collaboration. Although the multi-hadron channels represent a small absolute contribution to $a_\mu^{\rm HVP}$, their rather imprecise determination gives rise to a significant fraction of the overall hadronic uncertainty. The February 2010 HVP evaluation by Davier et al [4] is the most complete effort to data, giving $a_\mu^{\rm HVP} = (6955 \pm 41) \times 10^{-11}$ (0.35 ppm). It is based on a global average incorporating direct-scan measurements by CMD2 [5] and SND [6], along with ISR-based measurements by KLOE [7] and BaBar [8]. The HVP uncertainty will be reduced in the $\pi\pi$ channel when the analyses of the two additional large data sets from KLOE and BaBar are completed. Additionally, new efforts such as the recently commissioned VEPP-2000 collider at Novosibirsk, and its updated CMD and SND detectors, will combine direct-scan and ISR data over a large kinematic region, using the same detectors, to enable a next-generation measurement with even better precision. Multi-hadron channels also continue to be analyzed at BaBar and at Belle, with the aim to reduce specific final-state uncertainties even further. We anticipate approximately halving the overall error from the leading-order HVP over the time period of our experiment from a combination of these efforts.

The hadronic light-by-light (HLbL) contribution has been studied by a number of authors over the past twenty years. Two years ago, Prades, deRafael and Vainshtein (PdeRV)—representing most of the major theoretical collaborations that have worked on this problem—came together to work through the details of their respective calculations, and produced a joint paper [10] with agreement on the value of the HLbL contribution. One of the important points that they make is that the main physics of the HLbL scattering is well understood. In fact, they point out "but for the sign error unraveled in 2002, the theoretical predictions for $a_\mu^{\rm HLbL}$ have been relatively stable over more than ten years." The collaborative work of PdeRV finds $a_\mu^{\rm HLbL} = (105 \pm 26) \times 10^{-11}$ (0.22 ppm). Other theorists who have worked on

this problem, while in agreement with the size of the contribution, quote estimates on the uncertainty that are somewhat larger. A dedicated theoretical Workshop is being planned, likely at the Institute for Nuclear Theory at the University of Washington, to facilitate communication and discussion between all principle parties. The aim of the Workshop will be to forge a path forward in improving our understanding of the HLbL terms, incorporating future experimental and computational inputs. Besides the analytical efforts, several groups have begun lattice-based computations that—on the timescale of the new experiment—have a good chance of being competitive. From the experimental side, new information could come from Frascati. The KLOE experiment at DAFNE, which is expected to take data in a few months, is going to be instrumented with new tagging detectors to measure the cross section $\gamma^*\gamma^* \to hadrons$. These detectors will permit measurement of the same cross section in the case in which one of the two photons is off-shell. The case of both photons off-shell will be studied as well. DAFNE will contribute in a unique way to determine the meson transition form factor in a region where few data are available. These measurements will be of primary importance to reduce the uncertainties on the model-dependent calculations of the HLBL contribution to a_μ.

A summary of the standard model values is given in Table VI. It is to be compared with the combined a_μ^+ and a_μ^- values from E821 [11], where we have adjusted the result slightly owing to an improved value for the muon-to-proton magnetic moment ratio—which enters the extraction of a_μ from the measured quantities—as recommended by the CODATA group [12]:

$$a_\mu^{\rm E821} = (116\,592\,089 \pm 63) \times 10^{-11} \quad (0.54\,{\rm ppm}) \tag{1}$$

$$a_\mu^{\rm SM} = (116\,591\,834 \pm 49) \times 10^{-11}\,(0.44\,{\rm ppm}) \tag{2}$$

which give a difference of

$$\Delta a_\mu({\rm E821} - {\rm SM}) = (255 \pm 80) \times 10^{-11}\,. \tag{3}$$

C. Physics Motivation

Since the development of the standard model (SM) more than 30 years ago, arguments have been put forward that the SM should be replaced by a better theory at the elec-

TABLE I: Standard model contributions to the muon anomaly. Updated includes the recent HVP evaluation and recommendation in [4] and the HLbL recommendation in [10].

Contribution	Result in 10^{-11} units
QED (leptons)	$11\,6584\,718.09 \pm 0.14 \pm 0.04_{\alpha}$
HVP(lo)	$6\,955 \pm 40_{\rm exp} \pm 7_{\rm QCD}$
HVP(ho)	$-97.9 \pm 0.9_{\rm exp} \pm 0.3_{\rm rad}$
HLbL	105 ± 26
EW	$154 \pm 2 \pm 1$
Total SM	$116\,591\,834 \pm 49$

troweak/TeV scale. The era has begun where this energy scale will be probed directly by experiments at the LHC. These experiments are in a good position to discover the signatures of beyond the standard model (BSM) physics at the TeV scale and we certainly look forward to their findings. How might a precision measurement program add to this effort? And, in particular, how might an improved $g-2$ measurement contribute?

Two likely scenarios are possible, which demonstrate that doing the new $g-2$ measurement provides a win-win situation. (1) If the LHC finds BSM physics soon, one will need to pin down the detailed properties of the new physics. The new $g-2$ measurement will constitute an indispensable tool for this. It is well established that $g-2$ is sensitive to other parameters (in SUSY for example, to very central ones) than the LHC or those probed by other precision frontier experiments. (2) If the LHC does not find BSM physics after acquiring a large data sample and, for example, "only" discovers what appears to be a standard model Higgs boson, precision measurements of the muon $g-2$ might still reveal new physics at the weak scale that escaped the LHC lens.

Different BSM scenarios predict a wide range of contributions to $g-2$ even in cases where the LHC signatures are similar—hence, a precise $g-2$ determination provides a benchmark, which will discriminate between possible BSM scenarios. SUSY, Randall-Sundrum and several other scenarios can lead to significant contributions; whereas for example universal extra dimensions (UED) or the Littlest Higgs model with T-parity (LHT) cannot. Exam-

ples of models that are hard to distinguish at the LHC are SUSY versus UED or SUSY versus LHT, or different manifestations of supersymmetry having similar masses but different sgn(μ) or tan(β)—the latter two parameters are related to the SUSY Higgs sector and thus central to understanding electroweak symmetry breaking. For SUSY versus UED or LHT, the expected contributions to $g-2$ are so different that the final $g-2$ test provides a clear distinction. Within SUSY scenarios, it has been shown that even with 300 fb^{-1} luminosity, the LHC may not be sufficient to determine sgn(μ) and tan(β) with satisfactory precision [9]. However, the new $g-2$ measurement can establish sign(μ) unambiguously and improve the precision of tan(β) by a factor four.

Searches for charged lepton flavor violation (CLFV) processes, especially $\mu \to e$ conversion in nuclei, share some of the advantages of precision measurements of $g-2$. Indeed, searches for $\mu \to e$ conversion might be sensitive to new physics at energy scales significantly above the weak scale, which is not the case of precision measurements like muon $g-2$. On the other hand, searches for CLFV are sensitive to both the scale of the new physics—how heavy are the new degrees of freedoms—*and* to the flavor-violating character of the new physics—whether the new physics interactions can convert, for example, a muon to an electron. Positive evidence for CLFV can be interpreted as a consequence of very heavy new physics (perhaps above 10 TeV) that violates flavor very strongly or of electroweak-scale new physics ($\sim$ 500 GeV) that is only weakly flavor violating—the case for electroweak interactions. Under these circumstances, the muon $g-2$ measurement, along with results from the LHC, will be necessary to disentangle the nature of the new physics. Note that the same argument holds for searches for CP-violation (including EDM's) and precision studies of flavor-violating processes in the quark sector, B-factory observables, searches for $K \to \pi\nu\bar{\nu}$ and so on.

The main motivation for a new muon $g-2$ experiment is the following: The understanding of new phenomena that may be discovered at the LHC will require input from a variety of non-LHC experiments. The muon anomaly is already providing critical input and sets strong constraints on standard model extensions. An established technique, an experienced team, and an ideal laboratory opportunity exist. They will combine to increase the precision on $g-2$ by a factor of 4 or more, which will provide a very sharp and timely constraint on establishing a New Standard Model.

D. Experimental Method

The experiment will be performed by injecting polarized muons into the storage ring—relocated from BNL to Fermilab—and observing the spin precession. The directly measured quantities are the anomalous precession frequency ω_a—the difference frequency between the spin and the cyclotron frequencies—and the magnetic field seen by the muons, which is expressed as the Larmor frequency of a free proton, ω_p. The ratio R of the two leads to the muon anomaly through the relation $a_\mu = R/(\lambda - R)$, where $\lambda = \mu_\mu/\mu_p$ is the muon-to-proton magnetic moment ratio, determined from muonium hyperfine level splitting [13].

The new experiment will operate in parallel with the high-energy neutrino operation, using a 30% share of protons from the upgraded 8-GeV, 15-Hz Booster. Four short "bunches" of 10^{12} protons each will be formed in the Recycler for each injected Booster batch. They will be directed to the existing antiproton target, which is presently employed in Tevatron $\bar{p}p$ collider operation. Modifications to the collecting lens system are anticipated to accommodate the higher repetition rate (and lower proton energy). A radiation-hard dc quadrupole lens and bending magnet, as used at Brookhaven, offer a simple and conventional approach, which we will likely follow. A 3.1 GeV/c positive pion beam will be directed out of the target and along the 290-m AP2 beamline. Most of the pions will decay along the way and the forward-going (0-degree) highly polarized, muons will be captured in the line, inside the FODO lattice. With the tripling of the quadrupole magnet density, a reduced beta function results, which triples the muon collection compared to the present AP2 configuration. The necessary quads exist at Fermilab and are available. The decay muons are directed around the antiproton accumulator complex (through the Debuncher ring), and then back toward the target region along the parallel transfer line AP3. Additional quads, also available, are required for optimal transport through AP3 and into a new beamline stub that raises the beam to grade level at the entrance into the storage ring. The total distance from target to storage ring is approximately 900 m, which allows for efficient muon collection in the forward direction and a sufficient suppression of undecayed pions that enter the storage ring and initiate hadronic showers. The layout is shown in Fig. 3. The plan described will increase the stored muon rate per proton on target by at least a factor of 6 compared to BNL, and it will reduce the pion-dominated background by more than a factor of 20. Both of these improvements are based on the long beamline path in the Fermilab scenario.

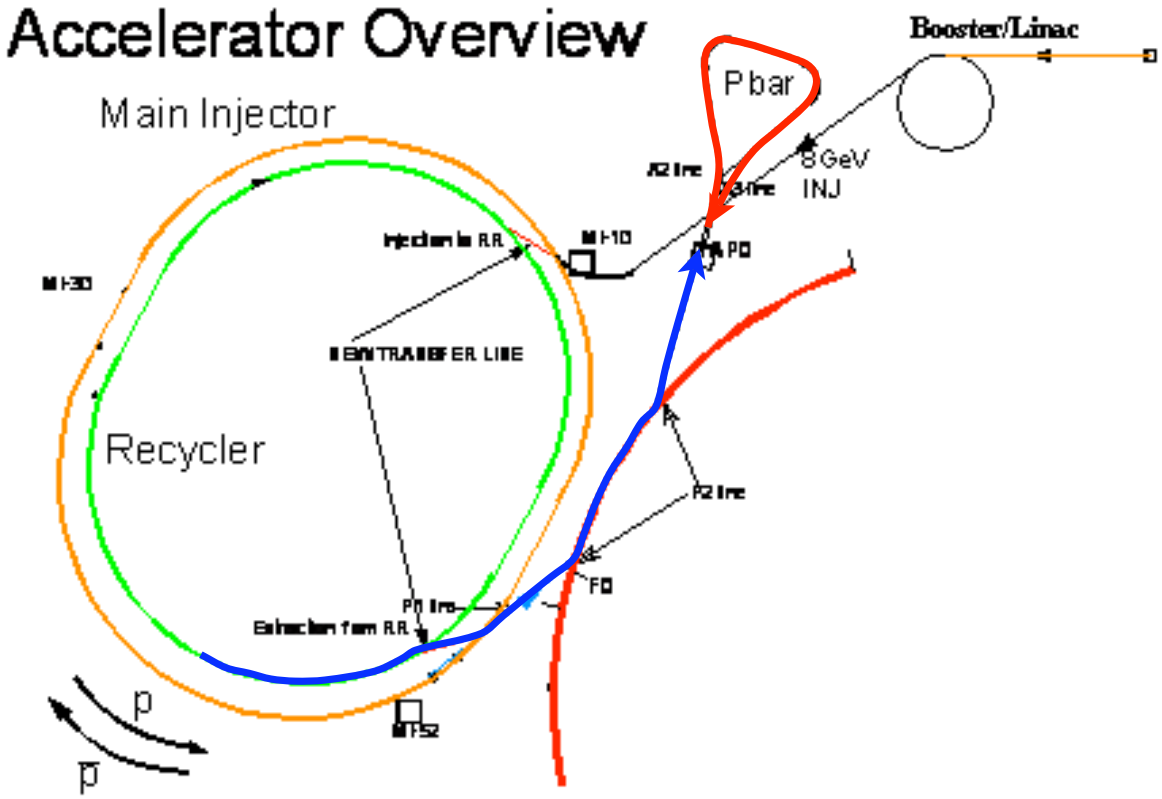

FIG. 3: Schematic of the Fermilab layout for $g-2$. A proton batch is delivered from the Booster into the Recycler (green) where it is divided into four smaller bunches by a new rf system. Each bunch is kicked out one-at-a-time and directed along the blue path to the "antiproton" target at AP0. The pions produced there travel out along the red path toward the Pbar complex and back again to the new $(g-2)$ hall, which will be located adjacent to the AP0 building.

The relocated BNL storage ring will be placed in a new, custom building near the target region. While the building has been optimized for the $g-2$ experiment—e.g., temperature and floor stability requirements, crane capacity—it is general purpose in nature and designed to host follow-up experiments that could employ proton or muon beams. The muons will enter the ring through a new superconducting inflector magnet, which will replace the existing one, which is wound in such a manner that the coils intercept the beam on both ends of the magnet. The new inflector windings avoid this, which will reduce multiple scattering and result in a higher muon storage efficiency. Once entering the ring, a better optimized pulse-forming network will energize the storage ring kicker to place the beam on a stable orbit.

The new experiment will require upgrades of detectors, electronics and data acquisition equipment to handle the much higher data volumes and slightly higher instantaneous rates. We have developed high-density, segmented tungsten/scintilating-fiber calorimeters [14] and in-vacuum straw drift tubes. The latter will be used to determine the stored muon distribution from decay positron tracks and to provide data for a greatly improved muon electric dipole moment (EDM) measurement, which can be obtained in parallel (see, for example the new EDM limit set in the BNL experiment [15].) A modern data acquisition system will be used to read out waveform digitizer data and store it so that both the traditional event mode and a new integrating mode of data analysis can both be used in parallel. The precession systematic improvement is threefold and largely based on the reduced pion contamination, the segmented detectors, and an improved storage ring kick of the muons onto orbit.

The storage ring magnetic field will be shimmed to an even more impressive uniformity, and improvements in the field-measuring system will be implemented. The field systematic is halved by better shimming, relocations of critical NMR probes, and other incremental changes.

A challenging task is the disassembly, transport, and reassembly of the BNL storage ring (See Fig. 4). It weighs 650 tons, and features three 14 m diameter superconducting coils, which must be carefully moved without distortion. We have examined the tasks in consultation with the lead project engineers and can estimate the time and cost required with a fair degree of confidence. The ring will be placed in a new and relatively modest building at the end of the AP2 line (near the AP0 blockhouse).

E. Collaboration, Timeline and Budget

The Collaboration is built from a core group of E821 participants, together with many new domestic and international groups. Indeed, many of those that built and instrumented the magnet, those that shimmed and mapped the field, those that built the detectors and electronics, and those that analyzed the data are participating. In addition, new strong groups have joined bringing additional expertise in other precision physics experiments and in large-scale construction projects, as well as expertise in running at Fermilab. We envision, as in E821, that a large number of young physicists—students and postdocs—will participate in the experiment and the data analysis phases.

FIG. 4: The existing muon storage ring that will be relocated to Fermilab for the New $g-2$ Experiment.

The critical timescale to be ready for data taking is driven by the effort to relocate the ring to Fermilab and to re-shim it to very high field uniformity. In addition, the accelerator and beam tasks must be coordinated with the timing of the Tevatron shutdown. Detector and software development will take place concurrently during this period. Our original planning envisioned approximately 1 year of design and development activities following the presentation of the proposal to the Fermilab PAC in March 2009. During this past year, in anticipation of formal approval, we have made significant progress on the design and cost estimate, the detailed building plans, the storage ring relocation task, the beamline optics design, and the detector development R&D effort. A Simulation Team has been organized, which incorporates both beamline optics programs and full Geant4 Monte Carlo of the storage ring elements and of the detector systems. A joint University-Laboratory "Beam Team" has been engaged in developing an end-to-end simulation from protons on target to stored muons in the ring. These tasks have mainly involved personnel, and have not represented significant capital costs. However, we now enter a phase where engineering and technical support to dismantle the ring are required; funds must be provide to complete the building plans and to initiate construction, and the collaboration management structure must be put into place. With a technically driven schedule, the experiment can be ready for

beam at the end of 2014. The details are provided in the body of this proposal along with the list of constraints to meet this schedule.

The costs for the New $g-2$ Experiment have been heavily scrutinized over the last year and are comparatively well-understood with respect to a typical pre-CD0 experiment. A final Total Project Cost (TPC) of \$41.3M was established, with \$35.55M being anticipated DOE support. However, \$5M of the DOE funds are for items needed by the Mu2e project, so the incremental cost to the HEP program is \$30.55M. The collaboration and the independent review committee agree to better than 10% on the TPC, well within the stated contingencies.

The costs can broadly be defined in three categories: general upgrades to the accelerator complex, civil construction of a new building with a short tunnel connection to the existing P1 tunnel, and experimental costs specific to $g-2$. The cost breakdown summary is given in the Table II, while the detailed discussion is provided in the body of this Proposal. The costs have also been subdivided by funding source, with DOE HEP costs separated from others. Average contingencies for each category are shown. The relatively small 25% contingency of the building and tunnel connections are a reflection of the detailed work performed by FESS engineers in developing an initial Project Definition Report.

Category	Cost	Contingency	Non-DOE	DOE
Building & Tunnel Connection	5240	25%		6550
Accelerator Upgrades	6876	36%		9317
$g-2$ Experiment	17208	48%	5786	19669
Totals	29324	41%	5786	35536

TABLE II: Cost summary in k\$ for the New $g-2$ Experiment. The TPC is \$41.3M. Roughly \$5M are shared costs that are required to mount the Mu2e experiment. Details are provided in the body of this Proposal.

II. INTRODUCTION

The muon magnetic moment is related to its intrinsic spin by the Landé g-factor g_μ:

$$\vec{\mu}_\mu = g_\mu \left(\frac{q}{2m}\right)\vec{S}, \tag{4}$$

where $g_\mu \equiv 2$ in the Dirac theory for a structureless, spin-$\frac{1}{2}$ particle of mass m and charge $q = \pm|e|$. Radiative corrections, the simplest of which is shown in Fig. 5, modify g, which becomes $g_\mu = 2(1 + a_\mu)$, where the "anomaly"

$$a_\mu = \frac{1}{2}(g_\mu - 2), \tag{5}$$

represents the contribution from all radiative corrections. The dominant contribution to a is the lowest-order (LO) quantum electrodynamic (QED) one of Fig. 5, which represents the very first quantum loop calculation [16], now called the "Schwinger term:" $a_\mu^{\mathrm{QED;LO}} = \alpha/2\pi \approx 1.16 \times 10^{-3}$.

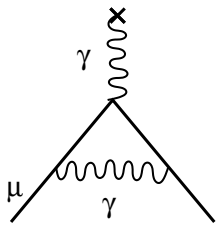

FIG. 5: The Schwinger (lowest-order QED) contribution to the muon anomaly.

The complete standard-model value of a_μ, currently evaluated to a precision of approximately 0.5 ppm (parts per million), includes this first-order term along with higher-order QED processes, electroweak loops, hadronic vacuum polarization, and other higher-order hadronic loops. The measurement of a_μ in Brookhaven E821 was carried out to a similar precision [11]. The difference between experimental and theoretical values for a_μ is a valuable test of the completeness of the standard model. At sub-ppm precision, such a test explores TeV-scale physics. The present difference between experiment and theory is

$$\Delta a_\mu(\mathrm{Expt} - \mathrm{SM}) = (255 \pm 80)) \times 10^{-11}, (3.2\,\sigma), \tag{6}$$

which is based on the 2009 summary of the standard model (SM) by Höcker and Marciano [2]. A contribution to the muon anomaly of this magnitude is expected in many popular standard

TABLE III: Summary of a_μ results from CERN and BNL, showing the evolution of experimental precision over time. The average is obtained from the BNL 1999, 2000 and 2001 data sets only.

Experiment	Years	Polarity	$a_\mu \times 10^{10}$	Precision [ppm]	Reference
CERN I	1961	μ^+	11 620 000(50 000)	4300	[18]
CERN II	1962-1968	μ^+	11 661 600(3100)	270	[19]
CERN III	1974-1976	μ^+	11 659 100(110)	10	[21]
CERN III	1975-1976	μ^-	11 659 360(120)	10	[21]
BNL	1997	μ^+	11 659 251(150)	13	[22]
BNL	1998	μ^+	11 659 191(59)	5	[23]
BNL	1999	μ^+	11 659 202(15)	1.3	[24]
BNL	2000	μ^+	11 659 204(9)	0.73	[25]
BNL	2001	μ^-	11 659 214(9)	0.72	[26]
Average			11 659 208.0(6.3)	0.54	[11]

model extensions, while other models predict smaller or negligible effects. In the LHC era, accurate and precise low-energy observables, such as a_μ, will help distinguish between candidate theories in defining a new standard model. The motivation for a new, more precise $g-2$ experiment, is to contribute significantly to the determination of the expected new physics at the electroweak scale. We devote a chapter of this proposal to the present and expected future status of the standard model evaluation and to the physics reach of an improved measurement.

Precision measurements of a_μ have a rich history dating nearly 50 years. In Table III we give a brief summary. With improved experimental methods, the precision on the measurement of a_μ has increased considerably. Advances in theoretical techniques—often driven by the promise of a new more precise measurement—have largely stayed at pace and we expect that the approval of a new Fermilab based experiment will continue to drive improvements in the determination of the SM value in the future.

We propose to measure the muon $g-2$ to a relative precision of ± 0.14 ppm, which will require more than 20 times the current event statistics. While we will largely follow the proven method pioneered at CERN and significantly improved at Brookhaven, the new

experiment requires the unique high-intensity proton accelerator complex at Fermilab to obtain a 21-times larger statistical sample. Upgrades in detectors, electronics, and field-measuring equipment will be required as part of a comprehensive plan to reduce systematic errors. These tasks are relatively well known to us as the collaboration is quite experienced in the proposed measurement. Subsequent chapters will outline the main issues and the beam use plan that is aimed to complete the experiment in less than 2 years of running.

A. Principle of the Experiment

The cyclotron ω_c and spin precession ω_s frequencies for a muon moving in the horizontal plane of a magnetic storage ring are given by:

$$\vec{\omega}_c = -\frac{q\vec{B}}{m\gamma}, \qquad \vec{\omega}_s = -\frac{gq\vec{B}}{2m} - (1-\gamma)\frac{q\vec{B}}{\gamma m}. \tag{7}$$

The anomalous precession frequency ω_a is determined from the difference

$$\vec{\omega}_a = \vec{\omega}_s - \vec{\omega}_c = -\left(\frac{g-2}{2}\right)\frac{q\vec{B}}{m} = -a_\mu \frac{q\vec{B}}{m}. \tag{8}$$

Because electric quadrupoles are used to provide vertical focusing in the storage ring, their electric field is seen in the muon rest frame as a motional magnetic field that can affect the spin precession frequency. In the presence of both $\vec{E}$ and $\vec{B}$ fields, and in the case that $\vec{\beta}$ is perpendicular to both $\vec{E}$ and $\vec{B}$, the expression for the anomalous precession frequency becomes

$$\vec{\omega}_a = -\frac{q}{m}\left[a_\mu \vec{B} - \left(a_\mu - \frac{1}{\gamma^2-1}\right)\frac{\vec{\beta}\times\vec{E}}{c}\right]. \tag{9}$$

The coefficient of the $\vec{\beta}\times\vec{E}$ term vanishes at the "magic" momentum of 3.094 GeV/c, where $\gamma = 29.3$. Thus a_μ can be determined by a precision measurement of ω_a and B. At this magic momentum, the electric field is used only for muon storage and the magnetic field alone determines the precession frequency. The finite spread in beam momentum and vertical betatron oscillations introduce small (sub ppm) corrections to the precession frequency. These are the only corrections made to the measurement.

The longitudinally polarized muons, which are injected into the storage ring at the magic momentum, have a time-dilated muon lifetime of 64.4 μs. A measurement period of typically 700 μs follows each injection or "fill." The net spin precession depends on the integrated

field seen by a muon along its trajectory. The magnetic field used in Eq. 9 refers to an average over muon trajectories during the course of the experiment. The trajectories of the muons must be weighted with the magnetic field distribution. To minimize the precision with which the average particle trajectories must be known, the field should be made as uniform as possible.

Because of parity violation in the weak decay of the muon, a correlation exists between the muon spin and decay electron direction. This correlation allows the spin direction to be measured as a function of time. In the rest frame of the muon—indicated by starred quantities—the differential probability for the electron to emerge with a normalized energy $y = E^*/E_{max}$ ($E_{max} = 52.8$ MeV) at an angle θ^* with respect to the muon spin is

$$\frac{dP(y,\theta^*)}{dy\ d\Omega} = (1/2\pi)n^*(y)[1-\alpha^*(y)\cos\theta^*] \quad \text{with} \tag{10}$$

$$n^*(y) = y^2(3-2y) \quad \text{and} \tag{11}$$

$$\alpha^*(y) = \frac{q}{e}\frac{2y-1}{3-2y}\ . \tag{12}$$

Figure 6a shows the quantities $n^*(y)$ and $\alpha^*(y)$. Electrons with $y < 0.5$ are emitted preferentially along the (negative) muon spin direction and those with $y > 0.5$ are more likely emitted opposite to the spin. Because both n^* and α^* are larger for $y > 0.5$, decay electrons tend to emerge in the direction opposite to the muon spin. Like the muon spin, the angular distribution of the electrons in the muon rest frame rotates at the angular frequency ω_a. Figure 6b shows the same differential quantities in the boosted laboratory frame ($n^* \to N, \alpha^* \to A$). Here, $E_{max} \approx 3.1$ GeV and A is the laboratory asymmetry. The statistical uncertainty on the measurement of ω_a is inversely proportional to the ensemble-averaged figure-of-merit (FOM) NA^2. The differential quantity NA^2, shown in the Fig. 6b, illustrates the relative weight by electron energy to the ensemble average FOM.

Because the stored muons are highly relativistic, the decay angles observed in the laboratory frame are greatly compressed into the direction of the muon momenta. The lab energy of the relativistic electrons is given by

$$E_{lab} = \gamma(E^* + \beta p^* c\cos\theta^*) \approx \gamma E^*(1+\cos\theta^*). \tag{13}$$

Because the laboratory energy depends strongly on the decay angle θ^*, setting a laboratory threshold E_{th} selects a range of angles in the muon rest frame. Consequently, the integrated number of electrons above E_{th} is modulated at frequency ω_a with a threshold-dependent

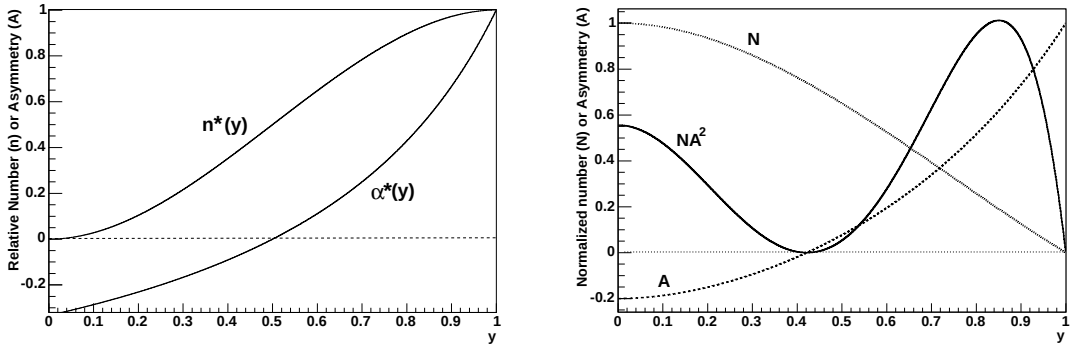

(a)Center-of-mass frame (b)Lab frame

FIG. 6: Relative number and asymmetry distributions versus electron fractional energy y in the muon rest frame (left panel) and in the laboratory frame (right panel). The differential figure-of-merit product NA^2 in the laboratory frame illustrates the importance of the higher-energy electrons in reducing the measurement statistical uncertainty.

asymmetry. The integrated decay electron distribution in the lab frame has the form

$$N_{ideal}(t) = N_0 \exp(-t/\gamma\tau_\mu)\left[1 - A\cos(\omega_a t + \phi)\right], \tag{14}$$

where N_0, A and ϕ are all implicitly dependent on E_{th}. For a threshold energy of 1.8 GeV ($y \approx 0.58$ in Fig. 6b), the asymmetry is ≈ 0.4 and the average figure-of-merit is maximized. A representative electron decay time histogram is shown in Fig. 7.

To determine a_μ, we divide ω_a by $\widetilde{\omega}_p$, where $\widetilde{\omega}_p$ is the measure of the average magnetic field seen by the muons. The magnetic field, measured using NMR, is calibrated to be expressed as the free proton (Larmor) precession frequency, ω_p.

The muon anomaly is given by:

$$a_\mu = \frac{\omega_a}{\omega_L - \omega_a} = \frac{\omega_a/\widetilde{\omega}_p}{\omega_L/\widetilde{\omega}_p - \omega_a/\widetilde{\omega}_p} = \frac{\mathcal{R}}{\lambda - \mathcal{R}}, \tag{15}$$

where ω_L is the Larmor precession frequency of the muon. The ratio $\mathcal{R} = \omega_a/\widetilde{\omega}_p$ is measured in our experiment and the muon-to-proton magnetic moment ratio

$$\lambda = \frac{\mu_\mu}{\mu_p} = 3.183\,345\,137(85) \tag{16}$$

is determined from muonium hyperfine structure measurements and theory [12, 13].

Since the publication of the final summary article by E821 [11], the value of λ has changed slightly [12]. The effect of this change has been to increase the extracted value of a_μ by

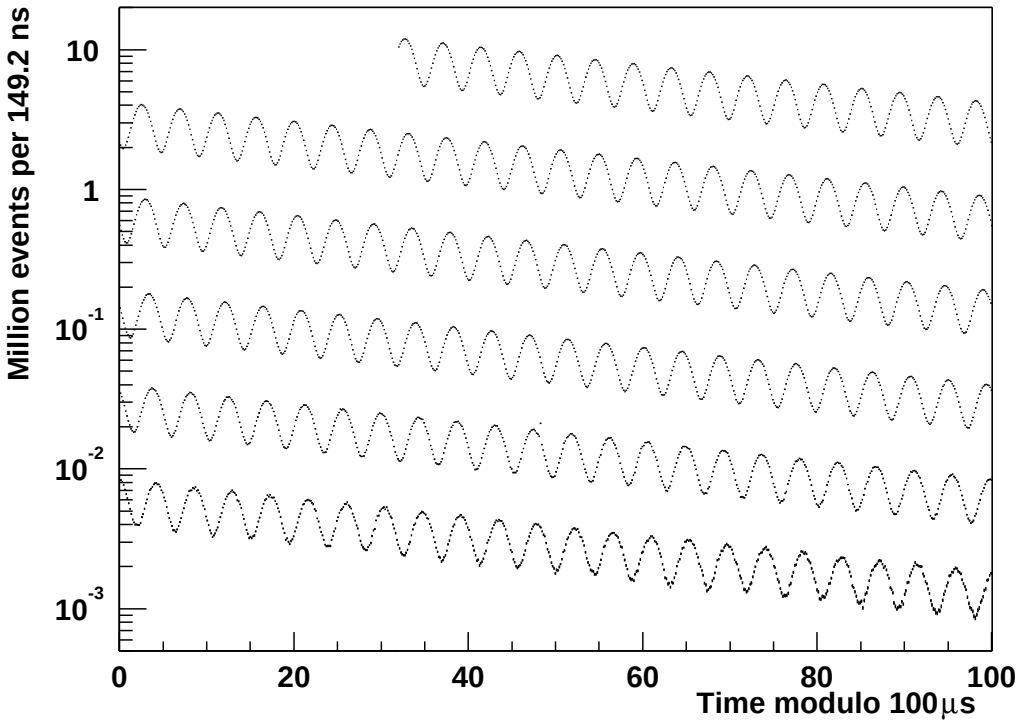

FIG. 7: Distribution of electron counts versus time for the 3.6 billion muon decays. The data are wrapped around modulo 100 μs.

9×10^{-11}, so

$$a_\mu^{(\mathrm{E821})} = 116\,592\,089(63) \times 10^{-11}\ (0.54\ \mathrm{ppm}). \tag{17}$$

The present result and standard-model theory are summarized in Table IV.

B. Experimental Specifics

Equation 15 demonstrates that both ω_a and $\widetilde{\omega}_p$ must be known to high precision to determine a_μ from the experiment. The magnetic field is measured using NMR techniques. In E821, it was shimmed to an azimuthally averaged uniformity of better than ± 1 ppm. Improvements will be made in the re-shimming process with the aim of an even more uniform field. To monitor the magnetic field during data collection, 366 fixed NMR probes are placed around the ring, in sets of two or three probes above and below the vacuum chamber. This permits monitoring of changes of both the dipole and quadrupole field locally around the ring as a function of time. A trolley with 17 NMR probes is used to map the field in the

Quantity	Value	Error	Reference
$\mathcal{R}(E821) = \frac{\omega_a}{\omega_p}$	0.003 707 206 3	20×10^{-10}	Ref. [11]
$\lambda = \frac{\mu_\mu}{\mu_p}$	3.183 345 137	85×10^{-9}	Ref. [12]
$a_\mu^{(\mathrm{E821})}$	$116\,592\,089 \times 10^{-11}$	63×10^{-11}	Ref. [11] updated by [12]
$a_\mu^{\mathrm{SM\,(e^+e^-)}}$	$116\,591\,834 \times 10^{-11}$	49×10^{-11}	Refs. [2, 4]
$a_\mu^{\mathrm{Exp}} - a_\mu^{\mathrm{Theory}}$	255×10^{-11}	80×10^{-11} $(3.2\,\sigma)$	Ref. [2, 4]

TABLE IV: Important parameters from Brookhaven Experiment 821. $\mathcal{R}$ is defined as the ratio of the anomalous precession frequency ω_a to the event-weighted magnetic field, which is expressed as the Larmor frequency of a free proton, ω_p. The anomalous moment is given by Eq. 15. The published combined $\mathcal{R}$ value in Table XV of Ref. [11] includes the systematic errors of the relative entries from the individual running periods.

storage ring, in vacuum, several times per week. The trolley probes are calibrated with a special spherical water probe, which provides a calibration to the free proton Larmor spin precession frequency ω_p. The details are described later.

The experiment will be run with positive muons owing to the higher cross section for π^+ production from 8-GeV protons. In the ring, the decay positrons are detected in new, segmented tungsten-scintillating-fiber calorimeters [14] where their energy and arrival time are measured. The number of high-energy positrons above an energy threshold E_{th} as a function of time is given by

$$N(t) = N_0(E_{th})e^{-t/\gamma\tau}\left[1 + A(E_{th})\sin(\omega_a t + \phi_a(E_{th}))\right]. \tag{18}$$

The uncertainty on ω_a is given by

$$\frac{\delta\omega_a}{\omega_a} = \frac{\sqrt{2}}{\omega_a \tau_\mu \sqrt{N} A} \tag{19}$$

where the energy threshold E_{th} is chosen to optimize the quantity NA^2.

The key to any precision measurement is the systematic errors. A summary of the realized systematic errors from BNL E821 is given in Table V. Our goal is to improve the net systematic error on both frequencies—ω_a and ω_p—to $\approx \pm 0.07$ ppm, each. The design of the new experiment is based on a full consideration of items in this table, which will be discussed in detail in the proposal. In some cases, R&D work will be required to develop instrumentation to achieve the stated systematic goals.

σ_{syst} ω_p	1999 (ppm)	2000 (ppm)	2001 (ppm)	σ_{syst} ω_a	1999 (ppm)	2000 (ppm)	2001 (ppm)
Inflector fringe field	0.20	-	-	Pile-Up	0.13	0.13	0.08
Calib. of trolley probes	0.20	0.15	0.09	AGS background	0.10	0.01	‡
Tracking B with time	0.15	0.10	0.07	Lost muons	0.10	0.10	0.09
Measurement of B_0	0.10	0.10	0.05	Timing shifts	0.10	0.02	‡
μ-distribution	0.12	0.03	0.03	E-field/pitch	0.08	0.03	‡
Absolute calibration	0.05	0.05	0.05	Fitting/binning	0.07	0.06	‡
Others†	0.15	0.10	0.07	CBO	0.05	0.21	0.07
				Beam debunching	0.04	0.04	‡
				Gain changes	0.02	0.13	0.12
Total for ω_p	0.4	0.24	0.17	Total for ω_a	0.3	0.31	0.21

TABLE V: Systematic Errors from the E821 running periods in 1999, 2000 and 2001 [24–26]. CBO stands for coherent betatron oscillations. The pitch correction comes from the vertical betatron oscillations, since $\vec{\beta} \cdot \vec{B} \neq 0$. The E-field correction is for the radial electric field seen by muons with $p_\mu \neq p_{magic}$.

†Higher multipoles, the trolley frequency, temperature, and voltage response, eddy currents from the kickers, and time-varying stray fields

‡In 2001 AGS background, timing shifts, E field and vertical oscillations, beam debunching/randomization, binning and fitting procedure together equaled 0.11 ppm

III. THE PHYSICS CASE FOR A NEW $(g-2)$ EXPERIMENT

In the first part of this section we present the standard model (SM) theory of the muon anomalous magnetic moment (anomaly). Then we discuss physics beyond the standard model (BSM) that could contribute to the anomaly at a measurable level. The conclusion is that muon $(g-2)$ will play a powerful role in the interpretation of new phenomena that might be discovered at the LHC. If new phenomena are not discovered there, then muon $(g-2)$ becomes even more important, since it would provide one of the few remaining ways to search for new physics at the TeV scale.

The magnetic moment of the muon (or electron), which is aligned with its spin, is given by

$$\vec{\mu} = g\frac{q}{2m_{\mu,e}}\vec{s}, \qquad \underbrace{g=2}_{\text{Dirac}}(1+a_\mu)\,; \tag{20}$$

where the quantity g is exactly 2 in the Dirac theory, $q = \pm e$ with e a positive number. The small number a, the anomaly, arises from quantum fluctuations, with the largest contribution coming from the single loop diagram in Fig. 8(a). This contribution was first calculated by Schwinger [16], who obtained $a = (\alpha/2\pi) = 0.00116\cdots$. These calculations have been extended to higher powers in α/π, with the fourth- $(\alpha/\pi)^2$ and sixth-order $(\alpha/\pi)^3$ contributions having been carried out analytically.

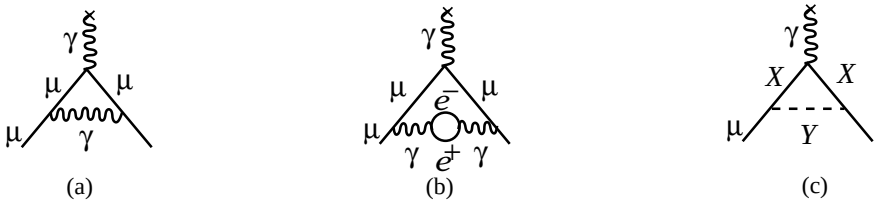

FIG. 8: The Feynman graphs for: (a) The lowest-order (Schwinger) contribution to the lepton anomaly ; (b) The vacuum polarization contribution, which is one of five fourth-order, $(\alpha/\pi)^2$, terms; (c) The schematic contribution of new particles X and Y that couple to the muon.

The electron anomaly is relatively insensitive to heavier physics, so in principle the 0.03 ppb measurement of the electron anomaly [30] should provide a test of QED, but the few ppb precision of the *independent* measurements of α prevents this comparison. Alternately, one can accept that QED is valid and use the electron anomaly to determine the

most precise measurement of α [30], which is now used by many authors when calculating the SM value of a_μ [2].

The muon anomaly is an entirely different case. The relative contribution to the muon anomaly of heavier virtual particles goes as $(m_\mu/m_e)^2 \simeq 43,000$, so with much less precision when compared with the electron, the muon anomaly is sensitive to mass scales in the several hundred GeV region. This not only includes the expected contribution of the W and Z bosons, but perhaps contributions from new, as yet undiscovered, particles such as the supersymmetric partners of the electro-weak gauge bosons (see Fig. 8(c)). The contribution from SM particles is discussed first, and then the implications for BSM physics are discussed.

The standard-model value of a_μ has three contributions from radiative processes: QED loops containing leptons (e, μ, τ) and photons; loops containing hadrons in vacuum polarization loops where the e^+e^- pair in Fig 8(b) is replaced by hadrons; and weak loops involving the weak gauge bosons W, Z, and Higgs such as is shown in Fig. 8(c) where $X = W$ and $Y = \nu$, or $X = \mu$ and $Y = Z$. Thus

$$a_\mu^{\rm SM} = a_\mu^{\rm QED} + a_\mu^{\rm hadronic} + a_\mu^{\rm weak}. \tag{21}$$

The QED and weak contributions to the muon anomaly are now well understood at the level needed for the comparison of Standard-Model theory with experiment.

The hadronic contribution must be determined from a dispersion relation using experimental data, namely the cross sections for electron-positron annihilation to hadrons. The determination of this contribution represents a worldwide effort which was driven primarily by the existence of BNL experiment E821. The possibility of a new Fermilab experiment has already stimulated further work that will certainly continue unabated if P989 turns into an approved and funded experiment.

A. The Standard-Model Value of a_μ

1. QED and weak contributions

The QED and electroweak contributions to a_μ are well understood. We take the numerical values from the recent Particle Data Group update by Höcker and Marciano [2]. The QED contribution to a_μ has been calculated through eight order (four loops), with the leading

tenth-order (five-loop) contributions estimated [28, 29, 31]. The present value is

$$a_\mu^{\rm QED} = 116\ 584\ 718.09\ (0.02)(0.14)(0.04) \times 10^{-11} \tag{22}$$

where the uncertainties are from the 4- and 5-loop QED contributions, and from the value of α taken from the electron $(g-2)$ value [2].

The electroweak contribution (shown in Fig. 9) is now calculated through two loops [32–36]. The single loop result

$$\begin{aligned} a_\mu^{\rm EW(1)} &= \frac{G_F}{\sqrt{2}}\frac{m_\mu^2}{8\pi^2}\left\{ \underbrace{\frac{10}{3}}_{W} + \underbrace{\frac{1}{3}(1-4\sin^2\theta_W)^2 - \frac{5}{3}}_{Z} \right. \\ &\quad \left. + \mathcal{O}\left(\frac{m_\mu^2}{M_Z^2}\log\frac{M_Z^2}{m_\mu^2}\right) + \frac{m_\mu^2}{M_H^2}\int_0^1 dx \frac{2x^2(2-x)}{1-x+\frac{m_\mu^2}{M_H^2}x^2} \right\} \\ &= 194.8 \times 10^{-11}\,, \end{aligned} \tag{23}$$

was calculated by five separate groups shortly after the Glashow-Salam-Weinberg theory was shown by 't Hooft to be renormalizable. With the present limit on the Higgs boson mass, only the W and Z contribute to the lowest-order electroweak at a measurable level.

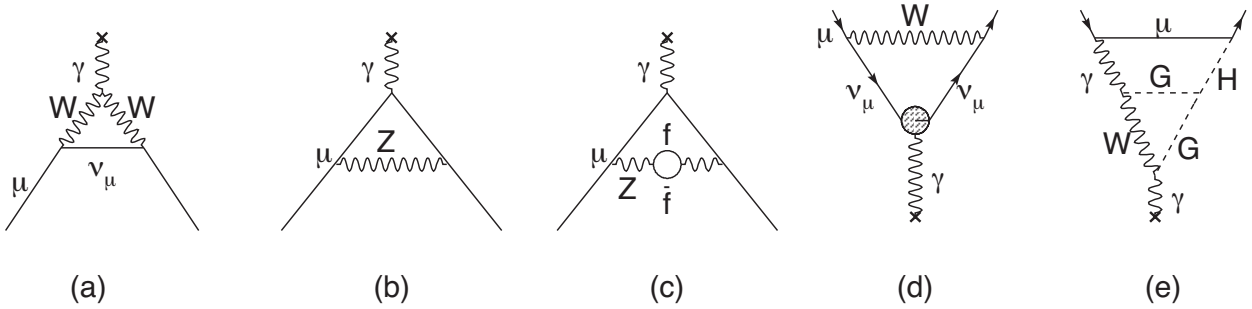

FIG. 9: Weak contributions to the muon anomalous magnetic moment. Single-loop contributions from (a) virtual W and (b) virtual Z gauge bosons. These two contributions enter with opposite sign, and there is a partial cancellation. The two-loop contributions fall into three categories: (c) fermionic loops which involve the coupling of the gauge bosons to quarks, (d) bosonic loops which appear as corrections to the one-loop diagrams, and (e) a new class of diagrams involving the Higgs where G is the longitudinal component of the gauge bosons. See Ref. [1] for details. The $\times$ indicates the virtual photon from the magnetic field.

The two-loop weak contribution, (see Figs. 9(c-e) for examples) is negative, and the total electroweak contribution is

$$a_\mu^{\rm EW} = 154(1)(2) \times 10^{-11} \tag{24}$$

where the first error comes from hadronic effects in the second-order electroweak diagrams with quark triangle loops, and the latter comes from the uncertainty on the Higgs mass [1, 17, 32–34]. The leading logs for the next-order term have been shown to be small [36]. The weak contribution is about 1.3 ppm of the anomaly, so the experimental uncertainty on a_μ of ± 0.54 ppm now probes the weak scale of the standard model.

2. Hadronic contribution

The hadronic contribution to a_μ is about 60 ppm of the total value. The lowest-order diagram shown in Fig. 10(a) dominates this contribution and its error, but the hadronic light-by-light contribution Fig. 10(e) is also important. We discuss both of these contributions below.

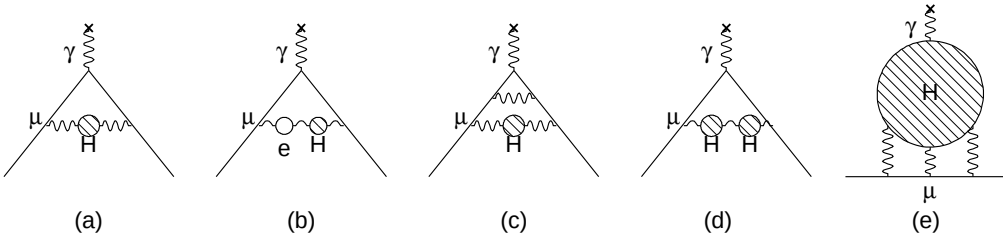

FIG. 10: The hadronic contribution to the muon anomaly, where the dominant contribution comes from the lowest-order diagram (a). The hadronic light-by-light contribution is shown in (e).

The energy scale for the virtual hadrons is of order $m_\mu c^2$, well below the perturbative region of QCD. Thus it must be calculated from the dispersion relation shown pictorially in Fig. 11,

$$a_\mu^{\rm had;LO} = \left(\frac{\alpha m_\mu}{3\pi}\right)^2 \int_{4m_\pi^2}^{\infty} \frac{ds}{s^2} K(s) R(s), \quad \text{where} \quad R \equiv \frac{\sigma_{\rm tot}(e^+e^- \to \text{hadrons})}{\sigma(e^+e^- \to \mu^+\mu^-)}\,, \tag{25}$$

using the measured cross sections for $e^+e^- \to$ hadrons as input, where $K(s)$ is a kinematic factor ranging from -0.63 at $s = 4m_\pi^2$ to 1 at $s = \infty$. This dispersion relation relates the bare cross section for e^+e^- annihilation into hadrons to the hadronic vacuum polarization

contribution to a_μ. Because the integrand contains a factor of s^{-2}, the values of $R(s)$ at low energies (the ρ resonance) dominate the determination of $a_\mu^{\rm had;LO}$, however at the level of precision needed, the data up to 2 GeV are quite important. This is shown in Fig. 12, where the left-hand chart gives the relative contribution to the integral for the different energy regions, and the right-hand gives the contribution to the error squared on the integral. The contribution is dominated by the two-pion final state, but other low-energy multi-hadron cross sections are also important.

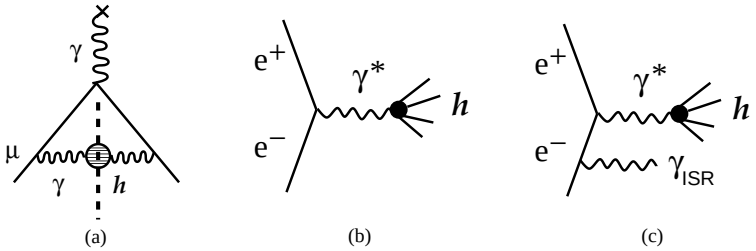

FIG. 11: (a) The "cut" hadronic vacuum polarization diagram; (b) The e^+e^- annihilation into hadrons; (c) Initial state radiation accompanied by the production of hadrons.

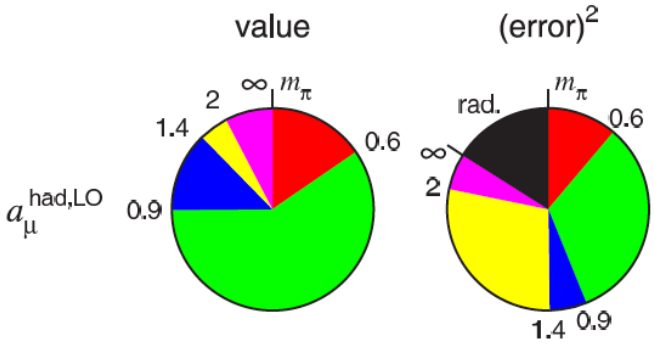

FIG. 12: Contributions to the dispersion integral, and to the error on the dispersion integral. Taken from T. Teubner [40]. The error graph does not reflect the new KLOE or BaBar data.

These data for e^+e^- annihilation to hadrons are also important as input into the determination of $\alpha_s(M_Z)$ and other electroweak precision measurements, including the limit on the Higgs mass [46, 48]. After the discussion of the determination of the hadronic contribution, we will return to the implications on M_H.

In the 1980s when E821 was being proposed at Brookhaven, the hadronic contribution was know to about 10 ppm. It now is known to about 0.4 ppm. This improvement has come from

the hard work of many experimental and theoretical physicists. The low energy e^+e^- data of the 80s have been replaced by very precise data from the CMD2 and SND collaborations in Novosibirsk, the KLOE collaboration at Frascati, and the BaBar collaboration at SLAC. Additional data are expected from the Belle detector at KEK. In addition to the collider experiments, significant theoretical work has been carried out in generating the radiator functions used in the initial-state radiation (ISR) experiments at Frascati and BaBar [49, 50], as well as on the hadronic light-by-light contribution shown in Fig. 10(e).

The worldwide effort to improve our knowledge of the hadronic contribution continues to this day. In the summer and fall of 2009 new results were reported by the BaBar [8] and KLOE [66, 67] collaborations. Muon $(g-2)$ is featured prominently in the recent international workshops Tau [37, 38] and PHIPSI [39], where sessions were devoted to all issues around muon $(g-2)$. We emphasize that while this is a difficult subject, progress will continue to be made, provided that a new experiment does indeed go forward at Fermilab.

3. Lowest- and next-lowest-order hadronic contribution

The cross sections at low energies dominate the dispersion relation, and until recently the low-energy electron-positron storage rings in Novosibirsk and Frascati provided the bulk of the new measurements. The Novosibirsk experiments CMD2 (cryogenic magnetic detector) and SND (spherical neutral detector) collected data using the traditional e^+e^- energy scan. The KLOE experiment ran at a fixed energy around 1 GeV, either on the ϕ-resonance or just below it, using initial-state radiation to lower the collision energy and provide the full energy range in a single measurement (see Fig. 11(c)). The BaBar experiment also used the ISR technique, but operated at a much higher energy at or near the $\Upsilon 4s$, which permitted observation of the ISR photon. The Belle experiment is also beginning to look at ISR data. The ISR (sometimes called "radiative return") technique is possible because of the development of the necessary theory [49, 50], which provides the effective virtual photon spectrum, called the "radiator function."

While the KLOE experiment was limited to the $\pi\pi\gamma$ channel, the higher energy of the PEP-2 collider permitted BaBar to detect the ISR photon and to measure many multiple hadron final states along with the $\pi\pi\gamma$ final state, thus providing important data from channels which were either very imprecise, or simply not available before. The first $\pi^+\pi^-$

data from BaBar were released in August 2009 [8], and covered the energy range from threshold to 3 GeV. Unlike the other experiments that used a calculated $\mu\mu$ cross section for the denominator in Eq. (25), the BaBar experiment measured the $\mu\mu$ production directly and took the ratio of experimental numbers to determine $R(s)$ directly. This had the benefit of canceling a number of systematic errors, and significantly lowered the uncertainty on the cross section. If BaBar had used the calculated $\mu\mu$ cross section, the cross section errors would have been at the $\sim 5\%$ level, much too large to be useful in the determination of $a_\mu^{\rm had}$.

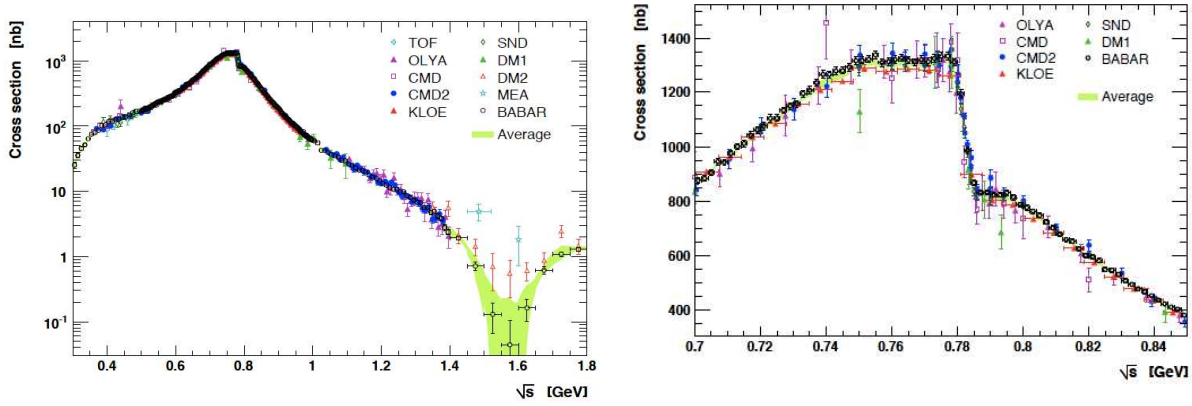

(a) (b)

FIG. 13: The $\pi\pi$ cross section from BaBar, CMD2, KLOE and SND. The right-hand side shows a blowup of the ρ resonance region. The sharp cusp comes from $\rho - \omega$ interference.

As mentioned above, the two-pion final state is the most important contributor to the dispersion integral. Published cross sections from the BaBar, KLOE, CMD2 and SND experiments are shown in Fig. 13. New KLOE large-angle data were reported at PHIPSI2009[67], and are displayed in Fig. 14 as the pion form factor F_π, which is related to the cross section by

$$\sigma_{e^+e^-\to\pi^+\pi^-} = \frac{\pi\alpha^2}{3s}\beta_\pi^3|F_\pi|^2. \tag{26}$$

These newest data, which form an independent data set that agrees well with the previous KLOE data set, are not yet included in the determination of the lowest-order hadronic contribution to a_μ. They were analyzed by a different group of collaborators who worked independently from those involved in the the KLOE08 [66] analysis. This new data set is final and a paper is in preparation, with the goal that the paper be submitted for publication

in April [44].

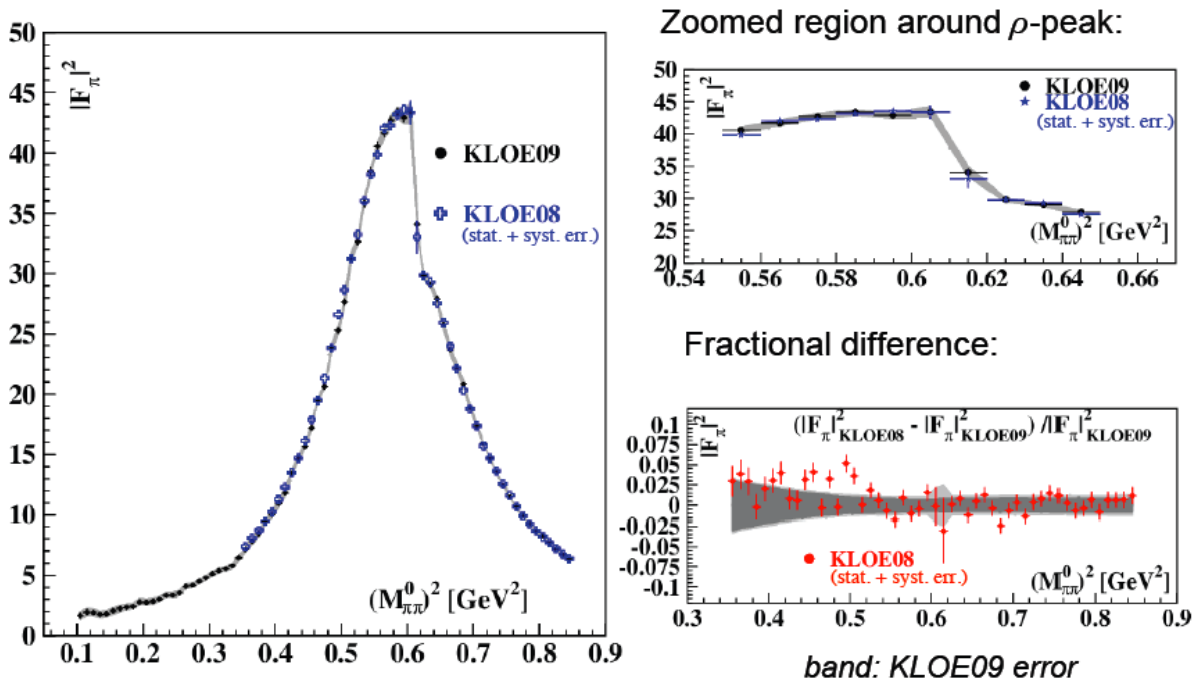

FIG. 14: The pion form factor $|F_\pi|^2$ from KLOE08 and KLOE09. The right-hand side shows a blowup of the ρ resonance region.

A recent analysis [69] that includes the 2008 KLOE data, along with the 2009 result from BaBar (but not the large-angle KLOE data reported in October [67]) gives:

$$a_\mu^{\rm had;LO} = (6\ 955 \pm 40_{\rm exp} \pm 7_{\rm QCD}) \times 10^{-11}\,. \tag{27}$$

Important earlier global analyses include those of HMNT [51], Davier, et al., [52], Jegerlehner [53].

The next-order hadronic contribution shown in Fig. 10(b-d) can also be determined from a dispersion relation, and the result is [69]

$$a_\mu^{\rm had:NLO)} = (-97.9 \pm 0.8_{\rm exp} \pm 0.3_{\rm rad}\ ) \times 10^{-11}\,. \tag{28}$$

4. $a_\mu^{\rm had;LO}$ *from hadronic* τ *decay*

The value of $a_\mu^{\rm had;LO}$ from threshold up to m_τ could in principle be obtained from hadronic τ^- decays (See Fig. 10), provided that the necessary isospin corrections are known. This

was first demonstrated by Almany, Davier and Höcker [57]. In the absence of second-class currents, hadronic τ decays to an *even* number of pions such as $\tau^- \to \pi^-\pi^0\nu_\tau$ goes through the vector part of the weak current, and can be related to e^+e^- annihilation into $\pi^+\pi^-$ through the CVC hypothesis and isospin conservation (see Fig. 15) [57–59]. The τ-data only contain an isovector piece, and the isoscalar piece present in e^+e^- annihilation has to be put in "by hand" to evaluate $a_\mu^{\rm had;LO}$. Until recently there were 3.5 to 4.5 standard deviation differences when e^+e^- data and the CVC hypothesis were used to determine the $\tau^- \to \nu_\tau\pi^-\pi^0$ or $\tau^- \to \nu_\tau 2\pi^-\pi^+\pi^0$ branching fractions, when compared with the experimental values. Thus most authors [17, 47, 51] concluded that there are unresolved issues, most likely incorrect isospin breaking corrections, that make it difficult to use the τ data on an equal footing with the e^+e^- data. More recently new isospin corrections have been obtained [70] that reduce this difference in predicted vs. measured branching fractions to 2.2 standard deviations. If the tau data are used to determine the low-s region of the HVP dispersion integral, then $a_\mu^{\rm Had;LO} = 7053(40)(19)(7) \times 10^{-11}$, and Δa_μ is reduced from the 3.2 standard deviations obtained from the e^+e^- data to 1.9 standard deviations [2]. We believe that this difference between e^+e^- and τ data will eventually be clarified.

We should note that the theoretical uncertainties on the dispersion relation in Eq. (25), which assumes analyticity and the optical theorem, are negligible. The cross section that enters in Eq. (25) is the bare cross section, and some of the early experiments were not so careful in their reporting the data and being clear on what, if any radiative corrections were applied. All of the modern experiments are well aware of these issues, and their reported errors include any uncertainties introduced in determining the bare cross section.

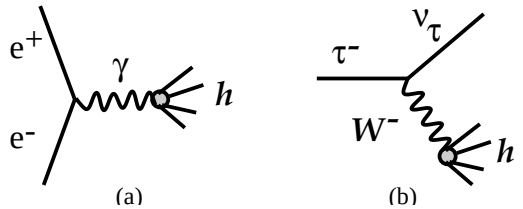

FIG. 15: e^+e^- annihilation into hadrons (a), and hadronic τ decay (b).

5. Hadronic light-by-light contribution

The hadronic light-by-light contribution, (Fig. 10(e)) cannot at present be determined from data, but rather must be calculated using hadronic models that correctly reproduce the properties of QCD. A number of authors have calculated portions of this contribution, and recently a synthesis of all contributions has become available from Prades, de Rafael and Vainshtein [10, 41], which has been agreed to by authors from each of the leading groups working in this field. They obtain

$$a_\mu^{\rm HLbL} = (105 \pm 26) \times 10^{-11}\,. \tag{29}$$

Additional work on this contribution is underway at Minnesota [60] and elsewhere. A Workshop at the Institute for Nuclear Theory in Seattle is being planned for 2011, with the aim to bring together all of the interested experts.

One important point should be made here. The main physics of the hadronic light-by-light scattering contribution is well understood. In fact, but for the sign error unraveled in 2002, the theoretical predictions for $a_\mu^{\rm HLBL}$ have been relatively stable for more than ten years. We summarize with a quote from Eduardo de Rafael [42]:

> "For the time being, concerning the issue of errors, and after the work in PdeRV, I personally think that a 25% error on the HLbL is quite a generous one. One of my reasons is the fact that in the comparable HVP contribution—assuming that we did not have data from *ee*-annihilations nor tau-decays—I claim that from the underlying physics which we know, and using the same techniques as in the HLbL calculation, we are presently able to make there an estimate which, when compared to the one with data, turns out to be quite good: at the 10% to 15% level."

In addition to the theoretical work on the HLBL, a new facility is being commissioned at DAϕNE which will provide tagged virtual photons for $\gamma^*\gamma^*$ physics. Both high- and low-energy taggers are being constructed on both sides of the interaction region to detect and measure the scattered electron and positron. Thus a coincidence between the scattered electrons and a π^0 would provide information on $\gamma^*\gamma^* \to \pi^0$, etc. [43], and will provide experimental constraints on the models used to calculate the hadronic light-by-light contribution.

B. Summary of the Standard-Model Value and Comparison with Experiment

Following Höcker and Marciano [2], the SM value obtained from the published e^+e^- data from BaBar, KLOE, CMD2 and SND, including the BaBar data for the multi-pion final states, is used to determine $a_\mu^{\rm had:LO}$ and $a_\mu^{\rm had;NLO}$. A summary of these values is given in Table VI.

TABLE VI: Standard-model contributions to the muon anomaly. Taken from Höcker and Marciano [2].

Contribution	Result in 10^{-11} units
QED (leptons)	$116\,584\,718.09 \pm 0.02 \pm 0.14 \pm 0.04_\alpha$
HVP(lo)	$6\ 955 \pm 40_{\rm exp} \pm 7_{\rm pQCD}$
HVP(HO)	$-98 \pm 0.9_{\rm exp} \pm 0.3_{\rm rad}$
HLxL	105 ± 26
EW	$154 \pm 1 \pm 2$
Total SM	$116\ 591\ 834 \pm 49$

This SM value is to be compared with the combined a_μ^+ and a_μ^- values from E821 [11] corrected for the revised value of λ as mentioned above:

$$a_\mu^{\rm E821} = (116\,592\,089 \pm 63) \times 10^{-11} \quad (0.54\,{\rm ppm}), \tag{30}$$

$$a_\mu^{\rm SM} = (116\,591\,834 \pm 49) \times 10^{-11}\,(0.44\,{\rm ppm}) \tag{31}$$

which give a difference of

$$\Delta a_\mu({\rm E821} - {\rm SM}) = (255 \pm 80) \times 10^{-11}\,. \tag{32}$$

This comparison is shown graphically in Fig. 16.

This difference of 3.2 standard deviations is tantalizing, but we emphasize that whatever the final agreement between the measured and SM value turns out to be, it will have significant implications on the interpretation of new phenomena that might be found at the LHC and elsewhere. This point is discussed in detail below.

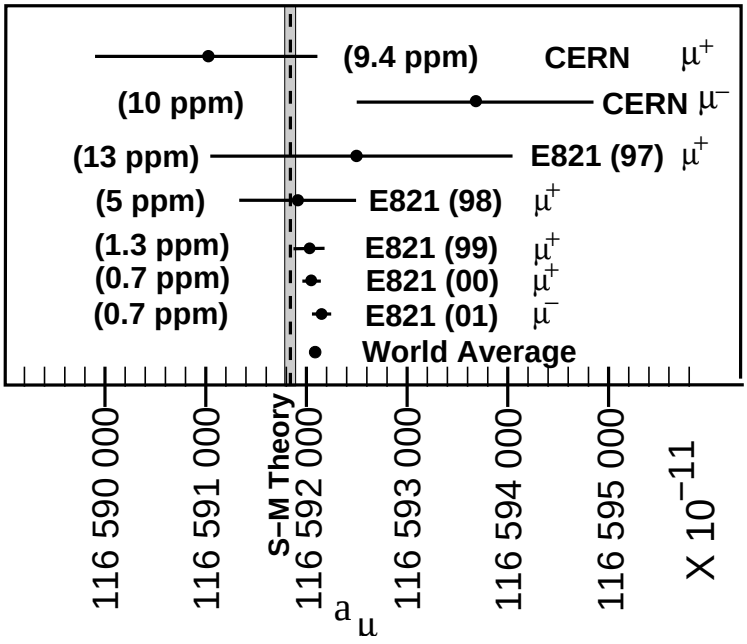

FIG. 16: Measurements of a_μ along with the SM value given above.

The present theoretical error [2, 4] of $\pm 49 \times 10^{-11}$ (0.42 ppm) is dominated by the $\pm 41 \times 10^{-11}$ uncertainty on the lowest-order hadronic contribution and the $\pm 26 \times 10^{-11}$ uncertainty on the hadronic light-by-light contribution. The lowest-order hadronic contribution could be reduced to 25×10^{-11} based on the analysis of existing data and on the data sets expected from future efforts, e.g. VEPP-2000 [45]. When combined with future theoretical progress on the hadronic light-by-light contribution, the total SM error could reach 30×10^{-11}.

With the proposed experimental error of $\pm 16 \times 10^{-11}$, the combined uncertainty for the difference between theory and experiment would be $\pm 34 \times 10^{-11}$, which is to be compared with the $\pm 81 \times 10^{-11}$ in Eq. (32).

1. *$R(s)$ measurements and the Higgs mass, M_H*

If the hadronic cross section that enters into the dispersion relation of Eq. (25) were to increase significantly from the value obtained in the published papers of CMD2, SND and KLOE, then as pointed out by Passera, Marciano and Sirlin [48], it would have significant implications for the limit on the mass of the Higgs boson. The value of $\Delta\alpha^{(5)}_{\rm had}(M_Z)$ depends

on the *same* measured cross-sections that enter into Eq. (25),

$$\Delta\alpha^{(5)}_{\rm had}(M_Z) = \frac{M_Z^2}{4\alpha\pi^2} P \int_{4m_\pi^2}^{\infty} ds \frac{\sigma(s)}{M_Z^2 - s}\,. \tag{33}$$

The present bound of $M_H \leq 150$ GeV (95% C.L.) changes if $\Delta\alpha_{\rm had}(M_Z)$ changes. Assuming that the hadronic contribution to a_μ is increased by the amount necessary to remove the difference between the experimental and theoretical values of a_μ, the effect on M_H is to move the upper bound down to $\simeq 130$ GeV. Given the experimental limit $M_H > 114.4$ GeV (95% C.L.), this significantly narrows the window for the Higgs mass. The details depend on the s-region assumed to be incorrect in the hadronic cross section. A much more complete discussion is given in Ref. [46, 48].

C. Expected Improvements in the Standard-Model Value

Much experimental and theoretical work is going on worldwide to refine the hadronic contribution. One reflection of this effort is the workshop held in Glasgow [61], which brought together 27 participants who are actively working on parts of this problem, including the BSM implications of a_μ. These participants represented many additional collaborators. As mentioned above, measurements related to $a_\mu^{\rm had}$ have featured prominently in the series of tau-lepton workshops and PHIPSI workshops which are held in alternate years.

Over the development period of our new experiment, we expect further improvements in the SM-theory evaluation. This projection is based on the following developments and facts:

- **Novosibirsk:** The VEPP2M machine has been upgraded to VEPP-2000. The maximum energy has been increased from $\sqrt{s} = 1.4$ GeV to 2.0 GeV. Additionally, the CMD2 and SND detectors have been upgraded. The cross section will be measured from threshold to 2.0 GeV using an energy scan, filling in the energy region between 1.4 GeV, where the present scan ended, up to 2.0 GeV, the lowest energy point reached by the BES collaboration in their measurements. See Fig. 12 for the present contribution to the overall error from this region. Engineering runs began in 2009, with data collection expected to begin in 2010. They will also take data at 2 GeV, using ISR, which will provide data between the PEP2 energy at the $\Upsilon(4s)$ and the 1 GeV ϕ energy at the DAϕNE facility in Frascati. The dual ISR and scan approach will provide an important cross check on the two central methods to determine HVP.

- **KLOE:**One additional data set from KLOE exists where they will report on the direct ratio of $\pi\pi/\mu\mu$. The two photon physics program will be ramping up in 2010, which will provide experimental input to the hadronic light-by-light theory.

- **BaBar:**A significant amount of new data exists from BaBar, which can be used to provide another ISR measurement from threshold to 3 GeV. Michel Davier has agreed to help advise any new group in the collaboration that would take on the analysis challenge.

- **Belle:** Some work on ISR measurements of $R(s)$ is going on in multi-hadron channels. These studies will complement those completed at BaBar and provide an important check.

- **Calculations on the Lattice for Lowest-Order HVP:** With the increased computer power available for lattice calculations, it may be possible for lattice calculations to contribute to our knowledge of the lowest-order hadronic contribution. Blum has already performed a proof-of-principle quenched calculation [62, 63]. Several groups, UKQCD (Edinburg), DESY-Zeuthen (Renner and Jansen), and the LSD (lattice strong dynamics) group in the US are all working on the lowest-order contribution.

- **Calculations on the Lattice of Hadronic Light-by-Light:** The hadronic light-by-light contribution has a magnitude of $(105 \pm 26) \times 10^{-11}$, ~ 1 ppm of a_μ. A modest calculation on the lattice would have a large impact. Blum and his collaborators at BNL and RIKEN (RBC collaboration) are working on the theoretical framework for a lattice calculation of this contribution, and are calculating the QED light-by-light contribution as a test of the program [64].

D. Physics Beyond the Standard Model

For many years, the muon anomaly has played an important role in constraining physics beyond the standard model [65, 71–73]. The over 1300 citations to the major E821 papers [11, 24–26], with 150 in 2009, demonstrates that this role continues. The citations are shown as a function of year in Fig. 17. As discussed in the previous section (see Eq. (32)), the present Standard-Model value is smaller than the experimental value by

$\Delta a_\mu(\text{E821} - \text{SM}) = (255 \pm 80) \times 10^{-11}$.

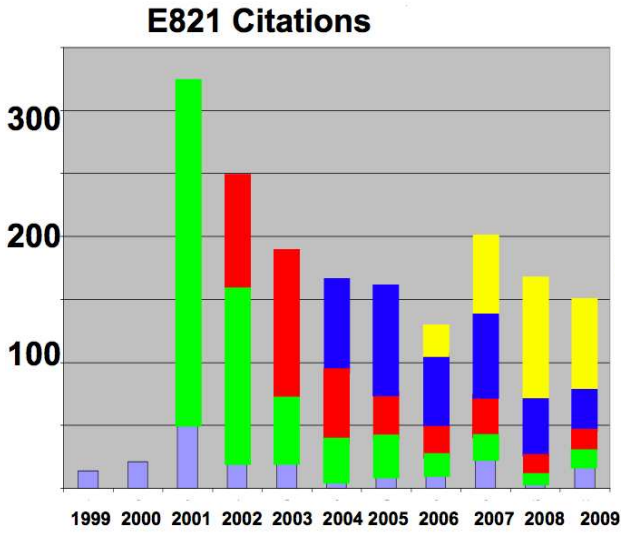

FIG. 17: Citations by year to the E821 papers reporting physics results: light blue [22] plus [23]; green [24]; red [25]; blue [26]; and yellow the Physical Review article [11].

In this section, we discuss how the muon anomaly provides a unique window to search for physics beyond the standard model. If new physics is discovered at the LHC, then a_μ will play an important role in sorting out the interpretation of those discoveries. In the sections below, examples of constraints placed on various models that have been proposed as extensions of the standard model are discussed. However, perhaps the ultimate value of an improved limit on a_μ, will come from its ability to constrain the models that we have not yet invented.

1. Overview

The LHC experiments have just begun operation, thus taking the next major energy step forward in directly probing physics at the TeV scale. This scale appears to be a crucial scale in particle physics. It is linked to electroweak symmetry breaking, and many arguments indicate that radically new concepts such as supersymmetry, extra dimensions, technicolor, or other new interactions, could be realized at this scale. Cold dark matter particles could have weak-scale/TeV-scale masses, and models of Grand Unification prefer the existence of supersymmetry at the TeV scale. TeV-scale physics could be very rich, and

the LHC is designed to discover physics beyond the standard model. Independent of whether the LHC establishes physics beyond the SM or produces the SM Higgs and nothing else, complementary experiments are needed in the quest to understand the TeV scale. This need is highlighted by the unprecedented complexity of the LHC accelerator and experiments, the involved initial and final states, and the huge backgrounds at the LHC.

The muon $(g-2)$, together with searches for charged lepton flavor violation, electric dipole moments, and rare decays, provides such a complementary tool to probe the high-energy frontier.

The complementarity between these different measurements can be easily seen. $g-2$ corresponds to a flavor- and CP-conserving interaction which is sensitive to and potentially enhanced by chirality flips. Many high-energy collider observables are insensitive to chirality flips. Many other low-energy observables are chirality-flipping but flavor-violating (b- or K-decays, $\mu \to e$ conversion, etc) or CP-violating (electric dipole moments). Furthermore, while $g-2$ is sensitive to leptonic couplings, b- or K-physics more naturally probe the hadronic couplings of new physics. If charged lepton-flavor violation exists, observables such as $\mu \to e$ conversion can only determine a combination of the strength of lepton-flavor violation and the mass scale of new physics. In that case, $g-2$ can help to disentangle the nature of the new physics.

The role of $g-2$ as a discriminator between very different standard model extensions is well illustrated by a relation discussed by Czarnecki and Marciano [71] that holds in a wide range of models as a result of the chirality-flipping nature of $g-2$: If a new physics model with a mass scale Λ contributes to the muon mass $\delta m_\mu(\text{N.P.})$, it also contributes to a_μ, and the two contributions are related as

$$a_\mu(\text{N.P.}) = \mathcal{O}(1) \times \left(\frac{m_\mu}{\Lambda}\right)^2 \times \left(\frac{\delta m_\mu(\text{N.P.})}{m_\mu}\right). \tag{34}$$

The ratio $C(\text{N.P.}) \equiv \delta m_\mu(\text{N.P.})/m_\mu$ is typically between $\mathcal{O}(\alpha/4\pi)$ (for perturbative contributions to the muon mass) and $\mathcal{O}(1)$ (if the muon mass is essentially due to radiative corrections). Hence the contributions to a_μ are highly model dependent.

It is instructive to classify new physics models as follows:

- Models with $C(\text{N.P.}) \simeq 1$: In such models the muon mass is essentially generated by radiative effects at some scale Λ. A variety of such models have been discussed in [71],

including extended technicolor or generic models with naturally vanishing bare muon mass. In these models the new physics contribution to a_μ can be very large,

$$a_\mu(\Lambda) \simeq \frac{m_\mu^2}{\Lambda^2} \simeq 1100 \times 10^{-11} \left(\frac{1\ \text{TeV}}{\Lambda}\right)^2. \tag{35}$$

and the difference Eq. (32) can be used to place a lower limit on the new physics mass scale, which is in the few TeV range [74].

- Models with $C(\text{N.P.}) = \mathcal{O}(\alpha/4\pi)$: In such models a difference as large as Eq. (32) is very hard to accommodate unless the mass scale is very small, of the order of M_Z. If any of these are realized in Nature, the new measurement of a_μ would be expected to agree with the standard model value within approximately $\pm 34 \times 10^{-11}$, the projected sensitivity of the combined standard model plus experiment sensitivity. Conversely, if the future a_μ-measurement establishes a definite deviation from the standard model prediction, such models will all be conclusively ruled out. There are many well-motivated models of this kind, e.g. models with extra weakly interacting gauge bosons Z', W', certain models with extra dimensions, and variants of Little Higgs models. As examples, the contributions to a_μ in a model with $\delta = 1$ (or 2) universal extra dimensions [75] and the Littlest Higgs model with T-parity [76] are given by

$$a_\mu(\text{UED}) \simeq -5.8 \times 10^{-11}(1 + 1.2\delta) S_{\text{KK}}, \tag{36}$$

$$a_\mu(\text{LHT}) < 12 \times 10^{-11} \tag{37}$$

with $|S_{\text{KK}}| \lesssim 1$ [75]. In both cases, the models predict observable effects at the LHC, which are hard to distinguish from e.g. supersymmetry at the LHC. Many other models with extra weakly interacting particles give similar results [77].

- Models with intermediate values for $C(\text{N.P.})$ and mass scales around the weak scale: In such models, contributions to a_μ could be as large as Eq. (32) or even larger, or smaller, depending on the details of the model. This implies that a more precise a_μ-measurement will have significant impact on such models and can even be used to measure model parameters. Supersymmetric models are the most well-known examples, so muon $g-2$ would have substantial sensitivity to the supersymmetric particles. Compared to generic perturbative models, supersymmetry provides an enhancement

to $C(\mathrm{SUSY}) = \mathcal{O}(\tan\beta\alpha/4\pi)$ and to $a_\mu(\mathrm{SUSY})$ by a factor $\tan\beta$ (the ratio of the vacuum expectation values of the two Higgs fields). The SUSY diagrams for the magnetic dipole moment, the electric dipole moment, and the lepton-number violating conversion process $\mu \to e$ in the field of a nucleus are shown pictorially in Fig. 18. In a model with SUSY masses equal to Λ the supersymmetric contribution to a_μ is given by [71]

$$a_\mu(\mathrm{SUSY}) \simeq \mathrm{sgn}(\mu)\ 130 \times 10^{-11}\ \tan\beta\ \left(\frac{100\ \mathrm{GeV}}{\Lambda}\right)^2 \tag{38}$$

which indicates the dependence on $\tan\beta$, and the SUSY mass scale, as well as the sign of the SUSY μ-parameter. The formula still approximately applies even if only the lighter smuon and chargino masses are of the order Λ but e.g. squarks and gluinos are much heavier. Thus muon $g-2$ is sensitive to SUSY models with SUSY masses in the few hundred GeV range, even if $\tan\beta$ is as low as around 10. Conversely, such SUSY models could provide an explanation of the deviation in Eq. (32).

There are many non-supersymmetric models of this kind, too. The most well-known are variants of Randall-Sundrum models [78–80] and large extra dimension models [81]. In these models, large contributions to a_μ are possible, but the theoretical evaluation is difficult because of cutoff dependences. Further examples include scenarios of unparticle physics [82, 83] (here a more precise a_μ-measurement would constrain the unparticle scale dimension and effective couplings), Hidden Sector models of Ref. [84] or a model with the discrete flavor symmetry group T' and Higgs triplets [85] (here a more precise a_μ-measurement would constrain Hidden Sector/Higgs triplet masses and couplings), or the model proposed in Ref. [86], which implements the idea that neutrino masses, leptogenesis and the deviation in a_μ all originate from dark matter particles. In the latter model, new leptons and scalar particles are predicted, and a_μ provides significant constraints on the masses and Yukawa couplings of the new particles.

The following types of new physics scenarios are quite different from the ones above:

- Models with extended Higgs sector but without enhanced Yukawa couplings: Among these models are the usual two-Higgs-doublet models or the Shadow Higgs scenario of Ref. [87]. The contribution of such models to a_μ is suppressed by two additional

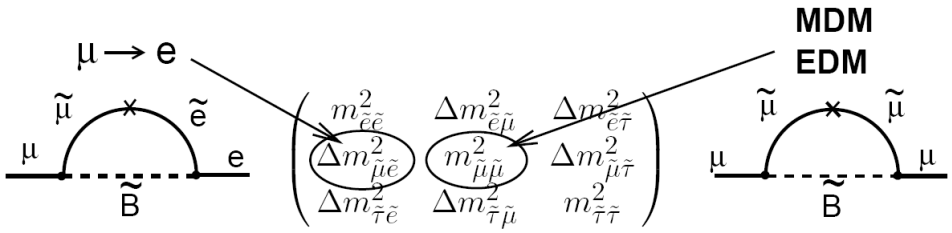

FIG. 18: The supersymmetric contributions to the anomaly, and to $\mu \to e$ conversion, showing the relevant slepton mixing matrix elements. The MDM and EDM give the real and imaginary parts of the matrix element, respectively. The $\times$ indicates a chirality flip.

powers of the muon Yukawa coupling, corresponding to $a_\mu(\text{N.P.}) \propto m_\mu^4/\Lambda^4$ at the one-loop level. Two-loop effects from Barr-Zee diagrams can be larger, but typically the contributions to a_μ are negligible in these models.

- Models with additional light particles with masses below the GeV-scale: examples are provided by the secluded U(1) model of Ref. [88] or the more general models discussed in Ref. [89], where additional light neutral gauge bosons can affect electromagnetic interactions. These models are difficult to study at the LHC, but they can lead to contributions to a_μ which are of the same order as the deviation in Eq. (32). Hence the new $g-2$ measurement will provide an important test of such models.

To summarize: many well-motivated models can accomodate larger contributions to a_μ — if any of these are realized $g-2$ can be used to constrain model parameters; many well-motivated new physics models give tiny contributions to a_μ and would be disfavored if the more precise $g-2$ measurement confirms the deviation in Eq. (32). There are also examples of models which lead to similar LHC signatures but which can be distinguished using $g-2$.

In the following we discuss in more detail how a_μ will be useful in understanding TeV-scale physics in the event that the LHC established the existence of physics beyond the standard model [90].

2. a_μ as a benchmark for models of new physics

It has been established that the LHC is sensitive to virtually all proposed weak-scale extensions of the standard model, ranging from supersymmetry (SUSY), extra dimensions

and technicolor to little Higgs models, unparticle physics, hidden sector models and others. However, even if the existence of physics beyond the standard model is established, it will be far from easy for the LHC alone to identify which of these — or not yet thought of — alternatives is realized. Typically LHC data will be consistent with several alternative models. The measurement of a_μ to 16×10^{-11} will be highly valuable in this respect since it will provide a benchmark and stringent selection criterion that can be imposed on any model that is tested at the LHC.

For example, a situation is possible where the LHC finds many new heavy particles which are compatible with both minimal-supersymmetric and universal-extra-dimension model predictions [91], or both minimal-supersymmetric and and Littlest Higgs model predictions [76]. The muon $g-2$ would especially aid in the selection since UED or Littlest Higgs models predict a tiny effect to a_μ, while SUSY effects are usually much larger.

On the other hand, a situation where the LHC finds no physics beyond the standard model but the a_μ measurement establishes a deviation, might be a signal for models such as the secluded U(1) model, with new light particles, or for unparticle physics effects, which are hard to identify at the LHC.

Next consider the situation that extra dimensions are realized in the form of a Randall-Sundrum or ADD model. In that case, the a_μ measurement will not only help to constrain model parameters. Since the a_μ predictions in these models strongly depend on the details of the physics of the extra dimensions, the a_μ measurement will also help to identify and test these details.

Within the framework of SUSY there are many different well-motivated scenarios that are not always easy to distinguish at the LHC. Fig. 19 shows a graphical distribution of the 10 Snowmass Points and Slopes model benchmark predictions [92] for a_μ(SUSY). They range considerably and can be positive and negative, due to the factor $\mathrm{sgn}(\mu)$ in Eq. 38, where this sign would be particularly difficult to determine at LHC, even if SUSY were to be discovered. The discriminating power of an improved $g-2$ measurement—even if the actual value of Δa_μ turned out to be smaller—is evident from Fig. 19.

A final example concerns the restriction of special, highly constrained models of new physics such as the constrained MSSM (CMSSM). The CMSSM has only four free continuous parameters. One precise measurement such as the future determination of Δa_μ effectively fixes one parameter as a function of the others and thus reduces the number of

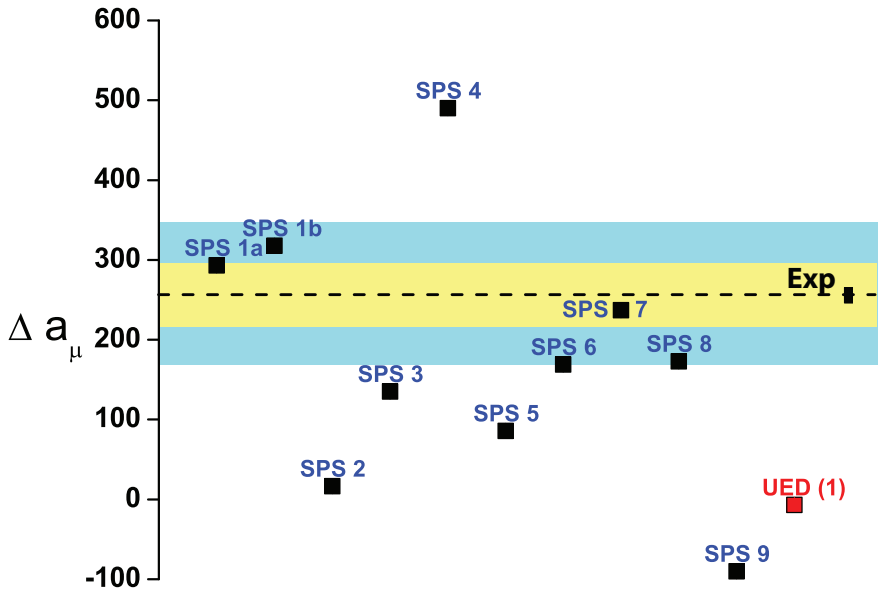

(a)

FIG. 19: The Snowmass Points and Slopes predictions for a_μ(SUSY) (in units of 10^{-11}) for various scenarios [92], and the UED prediction for one extra dimension [75]. (The horizontal axis has no meaning except to make all points visible.) The wide blue band is the present 1σ difference between experiment and theory, $\Delta a_\mu = (255 \pm 80) \times 10^{-11}$. The narrow yellow band represents the proposed improved precision ($\pm 34 \times 10^{-11}$), given the same central value. In both cases the error represents the quadrature between the experimental and theoretical errors.

free parameters by one. A large number of recent analyses have made use of this feature, see e.g. Refs. [93]. In fact, the CMSSM is very sensitive not only to the a_μ but also to the dark matter (which in this model is assumed to consist of neutralinos) relic density. As shown in Fig. 20, both observables lead to orthogonal constraints in CMSSM parameter space, and therefore imposing both constraints leaves only two free parameters and thus allows for very stringent tests of the CMSSM at the LHC. From Fig. 20(a) we see that in this model, there is little room left for $\tan\beta = 10$.

3. a_μ is sensitive to quantities that are difficult to measure at the LHC

For unraveling the mysteries of TeV-scale physics it is not sufficient to determine which type of new physics is realized, but it is necessary to determine model parameters as precisely

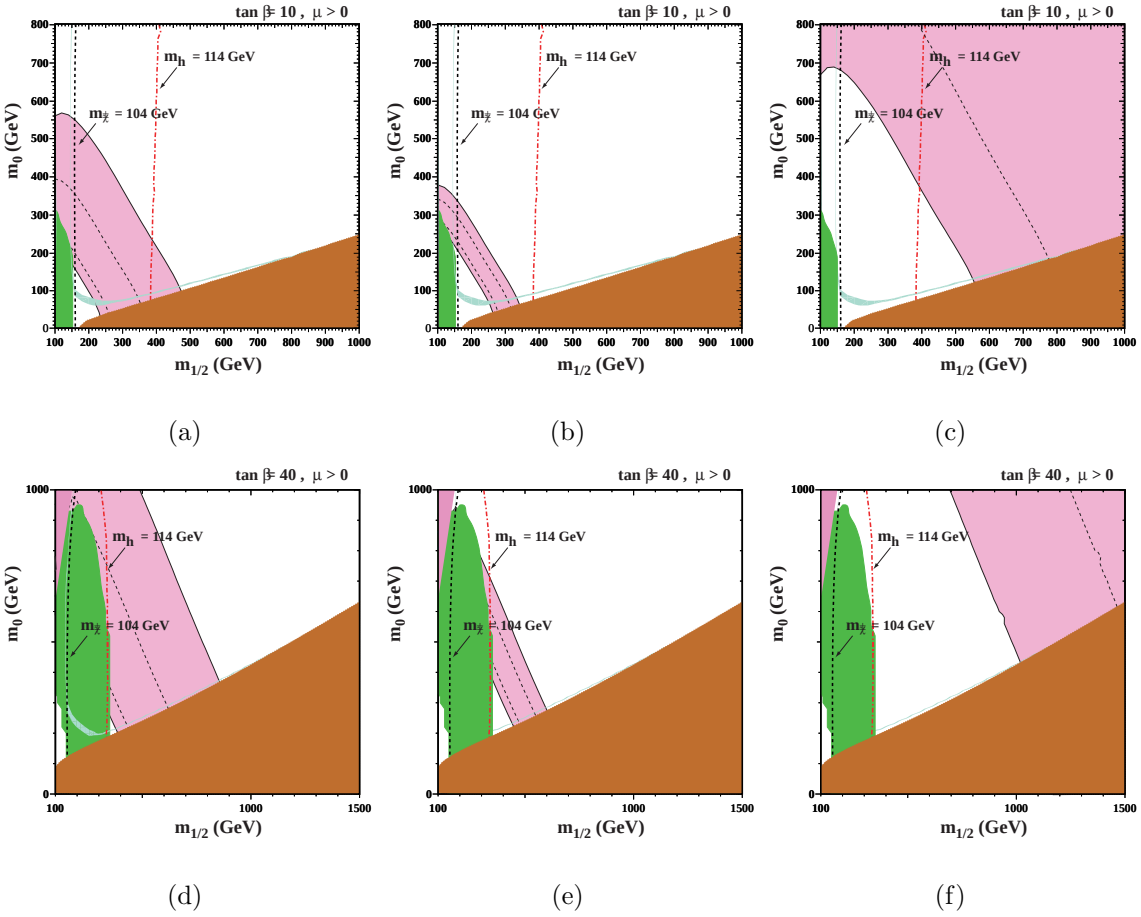

FIG. 20: The m_0(scalar mass)–$m_{1/2}$(gaugino mass) plane of the CMSSM parameter space for $\tan\beta = (10; 40)$, $A_0 = 0$, $\mathrm{sgn}(\mu) = +$:
(a;d) The $\Delta a_\mu^{(\mathrm{today})} = 255(80) \times 10^{-11}$ between experiment and standard-model theory is from Ref. [17]. The brown wedge on the lower right is excluded by the requirement the dark matter be neutral. Direct limits on the Higgs and chargino $\chi^\pm$ masses are indicated by vertical lines, with the region to the left excluded. Restrictions from the WMAP satellite data are shown as a light-blue line. The $(g-2)$ 1 and 2-standard deviation boundaries are shown in purple. The green region is excluded by $b \to s\gamma$. (b;e) The plot with $\Delta a_\mu = 255(34) \times 10^{-11}$. (c;f) The same errors as (b), but $\Delta a_\mu = 0$. (Figures courtesy of K. Olive, following Ref. [94])

as possible. Here the complementarity between the LHC and precision experiments such as a_μ becomes particularly important. A difficulty at the LHC is the indirect relation between LHC observables (cross sections, mass spectra, edges, etc) and model parameters such as masses and couplings, let alone more underlying parameters such as supersymmetry-breaking

parameters or the μ-parameter in the MSSM. Generally, the LHC Inverse problem [95] states that several different points in the supersymmetry parameter space can give rise to indistinguishable LHC signatures. It has been shown that a promising strategy is to determine the model parameters by performing a global fit of a model such as the MSSM to all available LHC data. However, recent investigations have revealed that in this way typically a multitude of almost degenerate local minima of χ^2 as a function of the model parameters results [96]. Independent observables such as the ones available at the proposed International Linear Collider [97] or $a_\mu$will be highly valuable to break such degeneracies, and in this way to unambiguously determine the model parameters.

In the following we provide further examples for the complementarity of LHC and a_μ for the well-studied case of the MSSM. Two central parameters which are related to electroweak symmetry breaking are the μ-parameter and $\tan\beta$, the ratio of the two Higgs vacuum expectation values. According to Eq. 38 the MSSM contributions to a_μ are highly sensitive to both sign(μ) and $\tan\beta$. Therefore, a future improved a_μ measurement has the potential to establish a definite positive or negative sign of the μ-parameter in the MSSM, which would be a crucial piece of information. The LHC has a weaker and less direct sensitivity to these two parameters. Combining LHC measurements with a_μ can lead to a good determination of $\tan\beta$.

One should note that even if better ways to determine $\tan\beta$ at the LHC alone might be found, an independent determination using a_μ will still be highly valuable, as $\tan\beta$ is one of the central MSSM parameters; it appears in all sectors and in almost all observables. In non-minimal SUSY models the relation between $\tan\beta$ and different observables can be modified. Therefore, measuring $\tan\beta$ in different ways, e.g. using certain Higgs- or b-decays at the LHC or at b-factories and using a_μ, would constitute a non-trivial and indispensable test of the universality of $\tan\beta$ and thus of the structure of the MSSM.

In the event that SUSY is discovered, we give an illustration of a $\tan\beta$ measurement and consider a case similar to the one discussed in Ref. [96]. We assume that the deviation $\Delta a_\mu = 255 \times 10^{-11}$ is real and that an MSSM parameter point SPS1a* is realized, where SPS1a* is defined in the same way as SPS1a [92] except that $\tan\beta = 8.5$. With this assumption, the comprehensive LHC-analysis of [96] for SPS1a can be taken over, and the LHC would find many SUSY particles and measure many SUSY parameters rather well. Only $\tan\beta$ can be determined rather poorly with an uncertainty of ± 4.5. In such a situation

one can study the MSSM prediction for a_μ as a function of $\tan\beta$ (all other parameters are known from the global fit to LHC data) and compare it to the measured value, in particular after an improved measurement. As can be seen from Fig. 21, using today's value for a_μ would improve the determination of $\tan\beta$, but the improvement will be even more impressive after a future more precise a_μ measurement. Should such a scenario unfold, as the SUSY masses become better measured, the measure of $\tan\beta$ from a_μ would improve further. A similar but more comprehensive study in [98], where a_μ has been incorporated into the global fit and error correlations can be controlled better, confirms this role of a_μ as an excellent observable to measure $\tan\beta$. In Ref. [98], the precision of $\tan\beta$ increases by a factor two already if today's a_μ is included in the fit, so a 3–4-fold improvement can be expected if LHC-data is combined with the future a_μ measurement.

At the 2007 Glasgow $g-2$ Workshop [61], Martin and Wells presented an update of their so-called "superconservative analysis" [100], where a very conservative 5σ band around the observed difference Eq. (32) and the general supersymmetric standard model are considered. Surprisingly, it could be shown that even this mild assumption leads to regions of parameter space which are excluded by $g-2$ and nothing else. Hence, $g-2$ provides complementary information to collider, dark matter, or other low-energy observables. An improved $g-2$ measurement will be very useful—independent of the actual numerical result.

In a similar spirit, Berger, Gainer, Hewett and Rizzo [101] discussed "supersymmetry without prejudice." First a large set of supersymmetry parameter points ("models") in a 19-dimensional parameter space was identified, which was in agreement with many important existing experimental and theoretical constraints. Then the implications for observables such as $g-2$ were studied. The result for $g-2$ was rather similar to Fig. 19, although the context was far more general: the entire range $a_\mu^{\rm SUSY} \sim (-100 \ldots +300) \times 10^{-11}$ was populated by a reasonable number of "models." Therefore, a precise measurement of $g-2$ to $\pm 16 \times 10^{-11}$ will be a crucial way to rule out a large fraction of models and thus determine supersymmetry parameters.

The anomalous magnetic moment of the muon is sensitive to contributions from a wide range of physics beyond the standard model. It will continue to place stringent restrictions on all of the models, both present and yet to be written down. Assuming that we will be so fortunate as to discover new phenomena in the LHC era, a_μ will constitute an indispensable tool to discriminate between very different types of new physics, especially since it is highly

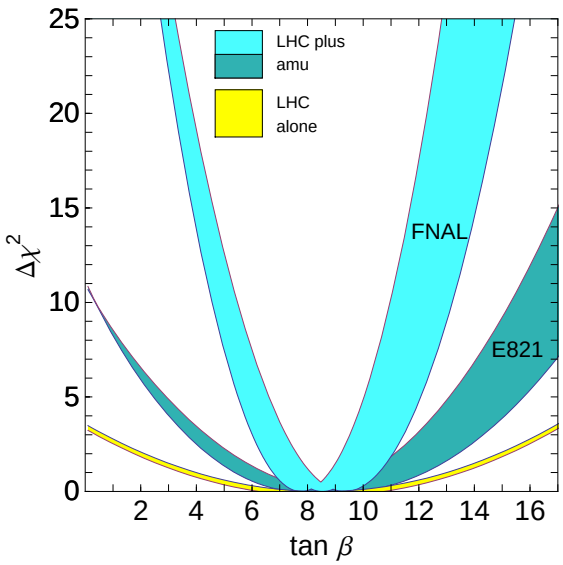

FIG. 21: Possible future $\tan\beta$ determination from the measurement of a_μ, assuming that the MSSM point SPS1a* (see text) is realized. The yellow band is from LHC alone which gives $\tan\beta^{\text{LHC fit}} = 8.5 \pm 4.5$, taking over the SPS1a analysis of Refs. [96, 98]. The darker blue band labelled E821 assumes $\Delta a_\mu = (255 \pm 80) \times 10^{-11}$, which comes from the present values for a_μ and the Standard-Model contribution, the lighter blue band labelled FNAL corresponds to $\Delta a_\mu^{\text{future}} = (255 \pm 34) \times 10^{-11}$. The blue bands show $\Delta\chi^2 = \left(\frac{a_\mu^{MSSM}(\tan\beta) - a_\mu^{\text{exp}}}{\{80;34\}\times 10^{-11}} \right)^2$ as a function of $\tan\beta$, where in $a_\mu^{\text{MSSM}}(\tan\beta)$ all parameters except $\tan\beta$ have been set to the values determined at the LHC. The width of the blue curves results from the expected LHC-uncertainty of the parameters (mainly smuon masses and M_2, μ) [98]. The plot shows that the precision for $\tan\beta$ that can be obtained using a_μ is limited by the precision of the other input parameters but is still much better than the determination using LHC data alone.

sensitive to parameters which are difficult to measure at the LHC. If we are unfortunate, then it represents one of the few ways to probe physics beyond the standard model. In either case, it will play an essential and complementary role in the quest to understand physics beyond the standard model at the TeV scale. This prospect is what motivates our collaboration to push forward with a new measurement.

IV. A NEW $(g-2)$ EXPERIMENT

A. Scientific Goal

The E821 results were based on three $\sim$ 2-month-long running periods in 1999, 2000, and 2001. A total of 8.55×10^9 events were included in the final fitted samples. Combined, this leads to a relative statistical uncertainty of 0.46 ppm. The systematic uncertainties were, in general, reduced in each running year, and a final combined averages for the magnetic field measurement (0.17 ppm) and spin-precession analysis (0.21 ppm) were combined in quadrature with the statistical error to obtain the final overall relative uncertainty of 0.54 ppm. In absolute units, the experimental uncertainty on a_μ is 63×10^{-11}.

The goal of the New $g-2$ Experiment is a precision improvement on a_μ by a factor of 4 to $\delta a_\mu = 16 \times 10^{-11}$, (0.14 ppm). This is arrived at by assuming roughly equal statistical and systematic uncertainty goals. At $\delta a_\mu = 16 \times 10^{-11}$, the uncertainty will be well below the theoretical error. In consultation with theorists who evaluate the SM contributions, we estimate that existing and future HVP input data sets will reduce the uncertainty from 49 to 30 in 10^{-11} units. Our experimental precision will remain better than theory, barring unforseen breakthroughs. Assuming a theory error of 30×10^{-11}, the uncertainty on the comparison between experiment and theory, Δa_μ, will be reduced to 34×10^{-11}. This low-energy precision SM test will provide a powerful discriminator of new physics models.

An improvement by a factor of 4 is both scientifically compelling and technically achievable. To do so in less than 2 years of running, will require use of 6/20 of the Booster batches, each subdivided fourfold leading to 18 Hz of storage ring fills (4 times the fill frequency at BNL). The use of a long decay beamline, with true-forward decay kinematics and an open inflector magnet, will serve to improve the muon storage efficiency per proton by a factor of more than 6. A significant reduction in background will result from the long beamline. The design of the experiment aims at a systematic error reduction by an overall factor of 3. The plan described below will achieve these stated goals.

B. Key Elements to a New Experiment

The New $g-2$ Experiment relies on the following improvements compared to the BNL E821 Experiment:

1. Increasing the stored muon flux per incident proton,

2. Increasing the fill frequency (lowers the instantaneous rate),

3. Decreasing the hadron-induced flash at injection,

4. Improving the stored muon beam dynamics with a better kick into the ring and with a damping scheme to reduce coherent betatron oscillations,

5. Improving the storage ring field uniformity and the measurement and calibration system,

6. Increasing the detector segmentation to reduce the instantaneous rate.

Items $1-3$ will be realized by a clever use of the present Fermilab accelerator complex. A single 8-GeV Booster batch will be injected into the Recycler, where it will be subdivided into 4 bunches; 6 of the 20 batches per 15 Hz Booster cycle provide 24 individual bunches of 10^{12} protons. Each bunch is directed to the antiproton target area to produce 3.1 GeV/c positive pions, which will be focussed by a new rad-hard lens system and dipole magnet into the AP2 transfer line. The quadrupole density in the 270-m long AP2 line will be increased by a factor of 3 to reduce the beta function and consequently capture and transport a high fraction of forward-decay muons. The muon beam will go around the Debuncher ring for nearly one full turn, then be extracted into the AP3 channel—also enhanced by additional quadrupoles—and then directed into a new building located close to AP0. A new, short, transfer line will direct the beam into the storage ring through a new open-ended inflector magnet. In subsection IV C we discuss how the background from the injection flash will be reduced.

Item 4 will be approached by optimization of the storage ring kicker pulse and possible implementation of a damping scheme to reduce muon betatron oscillations. We discuss this complex subject in Appendix B.

Item 5 involves the magnetic field. As the ring is rebuilt for Fermilab, an extra degree of effort will be required to shim the field to a higher level of uniformity. To meet the stringent demands of the systematic error goal for this measurement, some R&D projects will be required, as detailed in the Field section. Additionally, an improved positron traceback system of detectors will be required to image the beam for folding together with the field maps to obtain the muon-averaged magnetic field.

Finally, for item 6, we detail a plan to segment the positron detector system to reduce pileup. Further, a new electronics and DAQ system will be capable of storing events having lower electron energies.

C. The Expected Flash at Fermilab

At BNL, one key limitation to simply increasing the rate was the hadronic flash that was induced by pions entering the ring at injection. These pions struck the detectors, vacuum chambers, and the magnet steel, producing neutrons, which thermalized with a time constant close to the time-dilated muon lifetime. In the calorimeters, neutron-capture gamma rays led to a slowly decaying baseline shift in the light reaching the PMTs. Positron signals then had to be extracted with respect to a time-dependent baseline. The baseline shift affected a number of systematic errors, which we expect to be largely absent in the new experiment. The prompt flash—the short burst of direct background in the detectors at injection—required us to gate off all detectors during injection and turn them back on some $5-15$ μs later. The slow neutron capture produced a baseline shift that was evident for 10's of μs afterward. To estimate the flash for Fermilab, we consider four differences in operation between BNL and Fermilab.

- At BNL, the proton intensity per storage ring fill was $\sim 4 \times 10^{12}$. At FNAL, it will be 1×10^{12} (intensity factor = 4).

- At BNL, the proton beam energy was 24 GeV; at FNAL it is 8 GeV. The pion production yield is approximately 2.5 times higher at BNL. (pion-yield factor = 2.5).

- The FNAL pion decay beamline will be $\sim$ 800 m longer compared to BNL. With a decay length for 3.1 GeV/c pions of 173 m, the difference represents a reduction by a factor of 100 in undecayed pions at FNAL compared to at BNL (decay factor = 100).

- To improve the ratio of injected muons to pions at BNL, the ratio of upstream pion-selection momentum to final muon magic momentum, (P_π/P_μ), was set to 1.017. This reduced the pion flux by 50 (and the muon flux by $\sim 3-4$). For FNAL the ideal ratio of $P_\pi/P_\mu = 1.005$ will be used. The asymmetric BNL setting reduced the transmitted undecayed pions compared to anticipated FNAL equivalent settings (P_π/P_μ factor = 0.02).

The flash is based on the pion flux entering the ring per storage ring fill (not on the stored muon rate). The four factors above—intensity, pion yield, decay, P_π/P_μ—multiply: $4 \times 2.5 \times 100 \times 0.02 = 20$. This implies that the flash will be 20 times smaller at Fermilab in the new experiment compared to BNL.

D. Event Rate and POT Request Calculation

A preliminary estimate of the event rate and therefore total proton-on-target (POT) request required for acquiring the 1.8×10^{11} events is outlined in Table VII. Up to the target, we used known factors for proton beam delivery as outlined in this proposal. A pion production calculation using MARS [102] was made to estimate the number of 3.1 GeV/c pions emitted into the accepted phase space of the AP2 line. From this point, a conservative approach was to compare known factors between the muon capture and transmission at Fermilab to those same factors at BNL. Many of the factors are relatively trivial to compute, while others rely on our detailed Decay Turtle simulations of the BNL lattice and modifications of this lattice for Fermilab. We are in the process of a complete end-to-end calculation of the beamline, but this work will take additional time. In the comparison to BNL approach, we find the important increase of stored muons per incident proton of 11.5; whereas, we require a factor of at least 6 for an experiment that can be done in less than 2 years. We use the factor of 6 in our beam estimates, thus introducing a "beam-time contingency" factor of nearly 100% from the beginning. Experience from E821 suggests that $4 - 6$ weeks of setup time with beam will be required before "good" data are obtained. We also assume that 66% of the data taking period will result in the final statistics—this allows for regular magnet mapping intervals, systematic runs, calibration runs, and normal experimental downtime. The origin of each factor in Table VII, is explained in a series of notes following the Table.

TABLE VII: Event rate calculation using known factors and a comparison to the realized stored muon fraction at BNL.

Item	**Factor**	**Net**	**Note**
Booster cycle - 15 Hz operation	1.33 s/cycle	0.75 Hz	1
Batches to $g-2$	6	4.51 Hz	2
Protons on target	4×10^{12} p/batch	1.80×10^{13} p/s	3
Bunches (each bunch provides 1 fill of the ring)	4 /batch	18 fills/s	4
BNL stored muons per proton	1×10^{-9} μ/p	1000 μ/Tp	5
Minimum stored μ/p improvement FNAL *vs.* BNL	6.0	6000 μ/Tp	6
Positrons with $t > 30$ μs and $E > 1.8$ GeV	10 %	603 e^+/fill	7
DAQ / Expt. production and uptime	66 %		8
Time to collect 1.8×10^{11} events (2×10^7s/y)		1.25 years	9
Commissioning time		0.1 years	10
FNAL running years		1.35 years	11
Total Protons on Target		4×10^{20} **POT**	12

Notes explaining entries in Table VII:

1. 15 Hz Booster operation is assumed.

2. Neutrino program uses 12 out of 20 batches; 8 out of 20 are in principle available, but 6 should be clean for use by the muon program. Batches are injected into the Recycler with 66 ms spacing.

3. Standard expected proton intensity per batch.

4. Subdivision in Recycler of each batch into 4 "bunches" with roughly equal intensity. Each is extracted separately with $\sim$ 12 ms spacing and each initiates a storage ring "fill."

5. Measured stored muon fraction per 24-GeV proton on target at BNL per 10^{12} p (Tp). This number folds up individual factors including the inflector transmission and the storage ring kicker efficiency.

6. The improvement is done comparing to the known situation at BNL. We arrive at the following factors: $\times 0.4$ for the reduced pion yield; $\times 1.8$ for the AP2 line with smaller

beta function; $\times 2$ for the longer decay channel; $\times 3$ for the forward decay optimal muon tune; $\times 1.33$ for opening up the pion momentum acceptance; $\times 2$ for the open inflector and improved kicker = 11.5. We use a factor of 6 to be very conservative. See details in Section V H.

7. Product of 16% acceptance from GEANT Monte Carlo for decay positrons having energy greater than 1.8 GeV and muon population reduction from injection to the expected fit start time at $t = 30$ μs.

8. Expected global uptime fraction, which includes time for magnetic field mapping, systematic error studies, calibration runs, and normal equipment malfunction.

9. With above factors, and using 2×10^7 s of delivered beam per FNAL year.

10. Estimate of setup time with beam on.

11. Total running.

12. Request POT under above conditions. Actual needs will depend on completed beam design.

V. ACCELERATOR PREPARATIONS

The Proton Plan and the NOνA Project at Fermilab will allow the Main Injector to run with a 1.333 s cycle time for its neutrino program (NuMI), with twelve batches of beam from the Booster being accumulated in the Recycler and single-turn injected at the beginning of the MI cycle. Thus, there remain eight Booster cycles during each MI period that could in principle be used for an 8 GeV (kinetic energy) [148] beam experimental program. Under the Proton Plan [103], the maximum average Booster repetition rate has been increased from roughly 2.5 Hz to 9 Hz. While not required for the NuMI program, a further upgrade to the Booster RF system remains necessary to allow the Booster to run at its maximum rate of 15 Hz. This upgrade is required for any use of the Booster for programs complementary to the neutrino program and in subsequent subsections we will assume this has been performed. Additionally the per cycle intensity may be greater with these upgrades, but for purposes of this discussion we will use a typical 4×10^{12} protons (4 Tp) per Booster batch.

Beam for the $g-2$ experiment is to be transferred directly into the Recycler ring from the Booster and out of the Recycler into the P1 transport line. At the moment these functions are performed directly to and from the Main Injector. However, the NOνA project also requires injection into the Recycler from the Booster, and so it will be assumed for our discussion that this functionality has been achieved at the end of that project. Extraction from the Recycler and delivery to the P1 beam line is required, with costs similar to the aforementioned injection system.

The Debuncher, Accumulator, and Recycler rings all have equipment installed to perform stochastic cooling (and, in the Recycler, electron cooling) which can and should be removed to generate less aperture restrictions for the high intensity operations of any 8 GeV experimental program. Removal of Recycler components is performed as part of the NOνA project.

Particle losses in the Booster are currently observed over a 100 s running average as detected by the beam loss monitor system and limit the beam delivered by the synchrotron to about 1.6×10^{17} protons/hour. Comparatively, 15 Hz operation at 4 Tp per batch would produce roughly 2.2×10^{17} protons per hour. It is expected that the new magnetic corrector system, the installation of which was completed in 2009 under the Proton Plan and is still being fully commissioned, will allow for this increased intensity under 15 Hz operation.

Table VIII outlines the scope of the work to be performed for implementation of the New $g-2$ Experiment at Fermilab.

TABLE VIII: Scope of accelerator system modifications required of accelerator systems.

Accel/BmL	System	Note
Booster	RF	upgrade to 15 Hz operation
Recycler	inj line	from MI-8 to RR
Recycler	ext line	from RR to P-1 line
Recycler	cooling	remove stoch/e^- cooling systems
Recycler	ext line	extraction kicker
Recycler	RF	system move from MI, upgrades
AP0	target station	possible new optics, lens upgrades
Expt Hall	building	new construction
Expt Hall	cryo	tie in with Tevatron system
transf. lines	Rad. Safety	mitigation near new building
Rings, transf. lines	Instr/Controls	possible BPM upgrade

A. Meeting the Experimental Requirements

The $g-2$ experiment requires 3.09 GeV/c muons injected into an existing muon storage ring that would be relocated from Brookhaven National Laboratory to Fermilab. The muon storage ring is 7.1 m in radius, giving a revolution time of 149 ns. To account for the injection kicker, the beam pulses need to have RMS lengths of about 50 ns or less. These pulses should be separated on the scale of about 10 ms for the muons to decay in the ring and data to be recorded prior to the next injection. To obtain as pure a muon beam as possible entering the storage ring, the experiment would like a decay channel corresponding to several pion decay lengths, where $c\beta\gamma\tau_\pi = 173$ m. Present understanding of the pion yield, the transfer line acceptance, and the muon storage fraction support the idea that the 21$\times$ more statistics can be obtained in less then 2 years of running.

To meet the above requirements it is envisioned that six Booster batches every MI cycle can be sent to the experiment for an average rate of $6/20 \times 4$ Tp $\times$ 15/s = 18 Tp/s. This yields the required total protons on target. Each batch of 53 MHz bunches from the Booster would be sent to the Recycler and formed into four bunches for delivery to the experiment. Using relocated existing RF systems, possibly supplemented with like-kind components, the four bunches can be formed to meet the demands of the $g-2$ ring. The re-bunching process takes approximately 30 ms, and the four bunches would then be delivered to the experiment one at a time spaced by 12 ms. Thus, the last bunch is extracted just within the 66.7 ms Booster cycle. The remaining two Booster cycles, before and after this process, allow for pre-pulsing of fast devices prior to the change between NuMI and "muon" cycles. (If this is deemed unnecessary, then eight rather than six Booster cycles could feed the experiment during each MI cycle.) Figure 22 shows the proposed time line of events during MI operation.

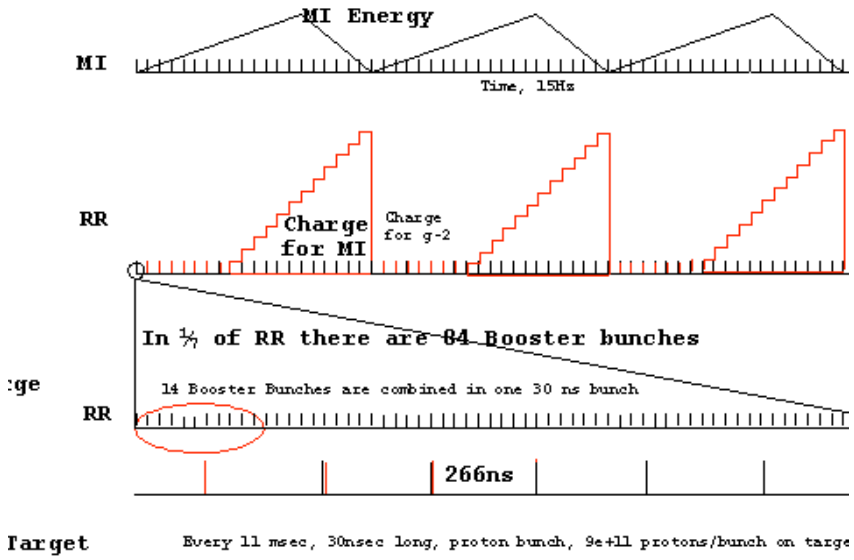

FIG. 22: Timing diagram for the proposed g-2 operation.

Once extracted from the Recycler, a bunch is sent toward the existing, though possibly modified, antiproton target station for $\sim$3.11 GeV/c pion production. A "boomerang" approach utilizing the Debuncher and Accumulator rings can be used as a decay line allowing for pion to muon decay, assuming a final location of the g-2 ring in the vicinity of the

production target. A schematic of the beam line system is presented in Figure 23. The total

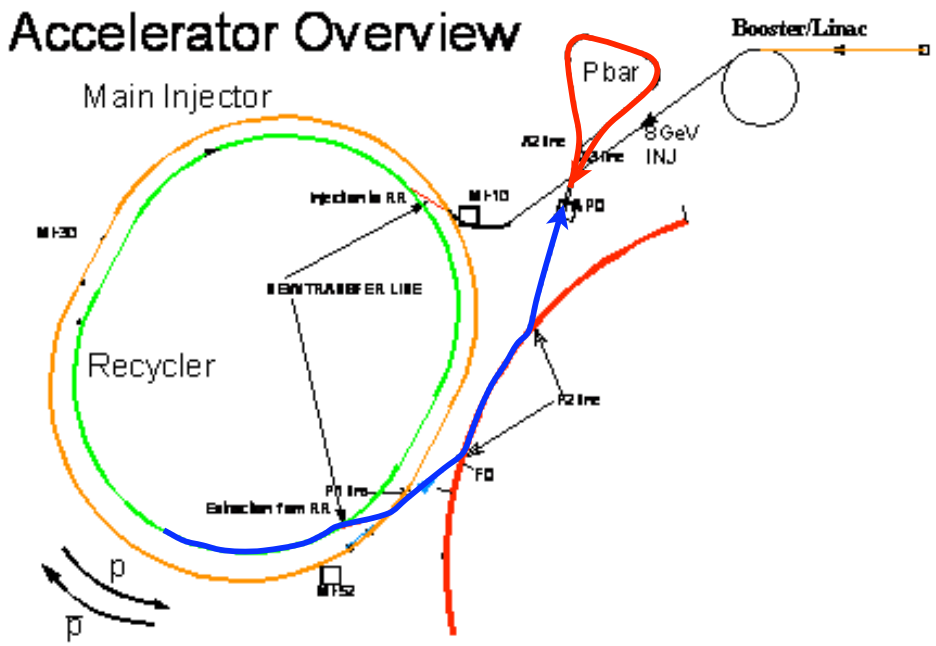

FIG. 23: Beam transport scheme for g-2 operation. Beam is prepared in the Recycler, exits via the P1 line, passes through the Tevatron tunnel into the AP1 beam line, and to the AP0 target area. (Blue curve.) Pions, decaying to muons, are transported from the target through the AP2 line, once around the "pbar" rings (Debuncher/Accumulator) and back toward the experimental hall near AP0 via the AP3 beam line. (Thick red curve.)

length of the decay line would be ∼900 m. To obtain even further purity of the muon beam, multiple revolutions in the Debuncher or Accumulator rings could be considered, perhaps as an upgrade to the program. This upgrade would require the development of an appropriate kicker system and is not included in this first design iteration. The 900 m decay length, however, is already a large improvement over the original layout at BNL.

B. Bunch Formation

The major proton beam preparation will be performed in the Recycler ring. A broadband RF system like that already installed in the Recycler would be used, except twice the voltage may be required. The 2.5 MHz (max. $V_{rf} = 60$ kV) and 5 MHz (max. $V_{rf} = 15$ kV) RF

systems that presently reside in the MI would be relocated to the Recycler. Upgrades to increase their maximum voltages by roughly 10-30% may be required. All of these upgrades are assumed for the cost estimate.

As described in [104], the bunching scheme is to use a four period sawtooth wave form across the Booster batch produced by the broadband RF system to break the batch into four segments and rotate them in phase space sufficiently that they can be captured cleanly in a linearized bucket provided by the resonant RF. Each of the four resulting bunches has an RMS length of ∼50 ns. The first bunch is extracted immediately and the latter three are extracted sequentially at half periods of the synchrotron oscillation. The beam loading of the resonant cavities will be considerable, and further details need to be considered. It is plausible to expect that a feedforward system can be developed without serious difficulty. A combination of feedback with feedforward is potentially better yet, but feedforward will be required with or without feedback. Figure 24 shows the resulting beam structure in the

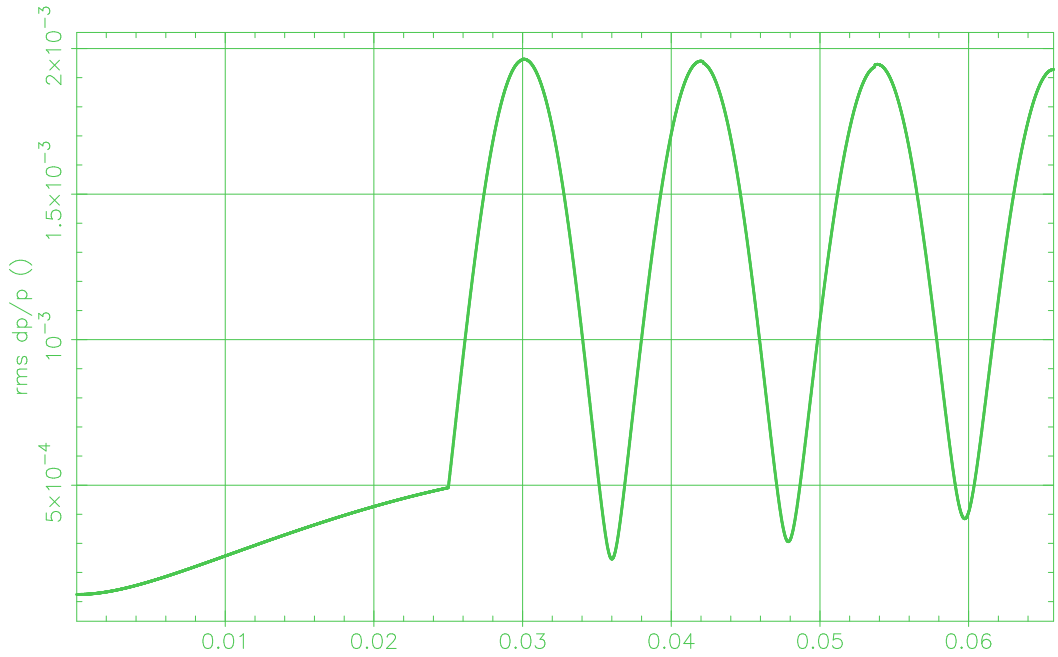

FIG. 24: Resulting relative momentum spread ($\Delta p/p$) *vs.* time in seconds following injection into the Recycler. After an initial phase using the broadband RF system, beam is captured into four buckets. The beam rotates within the four buckets with period 12 ms and is extracted one-by-one as the momentum spread reaches its peak (pulse length is at its shortest).

Recycler if the beam were not extracted. The plan would be to extract one pulse at a time, every 12 ms, when the bunches are at their narrowest time extent (4σ widths of 38-58 ns). The four bunches would be separated by roughly 400 ns center-to-center. For the sequence shown, the RF systems require voltages of 4 kV (broadband), 80 kV (2.5 MHz), and 16 kV (5.0 MHz). A longitudinal emittance of 0.07 eV-s per 53 MHz Booster bunch was assumed.

C. Beam Delivery and Transfer

Following the beam trajectory starting with extraction from the Booster, we see that the proton beam needs to be injected into the Recycler from the MI-8 beam line at the MI-10 region of the Main Injector tunnel. This maneuver will be facilitated through the NOνA project, which requires the same injection procedure. Once prepared with the RF systems as described above, the beam will need to be extracted from the Recycler and injected into the P1 beam line. The extraction location is at the MI-52 tunnel location, where the Main Injector ties into this same beam line. (See Figure 23.) The P1 beam line is used to deliver 8 GeV antiprotons from the Accumulator into the Main Injector (and on into the Recycler) in the reverse direction. During the $g-2$ operation, however, the Main Injector will contain beam destined for NuMI and so this region will need to be modified in almost exactly the same way as MI-10 to transport protons directly into the P1 line from the Recycler.

An appropriate kicker system will also be required for this region to extract one-by-one the four proton bunches from the Recycler. The four bunches will be separated by approximately 200 ns, so the kicker must rise in $\sim$180 ns and have a flat top of $\sim$50 ns. The Recycler has a circumference seven times that of the Booster, and only one Booster batch will be injected at a time. Thus, the last proton bunch of the four will be separated from the first by about 8.6 μs or more. The kicker can then have a fall time on the order of 5 μs, and must be pulsed 4 times separated by 10 ms within a Booster cycle. This operation is repeated 6 times every 1.33 s MI cycle.

From the entrance of the P1 line through the Tevatron injection Lambertson (which is kept off during this operation) the beam is directed through the P2 line (physically located in the Tevatron tunnel) and into the AP1 line toward the AP0 target hall. Again, since this system is run at 8 GeV for antiproton operations, no modifications are required for beam transport in $g-2$ operations. After targeting, which is discussed in the next subsection,

3.1 GeV/c pions are collected into the AP2 line which is "retuned" to operate at 3.1 GeV/c rather than today's 8.89 GeV/c antiproton operation.

To obtain a long decay channel for the pions off the target, the beam is transported through the AP2 line, into the Debuncher ring, and, through a new short transfer line, into the AP3 line, and directed back toward AP0. (See Figure 23 again.) As this will be the only use of these rings, kicker magnets will not be required in this configuration, and the Debuncher will be "partially powered" using only those magnet strings required to perform the "boomerang." Either corrector magnets or DC powered trim magnets will be used in place of kickers to perform the injection/extraction between the partially powered rings and associated beam lines. The $g-2$ ring will be located on the surface near the AP0 service building as indicated in Figure 25.

FIG. 25: Proposed location of the new $g-2$ experimental hall (yellow).

D. Target Station

Use of the existing AP0 target more-or-less "as is" – Plan B – would appear to be a straightforward approach. The present system is used for selecting 8.9 GeV/c antiprotons from a 120 GeV/c primary proton beam. For $g-2$ one would select $\sim$ 3.1 GeV/c pions

from 8.9 GeV/c primary protons by re-tuning the beam lines upstream and downstream of the target. The major issues with this particular scenario is the use of the existing Lithium lens, critical for antiproton production at 120 GeV/c, and the use of the existing pulsed bending magnet just downstream of the lens. Both of these devices are pulsed once every 2.2 s during antiproton operation.

Fermilab has over 25 years of experience using a lithium lens and pulsed dipole magnet in the target vault for antiproton production. The lens, which pulses approximately 62 kA into the primary of a current transformer ($\times 8$ in the secondary coil), produces a 400 ns-wide pulse every 2.2 s at its present operating condition. The heat load on the lens system from ohmic heating at this current is $\sim$4 kW, while the heating from the beam — operating at a beam power of 70-75 kW — is $\sim$2 kW. The capacity of the system is on the order of 10-11 kW.

Simply scaling the beam line elements from 8.9 GeV/c operation to 3.1 GeV/c operation yields a factor of 1/2.8 less current necessary for the lens, or 1/8 of today's power. The ohmic heat load at 2.2 s cycle time would thus become 490 W. Scaling from these conditions to the $g-2$ experiment's baseline of 18 Hz, with 25 kW beam power, the total load would be 20 kW, or twice the system capacity. Reducing the power by another factor of 2 (or, current by another 30%), would reduce the total heat load to just under 10 kW, within the present system's capabilities. There is some adjustment possible in cooling water flow as well.

At this further-reduced current, it is estimated that the pion yield would be reduced from the original estimates by $\sim$27%, assuming the lens is positioned further from the target at its longer focal length. Thus, the run-time of the experiment would be extended accordingly, all else being held constant, in this scenario.

The lens, its transformer, and the pulsed dipole magnet could all be used with appropriate power supplies to run them at the much-increased frequency. The costs of the magnetic elements are well known. Work has been performed in the Accelerator Division at Fermilab to scope out the costs of the required power systems. Estimates are provided in the cost tables, representing actual design elements to produce the bursts of 80 Hz pulses at an average rate of 18 Hz for the experiment.

The collaboration's favored plan – Plan A – is being developed for the target area for $g-2$ in which the pulsed lens and magnet system would be replaced by a set of radiation-hard

magnetic elements that could run at DC currents. This was the approach taken at BNL for $g-2$, where the average beam power on target was three times higher and in which the magnets survived this radiation environment for the life of the experiment there. Figure 26 shows a plan view of the Fermilab target vault at AP0. The 32.25-in wide by 10.75-in-long

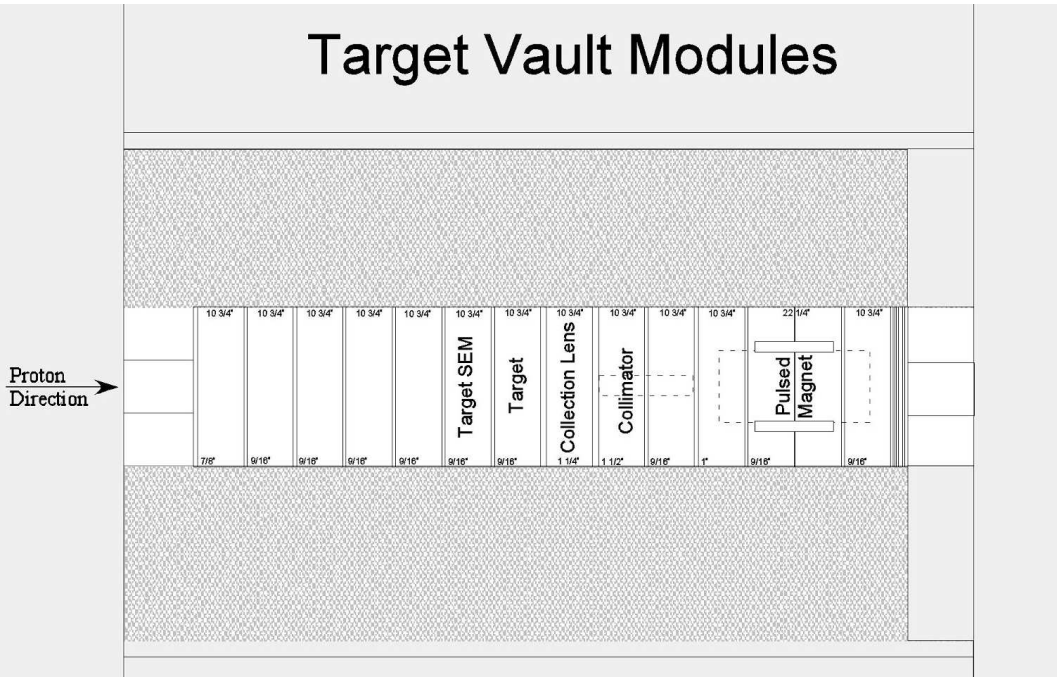

FIG. 26: Schematic layout of the AP0 target vault at Fermilab, with present module uses identified.

modules hold the various elements in place from above. Within this available space one could conceive of placing the target (presently at the middle of the vault) at the most upstream position followed by a quadrupole doublet made of radiation-hard components as was done at BNL. In fact, the length and width of the BNL magnets are small enough to fit inside the space provided, and the design for these magnets is available. A DC dipole magnet would then be placed with its bend center in the same location as the center of today's pulsed magnet to set the trajectory downstream.

A preliminary layout using BNL-style quadrupoles has been performed, as indicated in Figure 27.

While all of the equipment used in the BNL $g-2$ experiment is available for use in the Fermilab version, these first two quadrupoles – Q1 and Q2 – are activated and very likely would not be transported to Fermilab and used in the initial running of the experiment

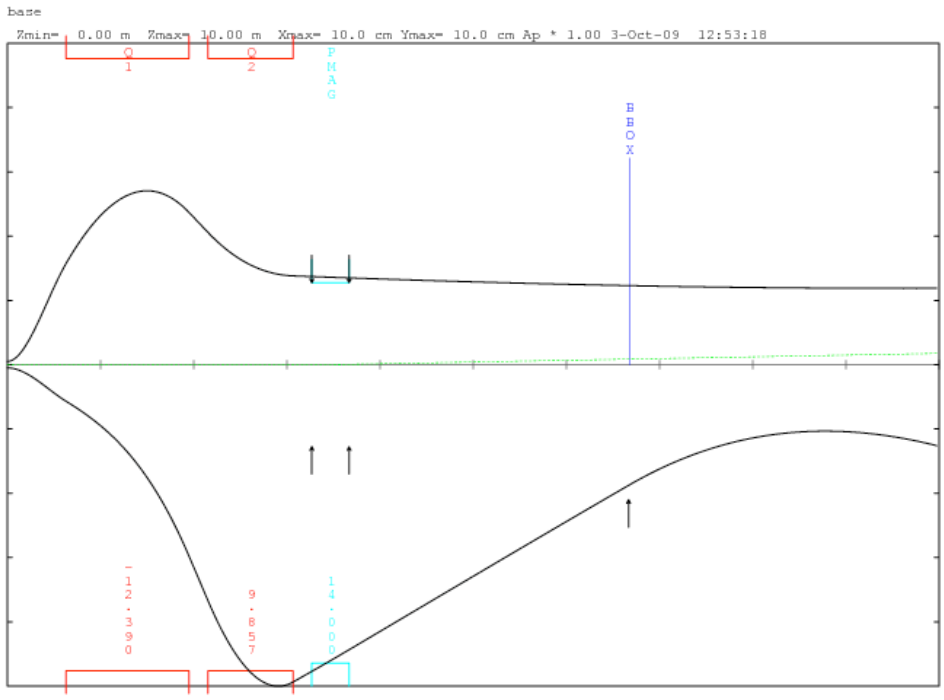

FIG. 27: Optics calculation showing beam envelope from the target through a quadrupole doublet, using the BNL experiment's magnet parameters. The required location of the 3-degree bend magnet is shown just to the right of the quads. The aperture of the current PMAG is indicated by the arrows. Its horizontal width would have to be increased as indicated, while the current gap is sufficient.

here. However, advantage could be taken of the existing designs, drawings and actual costs of these quadrupoles once a preferred optical layout is obtained.

This newer plan would be the preferred solution if an appropriate design can be worked out over the upcoming months, which in fact looks very feasible. Both plans are likely similar in cost, where one is trading low magnet costs but high power supply costs in Plan B for larger magnet costs but lower power supply costs in Plan A. A major benefit of Plan A would be the potential for better reliability and less maintenance for a DC system. But Plan B is a better understood system at this point and presents only a small hit on run

time. It could turn out to be appropriate to begin $g-2$ running with a Plan B target system using mostly lens equipment that exists at the end of Tevatron Run II, followed by an early upgrade to Plan A for full production running.

E. Target to Debuncher

The current AP2 lattice has a large transverse (unnormalized) acceptance of about 35 mm-mrad in both planes, which matches well to either the Li lens or the quadrupole collection of pions from the target region. The lattice for this line has been translated into MAD, TRANSPORT and DECAY TURTLE input decks and is shown in Figure 28, top panel. As described elsewhere, for the generation of muons with $p_\mu = 3.094$ GeV/c in pure forward decay kinematics an initial pion momentum of $p_\pi = 1.005 p_\mu$ is required. However, pions with 3-4% higher momenta decaying with muon angles of several mrad can still contribute to the magic muon flux. Thus, in order to increase the muon flux, (i) the FODO beta function; i.e. the pion beam size, should be decreased in the decay region and (ii) a momentum bin of $\pm 2\%$ should be accepted by the lattice. Modifying the beta function reduces the pion beam size in the decay FODO, so that larger decay angles still remain within the acceptance of the $g-2$ ring. The momentum acceptance is limited by second order chromatic effects, where a large aperture Q1, Q2 collection system is likely to be less efficient than the Li lens, which demonstrated 2.5% momentum acceptance as an antiproton source. The quadrupole option, on the other hand is likely to have a higher overall acceptance in the transverse plane. One should emphasize that these FODO changes are required only for the decay region, because their importance is weighted by $e^{-z/L}$, where $L = 173$ m is the decay length of pions of p_μ. Thus reducing the beta function in the first $\sim$150 m long straight section of the AP2 line is most important, followed by the second straight FODO extending to 290 m, before the beam enters the Debuncher. From this point on, only a small fraction of muons are produced and no changes to the Debuncher lattice are required for this purpose.

The properties of the target region, the decay lattice design and the transport to and injection into the $g-2$ ring are tightly coupled, so that a full end-to-end simulation is required. The collaboration has made significant progress in this direction by forming a beam team between members of the Fermilab Accelerator Division, the antiproton group and the

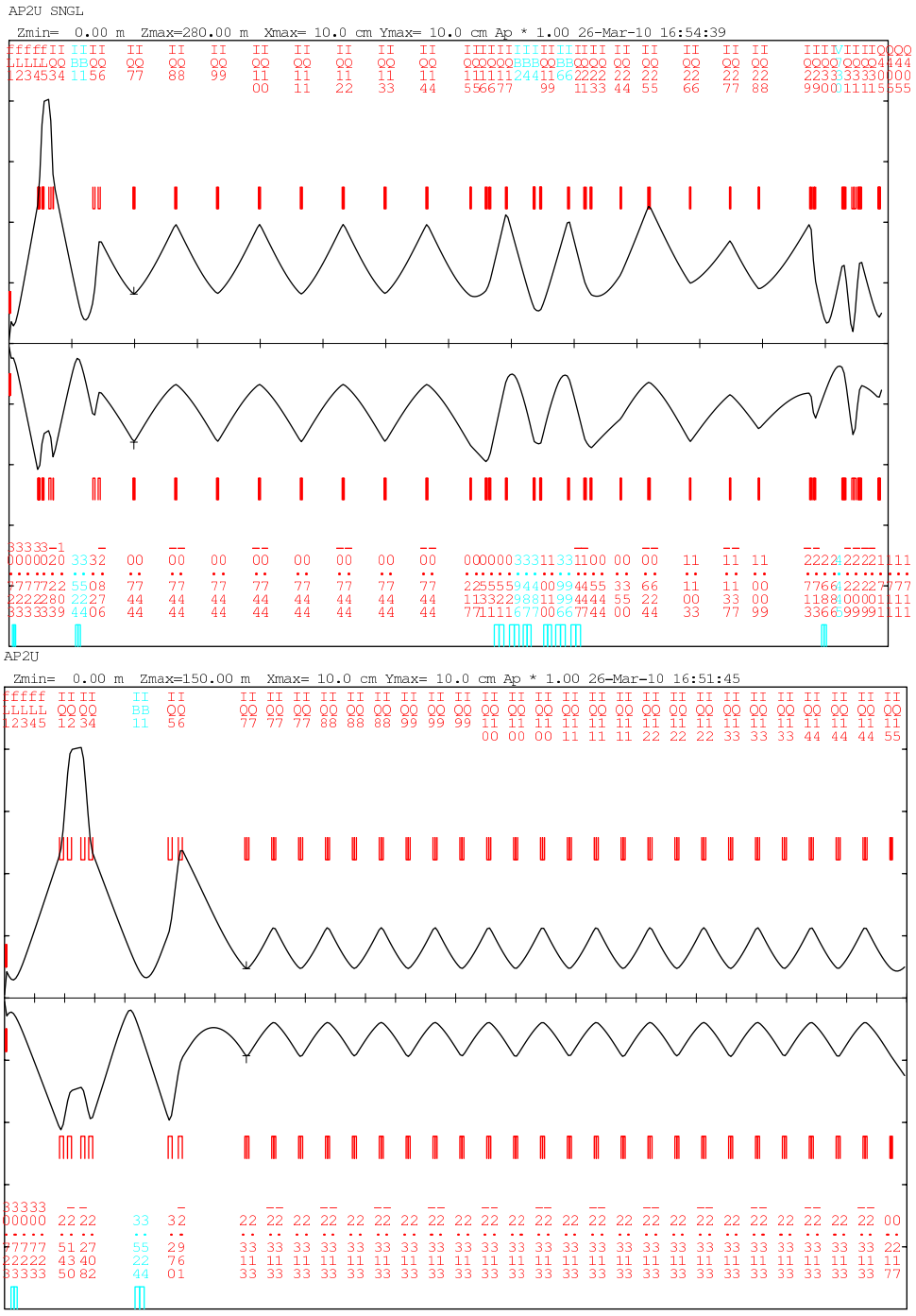

FIG. 28: Beam envelope of present AP2 line (top) and modified AP2 beam line (bottom), with triplet lattice spacing in first straight FODO section. The line depicted in the top panel is the full AP2 280m long, the bottom panel is the first AP2 FODO up to 150m. The TRANSPORT display shows the beam envelopes in the y-plane above and the x-plane below the abscissa. The ordinate range corresponds to 10 cm. The schematic layout of the triplet lattice (bottom figure) is for costing purpose. The labels denote beam line elements and pole tip fields in kG.

universities, where new work has been presented and discussed in weekly teleconferences. For the AP2 lattice we have considered increasing the number of quadrupoles by factors of 2-4, in order to reduce the lattice spacing and beta function. At the moment, tripling the number of quads appears like a good compromise and a preliminary lattice design has been made for this case. (See Figure 28, bottom panel.) This lattice has been simulated with a full DECAY TURTLE calculation confirming that accepted muon flux is approximately increased 3-fold compared to the existing AP2. More systematic studies including Plans A and B, different lattice spacings, denser lattice in the second AP2 straight section, including wider momentum bins, *etc.*, are currently intensively studied. For instrumenting both straight sections of AP2 with 3 times higher lattice density, 30 additional quadrupoles are required. Figure 28 was calculated for the examples of 4Q24 quads (pole distance 10 cm, effective length 67 cm), which had been used for BNL $g-2$ beam line. In the current configuration they would be operated with a moderate pole tip field of $\sim$2.5 kG.

F. Debuncher to Muon Ring

The large aperture and strong focusing of the Debuncher is ideal for collection and transport of the pion/muon beam. However, the AP3 line—used today as an antiproton transport line from the Accumulator ring to the Main Injector—has much weaker focusing and hence its admittance is much less than that of the Debuncher. While a further optimization of this beam transport system is forthcoming, for the recent costing exercise the approach taken has been to lay out an AP3 line optics to have the same admittance as the Debuncher ring. This will likely lead to more magnetic elements than necessary for transporting pions/muons from the target, so it gives us an upper bound to the design.

Figure 29 shows the optical layout of the AP3 line used for the costing exercise. What is shown is the square root of the amplitude functions, indicating the relative beam size along the entire length of the line, starting in the Debuncher ring and ending at the entrance to the $g-2$ ring. The quad spacing of the Debuncher is continued through the beam line essentially until it joins up with the existing AP3 line. At this point, the quad spacing changes, reflecting the use of larger aperture quadrupoles throughout most of the remainder of the transport line. At the very end of the line, the beam is directed over and upward to the $g-2$ storage ring, and the beam is focused to a waist as it enters the inflector of the ring.

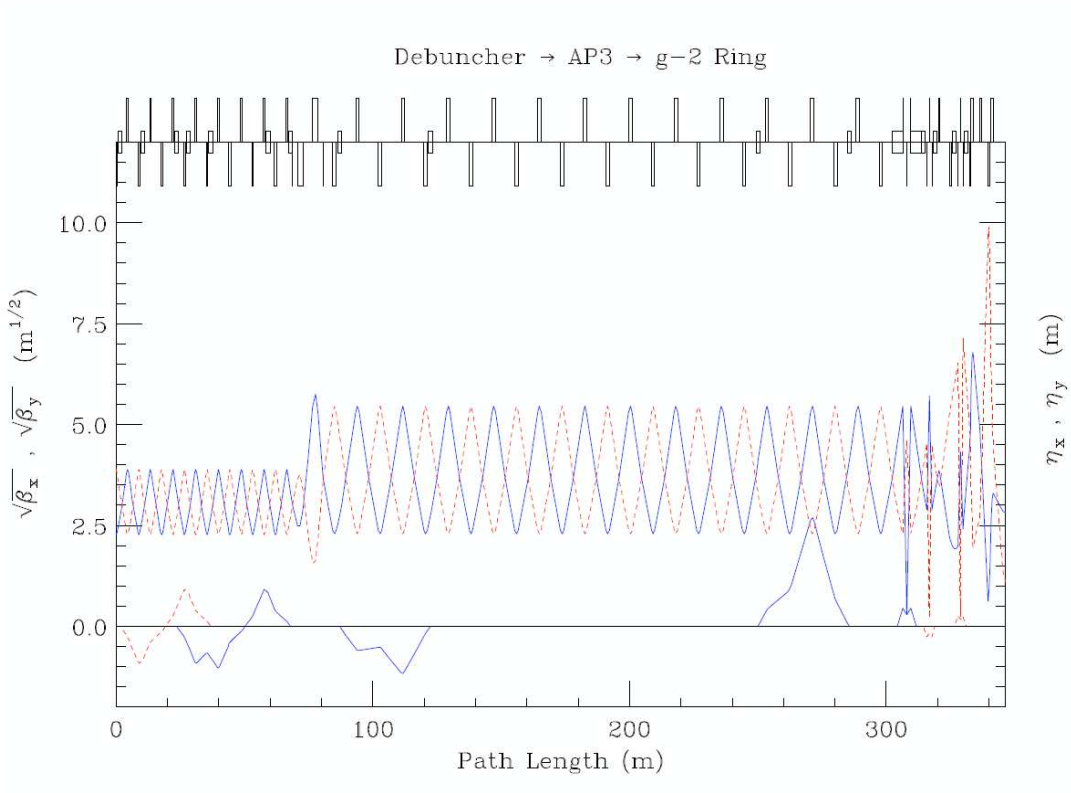

FIG. 29: Layout of AP3 beam line used for costing purposes. The left axis (upper curves) indicates the relative size of the beam envelope and the right axis (lower curves) is the momentum dispersion (orbit spread per $\Delta p/p$).

The geometry of this beam line is consistent with the geometry of the existing Debuncher ring, AP3 line and the newly designed beam line enclosure leading to the ring as described elsewhere.

From this exercise, the total number of quadrupoles is 57, including 14 in the "stub" region (connecting tunnel to the storage ring). The AP3 line already contains 20 quadrupoles, so the number of new quadrupoles required is approximately 23. The dipole magnets to be used either already exist in the present line or are available from Fermilab. In the long run, reductions in the number of elements may be possible, where achromatic bend regions might be extended to allow tolerable dispersion waves, bending magnets could be rolled, focusing requirements could be relaxed slightly, as the design evolves.

1. Availability of quads

An inventory has been made of available magnets at Fermilab or are available from the existing BNL $g-2$ beam line which will be shipped to Fermilab along with storage ring components. Table IX lists the number of magnetic elements in the line for costing purposes.

Quadrupoles	Count Needed	Connected
SQC	14	Series
3Q52	25	Series
3Q84	2	
BNL FF	6	
Others*	11	
Dipoles	17	

TABLE IX: Magnet count for AP3 line costing exercise. *The "other" quads can be combinations of existing, remaining components and are left unspecified for now. The majority of the magnets will be operated in series with each other, minimizing the number of power supplies required

G. Opening the Inflector Ends

The original superconducting inflector design for BNL E821 included two options for the ends: open or closed, see Fig. 30. Both versions were built in 0.5 m long prototype form, but only the closed-end version was built at full scale (1.7 m length) and used in the experiment [107, 108]. The closed inflector was selected because of its simpler construction and was thought to be more stable against Lorentz forces. Further, the closed-end inflector has a smaller fringe field that could be more easily shielded from the storage ring field seen by the muons. On the downside, beam transport studies show that multiple scattering and energy loss in the closed end reduce the transmission of muons that store in the ring by a factor of 2.

The stability of the open-ended coil configuration was demonstrated at full current in a 1.5 T external magnetic field. Based on our measurements [108], the added leakage field

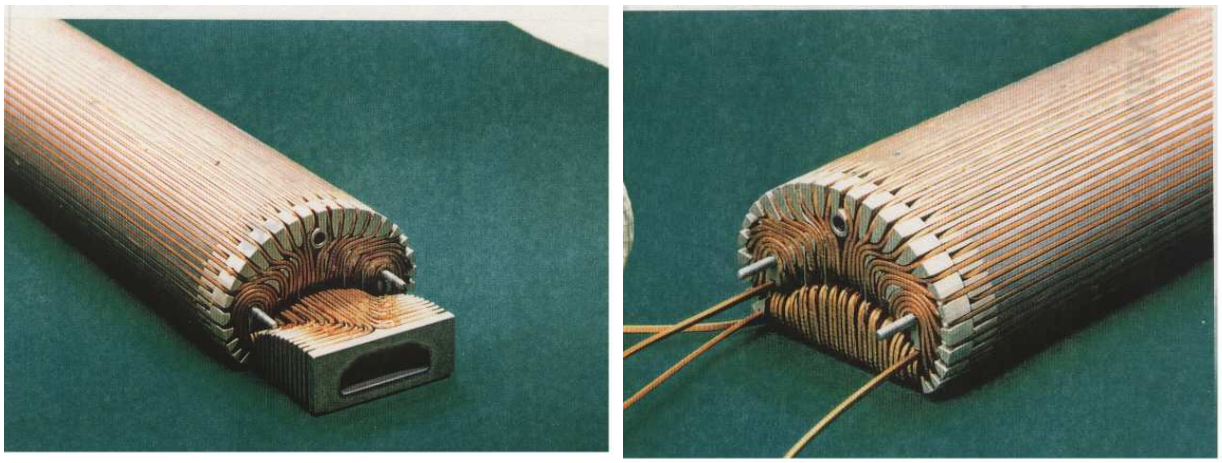

(a)Open End (b)Closed End

FIG. 30: Photos of the open- and closed-end inflector prototype.

from the open end can be excluded from the storage region by a passive superconducting sheet.

A factor of 2 increase in muon flux is expected from opening the ends. Much of the investment in engineering for this device has already been made and custom tooling necessary to construct the magnet exists.

H. Summary of Stored Muon-to-Proton Factors

The experiment at Fermilab requires at least a 6-fold increase of the number of stored muons per 8 GeV proton compared to that obtained by E821 for 24 GeV protons. Table X summarizes the main gain factors of the New $g-2$ Experiment relative to E821 and their origins. These estimates are preliminary and the proposed R&D plan foresees detailed end-to-end simulations—which have begun—as well as beam tests to corroborate these numbers. Additional improvements, due to a faster ring injection kicker or tighter proton focusing on the production target, are under investigation. Thus, the required gain factor of 6 can likely be exceeded, but we conservatively assumed this factor as a planning baseline for this proposal.

parameter	BNL	FNAL	gain factor FNAL/BNL
Y_π pion/p into channel acceptance	$\approx$ 2.7E-5	$\approx$ 1.1E-5	0.4
L decay channel length	88 m	900 m	2
decay angle in lab system	3.8 $\pm$ 0.5 mr	forward	3
$\delta p_\pi/p_\pi$ pion momentum band	$\pm$0.5%	$\pm$2%	1.33
FODO lattice spacing	6.2 m	3.25 m	1.8
inflector	closed end	open end	2
total			11.5

TABLE X: Parameters for E821 and the New $g-2$ Experiment beamline and their relative effect on the stored muons per proton fraction. Pion yield Y_π given for pion momentum bin p_π= 3.11 GeV/c $\pm$ 0.5%.

VI. g−2 CONVENTIONAL FACILITIES

A. Building and Tunnel Connection

Under the direction of Russ Alber, a team of FESS engineers at Fermilab has produced an initial project definition report (PDR) [105]. for the construction of the $g-2$ conventional facilities. These facilities include a new building and a short tunnel connecting the building to the existing AP1 transfer line. The PDR is the result of a concentrated collaboration between project physicists, Brookhaven experts, and FNAL engineers, to design a building and beamline enclosure that will meet the design criteria required by the experiment. Gross features of the building plan include a high-bay experimental area to house the $g-2$ storage ring, a loading dock, and a 30-ton overhead crane; a low-bay service building that contains a control/counting room; a mechanical area for building infrastructure; and a power supply area for beamline and inflector magnet power supplies. Two parking areas are provided, a small paved lot at the west corner of the building near the control room, and a much larger compacted gravel hardstand to the southeast that doubles as a storage area for the $g-2$ cryostats during the ring construction phase. Figure 31 shows an architectural floor plan of $g-2$ conventional facilities.

The site for the experimental hall is located on Kautz road approximately 100' southeast of the AP0 target building. The coarse-scale placement of the building on the FNAL site is dictated by the need to maintain a reasonable distance back to the AP1 tunnel, which will house the final portion of the muon beamline. From the AP1 enclosure, a new three-stepped beam enclosure brings the beam up 18' to the surface over a 50' horizontal run, as shown in Figure 32. The exact position along AP1 has been optimized to minimize disruption of utilities and drainage, and by considering where the muon beam can most conveniently be brought out of the AP1 tunnel and up to the surface. The elevation of the building floor is 4' below the grade of Kautz road, which matches the natural contour of the land (thus minimizing excavation and fill) and has the added benefit of placing the plane of the storage ring slightly below grade (thus reducing radiation concerns). The proximity of Kautz road allows convenient access for trucks to deliver materials to either parking lot or directly to the high-bay via the loading dock. The site also allows convenient access to an electrical feeder for a new 1500 kVA transformer and all other utilities including industrial

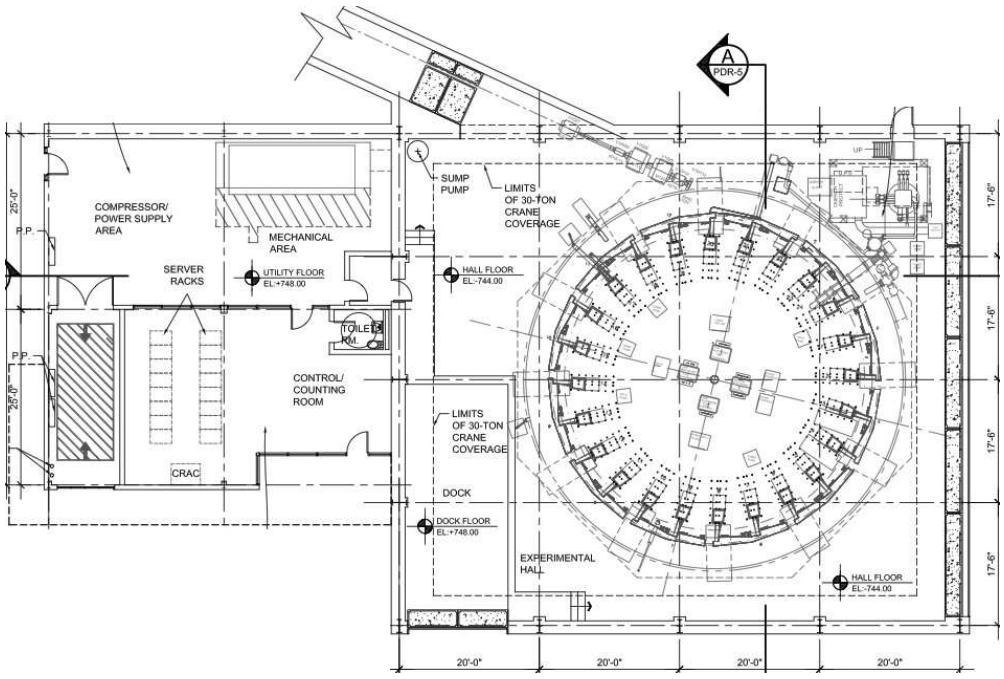

FIG. 31: Architectural floor plan of the $g-2$ conventional facilities.

chilled water. The proximity to the Tevatron enables cryogenic needs to be met with largely existing infrastructure [106].

The high-bay experimental hall has been designed to meet the needs of the muon $g-2$ storage ring in several capacities. The 56' outer diameter of the ring yoke requires a building with a larger clear span than most FNAL buildings. The overall dimensions of the bay are 70' x 80', which is approximately 5' larger in either dimension than the building currently housing the storage ring at Brookhaven. A loading dock in the building provides full access for flatbed trucks to be offloaded directly using a 30-ton bridge crane. The heaviest pieces of material or equipment that need to be moved are the 24 bottom and top plates of the return yoke, each of which weighs 25 tons.

The overall weight of the storage ring is 650 tons. In order to meet the floor stability requirements a novel design has been developed where the storage ring is installed on an octagonal platform that is independent from the rest of the building. The platform is formed from 2.5' thick reinforced concrete and sets on an array of eight 4' diameter caissons down to bedrock. A similar construction method of using caissons down to bedrock is used to support each building pillar. One of the experimental concerns arises from temperature stability in the hall. The C-shaped storage ring can open and close with temperature variations thus

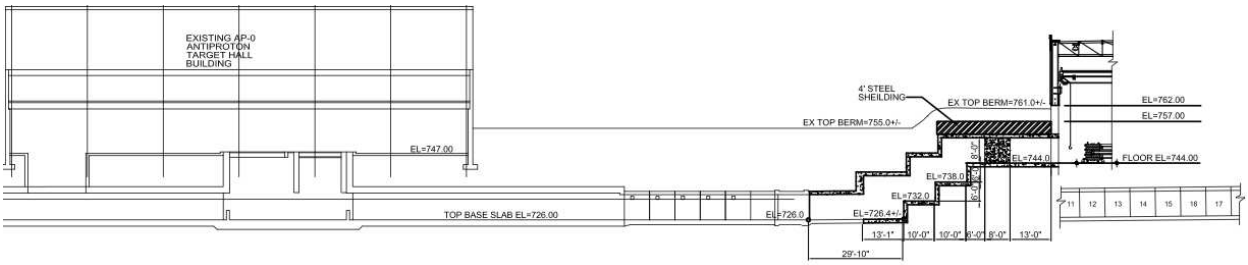

FIG. 32: Elevation view showing the tunnel profile as it bring beam out of the AP1 tunnel and into the high-bay area of the building.

perturbing the field. Even worse, differential heating of one portion of the ring can cause parts of the magnet gap to change relative to others. It was found that with proper building insulation and thermostat settings, a conventional HVAC system can maintain the +/- 2F experimental requirements. A stratification and distribution system has been designed to ensure differential heating of the storage ring is avoided.

As can be seen in Figure 31, the lower half of the building on the opposite side of the control room has a removable shielding wall. This is to accommodate a slot that runs along the entire slide of the building. The slot has been engineered to be free of supports so that it can be open and closed allowing the 14 m diameter superconducting coils to be brought into the building while the ring is under construction. A similar technique was used at BNL where the three coils had to be wound and fabricated one at a time, moved out to the parking area, and the brought back in one at a time as the magnet yoke was assembled.

The low-bay service building attached to the high-bay serves two purposes. It provides a temporary working area outside of the high-bay area during the construction phase of the experiment, as well as meeting the needs of the experiment during operation. The building is divided into two major areas. A mechanical area on the back towards the beamline provides the space needed for building infrastructure including fire protection and HVAC. The same area houses the powers supplies for the superconducting inflector and beamline elements required to bring the muon beam to the surface and produce the final focus into the storage ring. The front half of the low-bay building includes a restroom, control room, and counting house for the detector electronics, data acquisition, NMR readout, surface coil power supplies, and magnet controls. For now shifts are expected to be staffed in the low-bay surface building.

FIG. 33: Rendering showing how the new building located off of Kautz Road would appear. The concrete building to the left is the AP0 target hall where anti-protons for the Tevatron are currently produced, and would also be reused to produce the beam needed for $g-2$.

The beam enclosure brings the muon beam from the AP1 beamline up to the muon $g-2$ surface building in a series of three 6' steps. The costing contains all elements of the civil construction, but beamline elements are included elsewhere in the proposal. Since the AP1 tunnel will still be used to transport 8 GeV protons to the AP0 target, it is necessary to maintain 21' dirt-equivalent radiation shielding along any line of sight. In order to maintain these shielding needs, the top of the last step in the enclosure is capped by a 4' slab of steel. The current berm above AP1 will be extended horizontally to meet the raised 2' thick concrete wall that forms the back side of the muon $g-2$ building.

While the building has been designed to specifically meet the needs of $g-2$, it can more generally be viewed as a valuable asset to the laboratory going into the future. The 70' x 80' clear span of the building is larger than the typical high-bay area available now at the laboratory. The 30 ton crane and reinforced floor will allow for heavy assembly projects in the future. The internal loading dock and engineered slot make the building very accessible. Finally, the connection to the AP1 line and interlocked high-bay can provide an area for other experiments or test stands that require 8-GeV protons or a lower energy, momentum-selected muon beam. One immediate possibility after $g-2$ would be to use the facility for a

dedicated muon EDM experiment or a muon cooling test facility. The rendering in Figure 33 shows the building facade and the proximity to the AP0 target hall, where antiprotons are currently produced.

B. Environmental Assessment

As noted previously, the average particle delivery rate to the $g-2$ target would be 18 Tp/sec. At 8 GeV kinetic energy per proton, this translates to approximately 25 kW beam power onto the target station. Present day antiproton production operation utilizes two Booster batches of 4 Tp every 2.2 sec at a particle energy of 120 GeV, which corresponds to approximately 67 kW beam power onto target. Thus, the activation of the target hall and beam lines leading up to it is expected to be well below present day levels. This should also be expected of the beam delivery from the target into and out of the rings and back to the AP0 region through the existing beam lines since this will be performed as a single-pass beam transport using DC magnetic elements. The final layout of the connecting region between the AP3 beam line and a new $g-2$ experimental hall will need to be assessed for appropriate shielding. While further work will be needed to validate the environmental impact of the new use of these facilities for $g-2$ as well as for the experimental building itself, this is seen as a straightforward effort.

VII. MUON STORAGE RING AND MAGNETIC FIELD MEASUREMENTS

A. Muon Storage Ring Magnet

The muon storage ring [109] is a superferric "C"-shaped magnet, 7.112 m in central orbit radius, and open on the inside to permit the decay electrons to curl inward to the detectors (Fig. 34). A 5 V power supply drives a 5177 A current in the three NbTi/Cu superconducting coils. Feedback to the power supply from the NMR field measurements maintains the field stability to several ppm. The field is designed to be vertical and uniform at a central value of 1.4513 T. High-quality steel, having a maximum of 0.08 percent carbon, is used in the yoke. Low-carbon steel is used for the poles primarily because the fabrication process of continuous cast steel greatly minimizes impurities such as inclusions of ferritic or other extraneous material and air bubbles. An air gap between the yoke and the higher quality pole pieces decouples the field in the storage region from non-uniformities in the yoke. Steel wedge shims are placed in the air gap. Eighty low-current surface correction coils go around the ring on the pole piece faces for active trimming of the field. The opening between the pole faces is 180 mm and the storage region is 90 mm in diameter. A vertical cross section of the storage ring illustrating some of these key features is shown in Fig. 35. Selected storage ring parameters are listed in Table XI.

Attaining high field uniformity requires a series of passive shimming adjustments, starting far from and then proceeding towards the storage region. First the twelve upper- and lower-yoke adjustment plates are shimmed by placing precision spacers between them and the yoke steel, modifying the air gap. Next the 1000 wedge shims in the yoke pole-piece air gap are adjusted. With a wedge angle of 50 mrad, adjusting the wedge position radially by 1 mm changes the thickness of iron at the center of the storage aperture by 50 μm. The wedge angle is set to compensate the quadrupole component, and radial adjustments of the wedge and other changes to the air gap are used to shim the local dipole field. The local sextupole field is minimized by changing the thickness of the 144 edge shims, which sit on the inner and outer radial edges of the pole faces. Higher moments, largely uniform around the ring, are reduced by adjusting the 240 surface-correction coils, which run azimuthally for 360 degrees along the surface of the pole faces. They are controlled through 16 programmable current elements. With adjustments made, the azimuthally averaged magnetic field in the

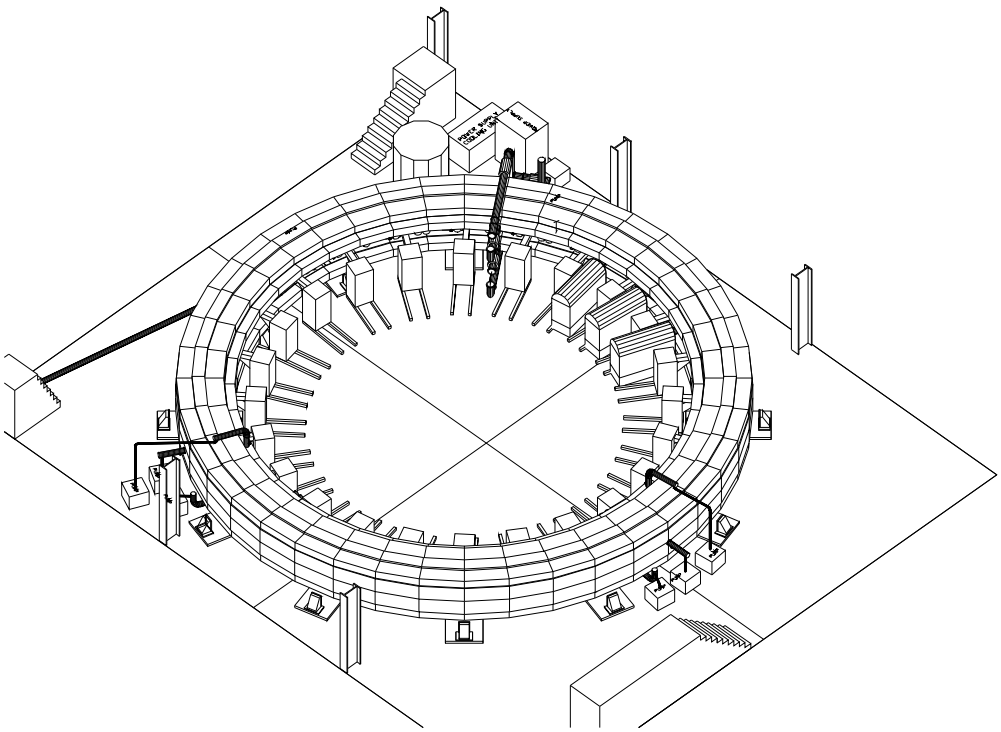

FIG. 34: A 3D engineering rendition of the E821 muon storage ring. Muons enter the back of the storage ring through a field-free channel at approximately 10 o'clock in the figure. The three kicker modulators at approximately 2 o'clock provide the short current pulse, which gives the muon bunch a transverse 10 mrad kick. The regularly spaced boxes on rails represent the electron detector systems.

storage volume had a uniformity of $\simeq 1$ ppm during data-taking runs.

The main temporal variation in the magnetic field uniformity is associated with radial field changes from seasonal and diurnal drift in the iron temperature. Because of the "C" magnet geometry, increasing (or decreasing) the outside yoke temperature can tilt the pole faces together (or apart), creating a radial gradient. The yoke steel was insulated prior to the R98 run with 150 mm of fiberglass to reduce the magnetic-field variation with external temperature changes to a negligible level.

B. Relocating the Storage Ring to Fermilab

Moving the experiment to Fermilab entails the disassembly and shipping of the storage ring along with all of its various subsystems. The subsystems can be disassembled

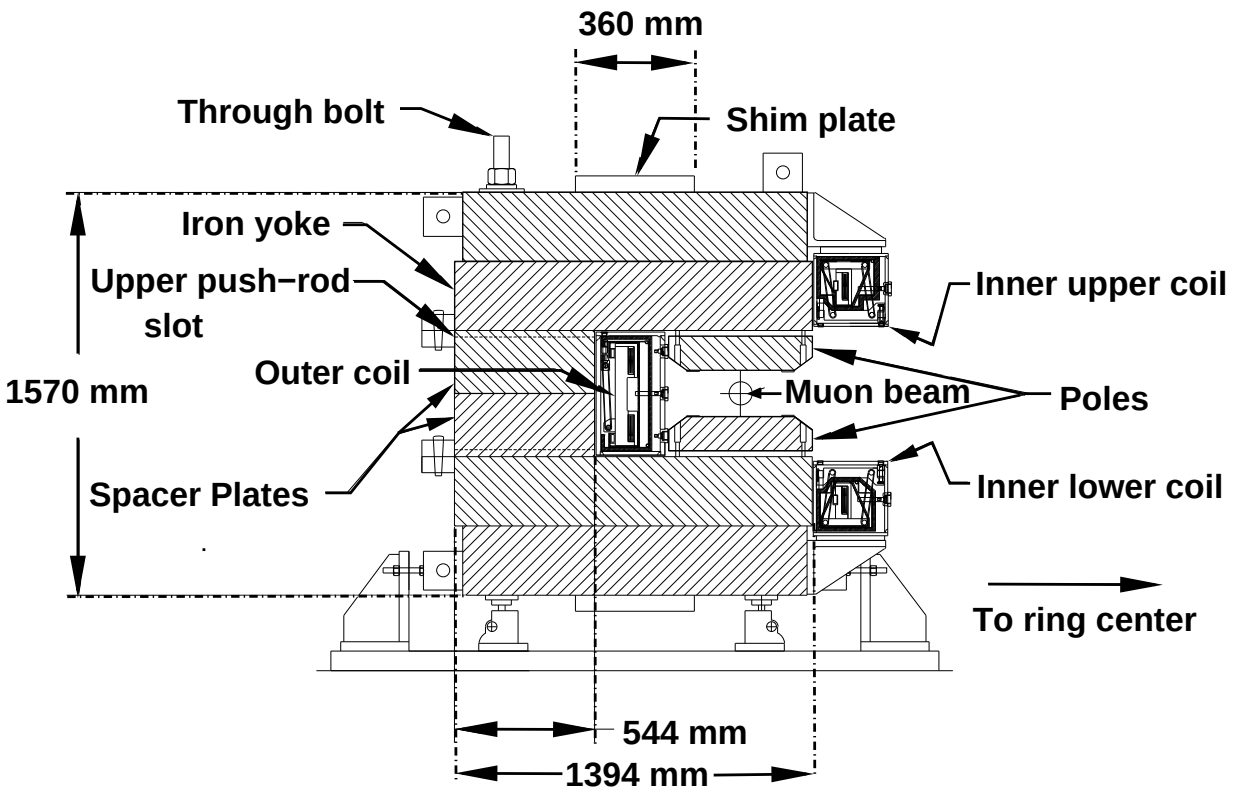

FIG. 35: Cross sectional view of the "C" magnet.

TABLE XI: Selected muon storage ring parameters.

Parameter	Value
Nominal magnetic field	1.4513 T
Nominal current	5200 A
Equilibrium orbit radius	7.112 m
Muon storage region diameter	90 mm
Magnet gap	180 mm
Stored energy	6 MJ

and shipped conventionally, including power supplies and control systems, cryo elements and quench protection, vacuum chambers and pumping stations, electrostatic quadrupoles, shimming devices and NMR systems, and magnetic kickers. The steel plates that form the yoke, see Fig. 35, are constructed in 12 sectors each covering 30 degrees in azimuth. The

plates can be unbolted and transported with a total shipping weight of 680 metric tons.

The main complication in moving the storage ring involves transporting the cryostats that contain the superconducting coils. The three cryostats, shown in cross-section in Fig. 35, are monolithic rings approximately 14 m in diameter. The outer cryostat holds a 48-turn coil separated into two blocks of 24 turns to allow the muons to enter through the space between. Two inner cryostats hold 24-turn coils connected in series to the outer coil with the current flow reversed. Given the large diameter of the coils, shipping overland is not possible. Moving the coils requires airlifting them from Brookhaven to a barge off the Long Island Sound, shipping them through the St. Lawrence Seaway, and into the Great Lakes. From Lake Michigan, the barge can travel via the Calumet SAG channel to a point near Lemont, IL that minimizes the distance to Fermilab. From there, the coils can be airlifted a second time to the laboratory. The total shipping cost for the water transport is estimated at $700K.

One advantage of the proposed route, is the proximity of major expressways between the barge and the laboratories. On Long Island, the William Floyd Parkway, and in Illinois, I-355 to I-88, provide flight paths that avoid air space over residential or commercial areas. Erickson Air-Crane has been contacted for an initial cost estimate and consultation on feasibility. The company is an international specialist in heavy-lift applications, and their S-64 aircrane has a 25,000 lb load capacity, which is enough to transfer the heaviest of the coils along with its lifting rig. The cost for the entire air crane operation at both ends of the barge voyage was quoted at $380K.

C. The Precision Magnetic Field

We propose to measure the magnetic field in the present experiment to a precision of about 0.07 ppm using essentially the same technique and apparatus which was used in E821. The technique was developed, implemented, and refined over a period of about twenty years. [110–115]. An uncertainty of 0.17 ppm had been reached when experiment E821 was stopped (cf. table XII).

A brief overview of the measurement is given in section VII D. Section VII E outlines the improvements that were made in the course of E821 and which resulted in the gradual reduction of the uncertainty in the field measurement by a factor of three. In section VII F

we discuss the shimming procedure necessary to regain the field homogeneity after moving the magnet. In section VII G we outline our plans for reestablishing the measurement after several years without operation, and how we foresee a further improvement in uncertainty to the projected 0.07 ppm.

D. Methods and Techniques

The measurement of the magnetic field in experiment E821 is based on proton NMR in water. A field trolley with 17 NMR probes was moved typically 2–3 times per week throughout the entire muon storage region, thus measuring the field in $17 \times 6 \cdot 10^3$ locations along the azimuth. The trolley probes were calibrated *in situ* in dedicated measurements taken before, during, and after the muon data collection periods. In these calibration measurements, the field homogeneity at specific calibration locations in the storage region was optimized. The field was then measured with the NMR probes mounted in the trolley shell, as well as with a single probe plunged into the storage vacuum and positioned to measure the field values in the corresponding locations.

Drifts of the field during the calibration measurements were determined by re-measuring the field with the trolley after the measurements with the plunging probe were completed, and in addition by interpolation of the readings from nearby NMR probes in the outer top and bottom walls of the vacuum chamber. The difference of the trolley and plunging probe readings forms an inter-calibration of the trolley probes with respect to the plunging probe, and hence with respect to each other.

The plunging probe, as well as a subset of the trolley probes, were calibrated with respect to a standard probe [119] with a 1 cm diameter spherical H_2O sample in a similar sequence of measurements in the storage region, which was opened to air for that purpose. The standard probe is the same as the one used in the muonium measurements that determine the ratio λ of muon to proton magnetic moments [13].

The NMR clock and the clock that measured the muon spin precession period were phase-locked to the same LORAN-C [120] signal. Systematic effects include the instrument response and were extensively studied. The leading uncertainties in the calibration procedure resulted from the residual inhomogeneity of the field at the calibration locations, and from position uncertainties in the active volumes of the NMR probes.

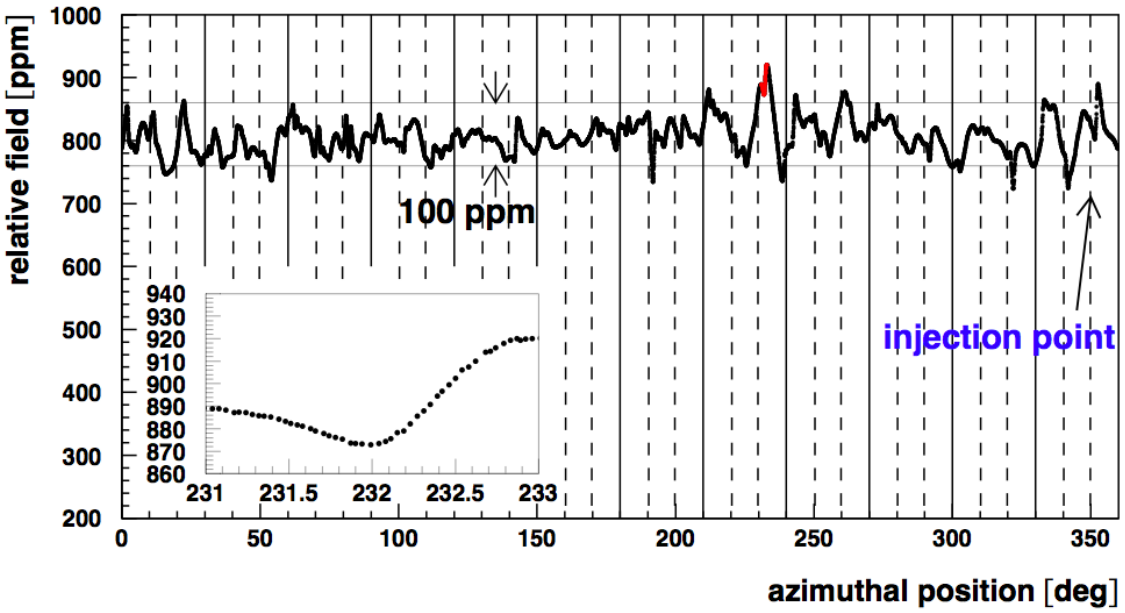

FIG. 36: The NMR frequency measured with the center trolley probe relative to a 61.74 MHz reference versus the azimuthal position in the storage ring. These data come from one of the 22 measurements taken with the field trolley during the 2001 data collection period. The solid vertical lines mark the boundaries of the 12 yoke pieces of the storage ring. The dashed vertical lines indicate the boundaries of the pole pieces.

The ring magnet design [116], the inflector design [117], and extensive shimming contributed to the overall uniformity of the field throughout the storage ring. Figure 36 shows one of the magnetic field measurements with the center NMR probe in the trolley for E821's final data collection period in the year 2001. A uniformity of ± 100 ppm in the center of the storage region was achieved for both field polarities and for the full azimuthal range, in particular also in the region where the inflector magnet is located.

Figure 37 shows a two-dimensional multipole expansion of the azimuthal average of the field in the muon storage region from a typical trolley measurement in 2001. Since the average field is uniform to within 1.5 ppm over the storage aperture, the field integral encountered by the (analyzed) muons is rather insensitive to the profile and the precise location of the beam, which was determined to within a millimeter in both coordinates.

The measurements with the field trolley were used to relate the readings of about 150 (out of 370) NMR fixed probes in the outer top and bottom walls of the storage vacuum

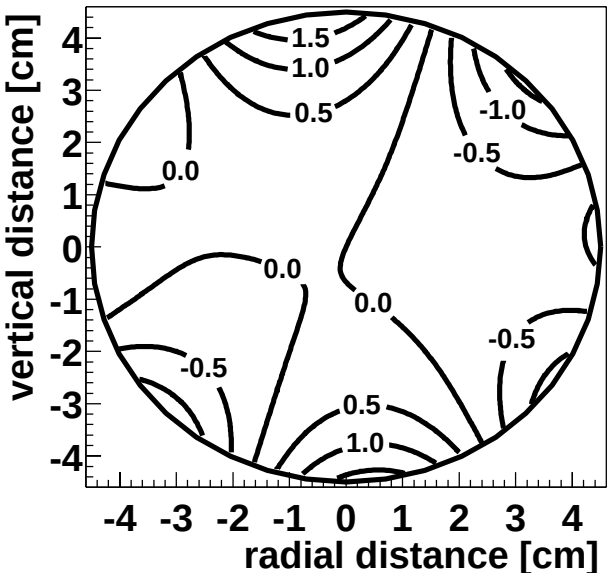

FIG. 37: A 2-dimensional multipole expansion of the azimuthal average of the field measured with trolley probes with respect to the central field value of about 1.45 T. The multipole amplitudes are given at the aperture of the 4.5 cm radius storage aperture.

chamber to the field values in the beam region. The fixed NMR probes were read out continually. Their readings were used to interpolate the field during data collection periods, when the field trolley was parked in a garage inside of the vacuum chamber. The garage is located just outside the beam region. The uncertainty in this interpolation was estimated from redundant measurements with the field trolley within the same magnet-on period.

The field change induced by eddy currents from the pulsed kickers was measured for a prototype chamber with an optical magnetometer [118]. Time-varying stray fields from the accelerator were measured *in situ* with the NMR system [111, 112] and found to contribute negligible uncertainty. Another small uncertainty comes from the off-vertical field components [122].

The total field uncertainty is predominantly systematic, with the largest contribution coming from the calibration. For all data collection periods, the results and uncertainties were based on two largely independent analyses.

E. Past Improvements

The uncertainty in the field measurement was improved by a factor of three in the course of experiment E821 and reached a final value of 0.17 ppm for the year 2001 (cf. Table XII).

The superconducting inflector magnet [117] was replaced between the data collection periods in 1999 and 2000 because of a damaged superconducting shield which permitted stray magnetic flux to leak into the storage region. This replacement minimized the inflector fringe field in the storage region in subsequent data collection periods and eliminated the need to measure the magnetic field with separate trolley settings in the inflector region. Together with refined shimming with programmable current loops, it improved the field homogeneity and thus reduced the uncertainty associated with our knowledge of the muon distribution that existed for our 1998 and 1999 results.

The addition of a plexiglass port and mirror setup to the storage ring before the 2000 data collection started, allowed us to precisely position the trolley shell at the location of a plunging probe without breaking the vacuum. It thus allowed us to make a relative calibration of the trolley probes with respect to the plunging probe during the data collection periods in 2000 and 2001, in addition to the calibrations made before and after each period.

Improvements in the alignment of the trolley rails throughout the storage ring and improvements in the trolley drive mechanism allowed us to measure the field with the trolley more often during the 2000 and 2001 data collection periods. Furthermore, we upgraded the readout of the trolley position in the storage ring before the data collection period in 2001 to reduce the uncertainty in the measurement of the average central field with the trolley.

Additional study of the trolley frequency, temperature, and voltage response resulted reduced uncertainties for the 2000 and 2001 results.

F. Shimming the Storage Ring Magnetic Field

The success of the experiment requires that the magnetic field be shimmed to a uniformity of ≈ 1 ppm averaged over the storage volume. This was essentially achieved by BNL E821. A more stringent requirement of the new experiment is that the field be measured to a precision of less than about 0.1 ppm. Improvements in field uniformity over those achieved in E821 will help to reach this more challenging goal.

TABLE XII: Systematic uncertainties in the measurement of the magnetic field for experiment E821 (1998–2001) and our projections for a future effort based on known techniques and existing equipment. The uncertainty "Others" groups uncertainties caused by higher multipoles, the trolley frequency, temperature, and voltage response, eddy currents from the kickers, and time-varying stray fields.

Source of errors	Size [ppm]				
	1998	1999	2000	2001	future
Absolute calibration of standard probe	0.05	0.05	0.05	0.05	0.05
Calibration of trolley probe	0.3	0.20	0.15	0.09	0.06
Trolley measurements of B_0	0.1	0.10	0.10	0.05	0.02
Interpolation with fixed probes	0.3	0.15	0.10	0.07	0.06
Inflector fringe field	0.2	0.20	-	-	-
Uncertainty from muon distribution	0.1	0.12	0.03	0.03	0.02
Others		0.15	0.10	0.10	0.05
Total systematic error on ω_p	0.5	0.4	0.24	0.17	0.11

The magnet was assembled as a kit at BNL, and would be assembled in a similar fashion at FNAL. The magnet is made of 12 C-shaped iron yoke sectors, each in turn composed of precision engineered, low carbon steel plates. Variations in the yoke plate thicknesses of the order of 200 μm, cause similar variations in the 20 cm air gap, leading to variations in the dipole field of 1000 ppm around the storage ring. Changes in the yoke permeability from sector to sector also lead to changes in the dipole field, as do tilts, gaps, and other imperfections.

Practical mechanical tolerances thus inevitably lead to variations of the magnetic field of a thousand ppm. It is therefore unavoidable that reassembling the storage ring at Fermilab will lead to the loss of field homogeneity realized at Brookhaven.

Reattaining high field uniformity requires a series of shimming steps, well established by E821, from coarse to fine adjustments, and from mechanical to electrical techniques.

First the 12 upper and lower-yoke adjustment plates are shimmed by placing precision spacers between them and the yoke steel, modifying the air gap. The precision pole pieces are adjusted so that the surfaces of adjacent pole pieces are matched to $\pm$ 10 μm. The

angles of the poles are measured to ± 50μrad, and adjusted so the pole faces are horizontal when the magnet is powered.

Next, the precision pole pieces are attached to each yoke sector, separated by a 1 cm air gap. In the air gap are inserted a total of 864 adjustable iron wedges. The wedges were machined with an angle of 50 mrad to compensate for the normal quadrupole moment expected from the C-magnet design. Moving a single wedge radially by ±3 mm changes the air gap by ±150 μm, changing the dipole field locally by ±300 ppm (with higher order moments essentially unchanged). Finer movements allow correspondingly finer adjustments of the dipole field.

The air gap also contains dipole corrections coils (DCCs) which allows the dipole field over a pole to be adjusted by ± 200 ppm. The currents in these 72 DCCs were static in E821, but active feedback is possible.

With these tools, the variation of the dipole field around the ring can be reduced to acceptable levels.

Higher order moments of the field are reduced by shimming elements placed between the pole faces and the storage volume. These include 5 cm wide iron shims placed on the inner and outer radius of each pole. The edge shim thicknesses are adjusted to minimize the normal sextupole, and skew quadrupole and sextupole. It would be prudent to produce new edge shims, though it is possible none would be required.

Another tool for reducing higher order moments are the surface correction coils (SCCs). These are a set of 2 × 120 coils, 360° in azimuth on PCBs, 2.5 mm apart, carrying ± 1A. The currents through the coils are set individually to reduce the average of the normal quadrupole and other moments over the ring. With these tools, a uniformity of ≈1 ppm should be achievable.

It is important to mention that maintaining this homogeneity requires that the magnet be insulated from changes in the environment. Temperature changes affect the yoke spacing, and temperature gradients in the yoke can produce quadrupole moments in the field. Insulating the magnet from temperature changes and gradients is an important part of preparing the field for the experiment.

A special shimming trolley with NMR probes will be used during the shimming process. During initial shimming the vacuum chambers will be absent. Field mapping at about 10^5 points (approximately 2 cm apart) will be done to obtain a complete map with the trolley

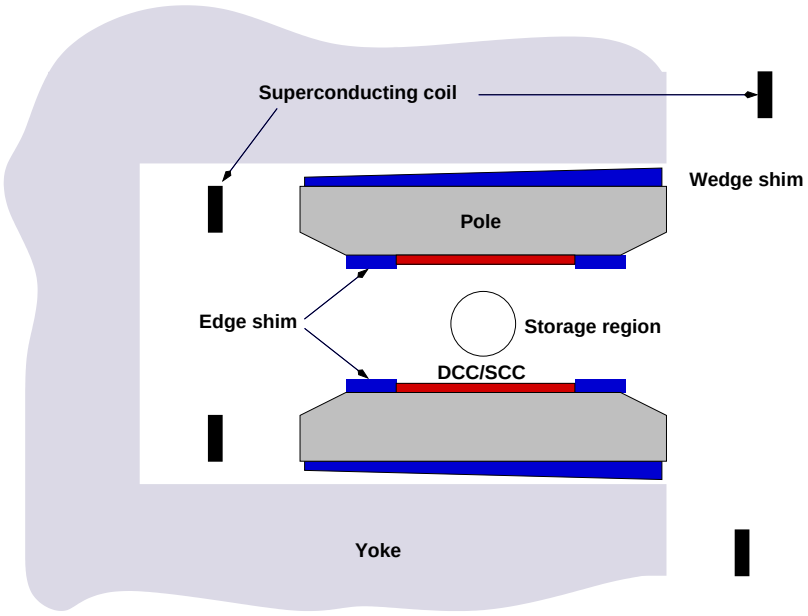

FIG. 38: Schematic view of the magnet pole region, showing the location of the various shims.

in a period of 4 to 8 hours. A measured set of field points can always be represented for a 2-dimensional case and the harmonic description is useful for shimming and also for analysis of errors due to field inhomogeneities. Three dimensional problems will be dealt with empirically. A computer program will provide rapid off-line analysis to represent the field in its harmonic components and with this information a decision can be made about what changes to make in the shimming configuration. It will be necessary to turn the storage ring magnetic field off to make changes in the iron shims.

The shimming techniques will all be done with an iterative approach involving field measurement, calculation, shimming and remeasurement. The calculation to predict the shimming required to improve the field will depend on the particular shimming technique being employed and on the character of the inhomogeneity.

We can anticipate at least 6 months or more will be required (once the magnet has been reassembled and powered) to shim the magnet without the vacuum chambers in place. This time would be used to adjust the pole face positions and tilts, to adjust the wedges and DCCs, make fine adjustments with the thin iron shims, and to make any changes to the edge shims. Note that some sort of mechanism for moving the shimming trolley around the ring will be necessary, as well as a means of determining its azimuthal position.

G. Further Improvements

The methods and techniques used in E821 are not fully exhausted; to reach a precision of 0.11 ppm, as detailed in Table XII, only modest refinements are necessary. To reach the projected 0.07 ppm, no single approach suffices, and several systematic error sources need to be addressed simultaneously.

Our efforts to improve the existing apparatus and techniques would be focussed on the following items.

- *in situ* measurement of the field change from kicker eddy currents [118].
- Extensive measurements with the magnetic field trolley, aiming in particular to better resolve the position of the active NMR volumes inside the trolley shell and to map out the response functions to the level where *corrections* can be applied, rather than *limits* be set.
- More frequent measurements of the magnetic field in the storage ring during beam periods (following mechanical maintenance on the trolley drive and garage).
- Repair and retuning of a number of the fixed NMR probes to improve the sampling of the storage ring.
- Replacement of the power supplies for the surface correction coils to eliminate the occasional data loss caused by oscillating outputs.
- Refinement of the analysis techniques to reduce trolley position uncertainties in the storage ring.
- Temperature control of the environment of the storage ring magnet.
- Additional shimming of the storage ring once the homogeneity of the E821 field has been reestablished at FNAL.
- Use thin (25-100μm) iron shims on the pole faces to further reduce azimuthal variations in the dipole field, which primarily couples to uncertainty in trolley position.
- Replacement of outdated computing and readout infrastructure.

- Replacement of the LORAN-C time reference by GPS-based system, if necessary.

Better knowledge of the muon beam distribution, required by the anomalous precession measurement, would also benefit the measurement of the average magnetic field.

Further improvements down to the final goal of 0.07 ppm require significant R&D. Several aspects of the measurement need to be addressed simultaneously, as no single improvement suffices to reach this level of precision. Development of new experimental techniques and equipment include

- Replacement of the water-based absolute calibration probe by a ^3He based system;
- Re-positioning of the fixed probes;
- Upgrade of the NMR trolley drive system;
- Upgrade of the plunging probe drive; and
- Re-machining of the precision poles.

Continued development of an independent helium-3 based standard probe [123], would benefit the field measurement, however, the projected uncertainty of 0.07 ppm does *not* rely on it.

In E821 about half of the fixed probes could not be used effectively, due to their proximity to the joints in the precision pole pieces and yoke and the resulting field inhomogeneity. For those used, an empirical importance (weight factor) was assigned, depending on its location. By increasing the usable number and effectiveness of the fixed probes, the field tracking uncertainty in-between trolley runs can be further improved. An extensive simulation program, including a detailed field description that includes the effect of the magnet imperfections and the specifics of the fixed probes, will be needed to find optimal positions. Modification of the vacuum chambers will have to be taken into account.

Tracking of higher multipoles, and thus the interpolation uncertainty, would greatly benefit from the placement of probes in the midplane of the storage volume, rather than just above and below it. Because of the geometry of the vacuum chambers this would imply placement *in vacuo* and as close as possible to the horizontal quadrupole plates. At the inner radius of the ring, these probes could interfere with the placement of the calorimeters

and other equipment. A probe that can operate in this environment, including a mounting and cabling scheme, has to be developed and the vacuum chambers will have to be adapted.

An increase of the speed with which the trolley moves though the ring would allow for more (frequent) measurements in the storage volume. It would simultaneously address the reduction of several sources of uncertainty, such as the trolley temperature and field interpolation. It requires the redesign of the trolley drive, together with an improvement in the alignment of the trolley rails. Besides an increase in trolley speed, the latter will also lead to a reduction of the trolley position uncertainty, which coupled to the azimuthal field inhomogeneity affects the uncertainty in the averaged field B_0.

The relative calibration of the trolley probes can be improved by operating the plunging probe more frequently, perhaps even *during* each trolley run. This would require the development of a faster, more powerful plunging probe drive, which has to operate close the precision field, without affecting it at a significant level.

Finally, with the advent of more powerful magnet design tools and computer-aided machining tools, it should be investigated whether the precision poles should be re-shaped to eliminate the need and limitations of the edge shims.

The successful completion of these improvements are expected to suffice to reach the projected goal 0.07 ppm, together with the refinements mentioned before. We do note, however, that the improvement relies significantly on measurement of the field change from kicker eddy currents and the absence of field perturbations caused by the redesigned (open) inflector magnet. Neither of these have been demonstrated to a sufficient level at this time.

We are confident that a field knowledge to a precision of 0.11 ppm can be reached using the *existing* experience in the field group. The present hardware has the potential to reach that level with the moderate aforementioned repairs and upgrades. A further reduction down to 0.07 ppm appears reachable with the successful completion of a multi-facetted R&D program aimed at reducing several systematic uncertainties simultaneously.

VIII. ω_A MEASUREMENT

A. Overview

The measurement of ω_a is made by recording the arrival times and energies of decay positrons in a suite of 24 electromagnetic calorimeters. A position-sensitive scintillator hodoscope is placed upstream of each calorimeter to record impact positions and to provide horizontal and vertical distributions, which are important for stored beam diagnostics. Coincident events, which penetrate two or three adjacent calorimeter stations, serve as "lost muon" detectors. In several stations, a suite of straw chambers, placed upstream of the calorimeters and inside the vacuum chambers, provide detailed beam dynamic information and serve as the basis for a parasitic electric dipole moment measurement. This chapter describes the systems we will use for the ω_a measurement, which are largely based on the experience obtained in E821.

For planning purposes, we assume that the expected rates in the new experiment will slightly exceed those of E821. The empirical argument to gauge the increase follows. The total E821 statistics of 8.5×10^9 events was accumulated in 2.5×10^7 storage ring fills. Allowing for efficiency factors consistent with those described in Table VII, E821 ran for 0.8×10^7 seconds using $\approx 1.5 \times 10^{20}$ protons on target (POT). In this summary of E821, commissioning time is excluded. At Fermilab, the storage ring fill frequency will be greater by a factor of 4 and the requested data-taking period is longer by a factor of nearly 4. Thus, the number of storage ring fills in the final sample will be greater by a factor of ~ 15; the 21 times increase in statistics then roughly implies that the experiment will be carried out at a rate ~ 1.5 times higher (we are rounding here). Under planned beam delivery scenarios, it could rise by as much as a factor of 3. Consequently, the detectors, electronics and DAQ, will be designed to accept sustained rates per fill up to 3 times as high as BNL E821. The rate comparison is important because it guides upgraded or new systems. First, the instantaneous rate near fit start time determines the pileup fraction, which is a critical systematic uncertainty. Second, the total data flow determines the details of the electronics and DAQ systems, their data transfer rates and the total data storage required.

Higher data rates lead to the conclusion that segmented electromagnetic calorimeters are required to reduce the pileup fraction per channel. Additionally, the position sensitive

detectors must have higher segmentation. We describe a design below, which satisfies these demands.

New waveform digitizers (WFDs) will be used to continuously digitize the analog signals from the calorimeter segments during each fill period. These data will flow to dedicated pre-frontend processors upstream of the frontend data acquisition modules where they will be packaged into event streams of derived databanks for the so-called T-method and Q-method analyses (see below). The collaboration has experience in building and running WFDs. After E821, we built more than 350 channels of 450-MHz, VME-based WFDs for several precision muon lifetime experiments at the Paul Scherrer Institute (PSI). We also built a precision clock distribution system to accurately drive all the WFDs at a known and stable frequency. The two "lifetime" experiments—MuLan [124] and MuCap [125]—have data rates and precision demands that prepare us for the requirements of a new $(g-2)$ effort. Together, those experiments acquired more than 140 TB of data, which are being processed using the NCSA computers and storage system at the University of Illinois. For the New $g-2$ Experiment, we will have a larger data volume, which can be stored and processed using the Fermilab grid of computers and data storage. Significant computing resources also exist in the collaborating institutions for studies and analysis of the processed data. As in the past, we anticipate multiple independent approaches to the data analysis, following standard "blinding" techniques.

The traditional, or T method, where individual decay-positron "events" are analyzed for time and energy, remains our primary analysis tool. Additionally, we will employ a complementary and elegant "integrating" method, the Q method. The Q method amounts to digitizing the energy deposited in an entire calorimeter (all segments) vs. time following injection. No threshold is necessary; all samples are recorded without bias and summed. The method is robust and intrinsically immune to pileup, but it is new and other systematics will likely emerge.

In the T method, positron decays are recorded individually and are sorted by energy and time. For each positron recorded at time t and having energy greater than E_{th}, a single count is incremented in a histogram, such as the one shown in Fig. 7. The asymmetry is determined by the choice of threshold, and the statistical power is proportional to NA^2. Optimizing this figure-of-merit implies setting E_{th} between 1.8 and 1.9 GeV. The T method is well understood by the collaboration; we use it to determine event rates and running necessary

for the goals of this proposal. A slight variant on the T method is an asymmetry-weighted (or energy-weighted) event mode, a T' method. Here, individual events having energy E_i are weighted by their asymmetry, A_i. This method improves the statistical power of the T method by about 10 percent at a cost of modestly increased demands on the gain stability of the detectors. The T' method can be derived from the standard data set and requires no additional hardware or special data-taking procedures. Variants of this method were used as part of the analysis approaches applied to the 2000 and 2001 data-taking periods in the E821 experiment.

In contrast, the Q method does not rely on the separate identification or isolation of positron events. It involves integrating the energy deposited in the entire calorimeter, plotted as the summed energy vs. time. In this simple method, the energy deposited, which is proportional to the light in the calorimeter, is digitized for the entire fill and the digitized samples are in turn added from fill to fill to produce a final histogram. The histogram can be fit by the same function used to fit the T method data. The asymmetry is lower compared to the T method because all accepted events are used, even the small fraction of low-energy positrons that hit the calorimeter and carry negative asymmetry compared to the higher-energy positrons (See Fig. 6b). The discrete placement of the detectors ensures a higher comparative acceptance of the highest energy positrons, and a net asymmetry approximately half that of the T method. In the Q method, a greater number of events are included, thus the effective N is larger. We have performed a Geant4 simulation to compare the T and Q methods. The simulation is based on tracked muons through the storage ring and features details such as the coherent betatron oscillation, which modulates the detector acceptance. We ignored that small effect in fitting the data; the result is a poor χ^2/dof, but it otherwise does not affect the comparison. Figure 39 shows spectra prepared using the T and Q methods, both fit with the five-parameter function:

$$N \exp\left(-t/\gamma\tau\right)[1 + A\cos\left(\omega t + \phi\right)].$$

In the upper panel, the number of events having positron energy greater than $E_{th} = 1.8$ GeV is plotted vs. time after injection. The fit gives an uncertainty on ω_a of 59 ppm for this sample. The bottom panel shows the same simulation, but the plot represents calorimeter energy vs. time after injection. The uncertainty on ω_a is 65 ppm; the Q method is statistically weaker than the T method by about 9 percent, implying an 18 percent longer run

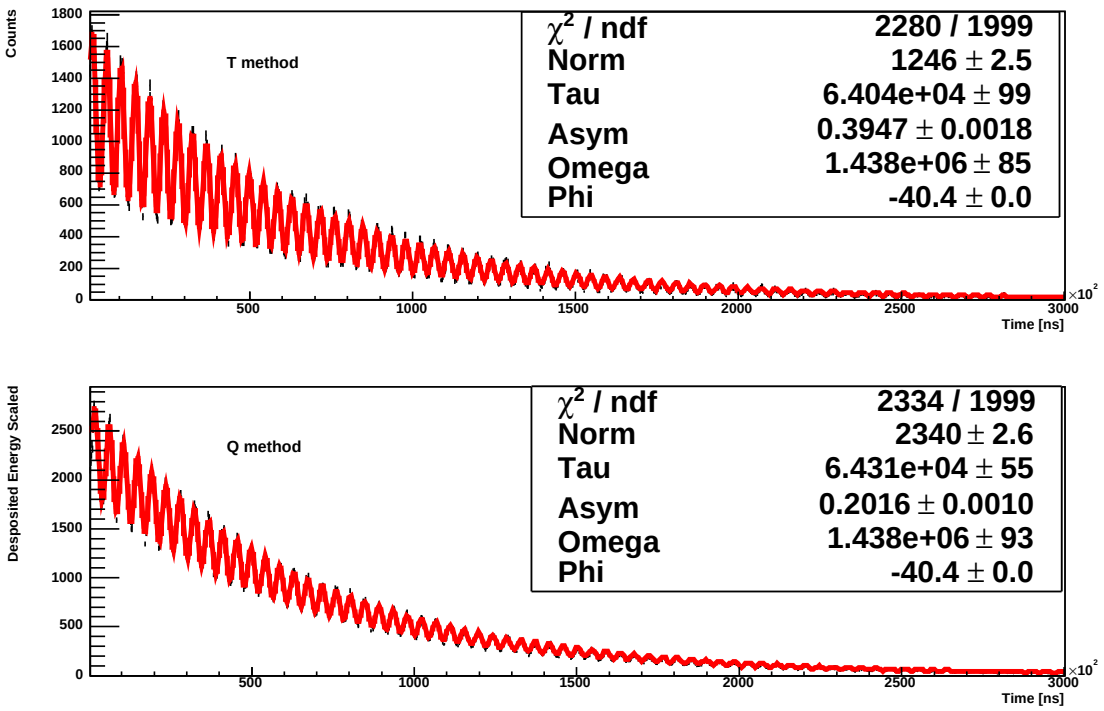

FIG. 39: Geant4 simulation of events. Upper panel: Data analyzed using the tradition T method with $E_{th} = 1.8$ GeV. Lower panel: Data prepared using Q method, representing energy vs. time. Note the poor χ^2/dof for each plot is because the fits were performed using a simple 5-parameter function, which ignores the coherent betatron oscillations present in the simulation.

is necessary to obtain the same precision. However, the Q method has an interesting advantage. There is no pileup correction to be made so the increased rate will not complicate the analysis algorithm. While the Q method had been recognized as viable during the E821 effort, it was impossible to implement with the existing WFD hardware and unattractive to use because of the significant hadronic flash, which added a large and slowly decaying baseline for many of the detectors in the first half of the ring. Our new digitizers will be capable of storing all the samples from a complete fill so Q-method running can be enabled as a parallel data stream; the anticipated smaller hadronic flash should keep the pedestal baseline relatively flat.

B. Electromagnetic Calorimeters

The electromagnetic calorimeters for the E821 experiment used a Pb/SciFi design [126, 127]. Each calorimeter consisted of a monolithic block of 1-mm diameter fibers arranged in a near close-packed geometry within grooved lead alloy foils. The fractional composition of the detector was Pb:Sb:Fiber:Glue = 0.466 : 0.049 : 0.369 : 0.096 (by volume), leading to a radiation length $X_0 = 1.14$ cm. The fibers were oriented radially so that the positrons would impact on the detector at large angles with respect to the fiber axis. Four lightguides directed the light to independent PMTs and the summed analog signal was processed by waveform digitizers. The 14-cm high by 22.5-cm radial by 15-cm deep calorimeter dimensions were largely dictated by the available space and the need to have a sufficient radial extension to intercept the positrons. The energy resolution requirement for $(g-2)$ is relatively modest, $\sim 10\%$ or better at 2 GeV.

For the New $g-2$ Experiment, the systematic errors associated with gain instability (0.12 ppm) and pileup (0.08 ppm) must each be reduced by a factor of $\sim 3-4$. We have designed [14] a new calorimeter that retains the fast response time of plastic scintillating fiber, but is made from an array of dense submodules where each is oriented roughly tangential to the muon orbit. This configuration provides transverse segmentation and allows for multiple simultaneous shower identification. A 50:50 ratio of tungsten to scintillator (and epoxy) reduces shower transverse and longitudinal dimensions. The calculated [129] radiation length, $X_0 = 0.69$ cm, is 60% of the length for the Pb/SciFi modules used in E821. Consequently, the modules can be made compact enough to free space for downstream readout in the highly constricted environment of the storage ring. The high density leads to a smaller radial shower size, which improves the isolation of simultaneous events. We find that using 0.5-mm layers gives an acceptable resolution close to 10% at 2 GeV for a prototype we have built and tested; a non-trivial error contribution to this measured performance parameter came from the beam momentum spread, photo-electron yield and transverse leakage fluctuations in our test environment. Therefore, the intrinsic detector response from sampling fluctuations alone is better.

A plan view of the vacuum chamber and the detector positioning is shown in Fig. 40, indicating that this design looks promising for the standard vacuum chamber sections. In this figure, 20 lightguides are indicated as they curl toward the inside of the storage ring. By

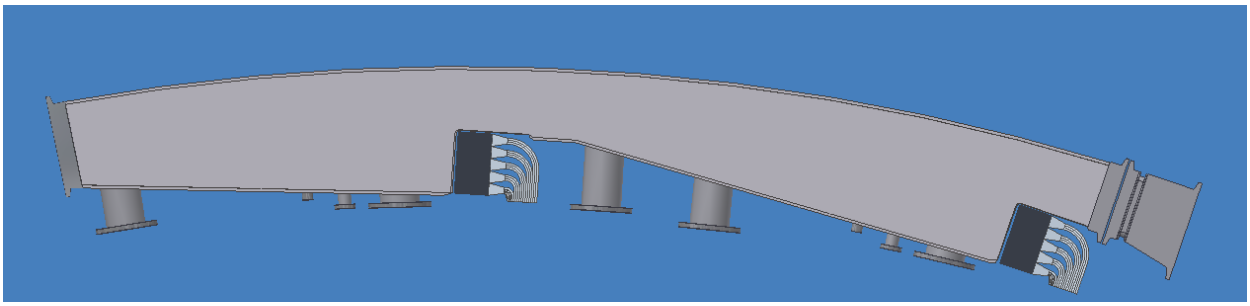

FIG. 40: Plan view of new calorimeters and existing scalloped vacuum chamber region.

design, the W/SciFi is a single monolithic array, which can be readout on the downstream side by any segmentation of optical couplers. The choice of 20 or 35 readouts (4×5 array or 5×7 array) is an optimization to be determined based on the final readout solution. We are exploring silicon photomultiplier (SiPM) arrays and will perform tests in the coming year with newly procured samples. At the time of this proposal, several large SiPM arrays are being produced, which would nicely match the 35-segmented model mentioned above. However, a conservative solution will be to use PMTs located outside of the field region. It is a solution that we have considerable experience in implementing based on E821.

Appendix C includes a more detailed description of a tungsten / scintillating fiber (W-SciFi) sampling calorimeter that meets these demands. In anticipation of this proposal, we built a 4×6 cm^2 prototype module made of 0.5-mm pitch layers of fiber ribbons and pure tungsten plates. Measurements were made at PSI and at Fermilab and results have been reported [14]. We have also recently completed a 15×15 cm^2 prototype in near-final geometry and are instrumenting it for a test-beam run in May of 2010.

C. Position-Sensitive Detectors

In E821, five-fold, vertically segmented scintillator hodoscopes were mounted on the upstream side of each calorimeter. To provide impact position information for shower reconstruction and to obtain a better horizontal and vertical profile, we propose to use a system of straw detectors in front of each station. These can be relatively simple detector systems with standard multi-hit TDC digitized readout. The time-start for the straws will be derived from a summed signal from the calorimeters. The straw system in front of each calorimeter will provide information for shower impact, pileup identification, and muon loss monitor-

ing. For some stations, a complement of in-vacuum straws will serve as positron traceback detectors, which are needed for beam dynamics imaging. These extended imaging stations will also provide the data used in the physics analysis for a muon electric dipole moment (See Section IX).

D. Waveform Digitizers for Calorimeter Readout

The primary data acquisition challenge for a new experiment is the readout and interpretation of the calorimeter signals. For the New $g-2$ Experiment, we intend to gather this information via waveform digitization, where the PMT analog output waveforms are continuously digitized at high speed. While waveform digitization was used to great effect in E821, significant advances in many fields - ranging from high speed analog circuitry to parallel computation - will allow us to both dramatically simplify and miniaturize the hardware while extracting significantly more information from the raw data.

The E821 400 MHz waveform digitizer (WFD) hardware was based on an earlier design from the MACRO experiment. It consisted of an analog input shaper, a clock input module, the Flash digitizer itself, a data formatter, discrete RAM banks, and a VME32 interface. The relatively low RAM densities available at the time coupled with stringent realtime processing constraints required the time consuming design and high-cost implementation of a custom data formatting ASIC. Current off-the-shelf and custom WFD designs are generally similar, but typically contain on-board FIFO memories. The main difference lies in the replacement of the inflexible custom ASICs with field programmable logic (in the form of FPGAs or CPLDs). We have deployed such a design for use in the MuLan and MuCap precision muon lifetime experiments at PSI.

For the New $g-2$ Experiment, we propose a departure from this model. FPGA based designs excel at manipulating very low level, realtime logic transformations, including such things as ADC readout, memory controllers, and network transceivers. High level data manipulation on the devices, however, is complicated by relatively high implementation, testing, and debugging barriers. These manipulations are much better done in high level computer programming languages on commodity hardware. We propose a hybrid design that merges the strengths of each approach, while minimizing engineering, construction, and deployment costs.

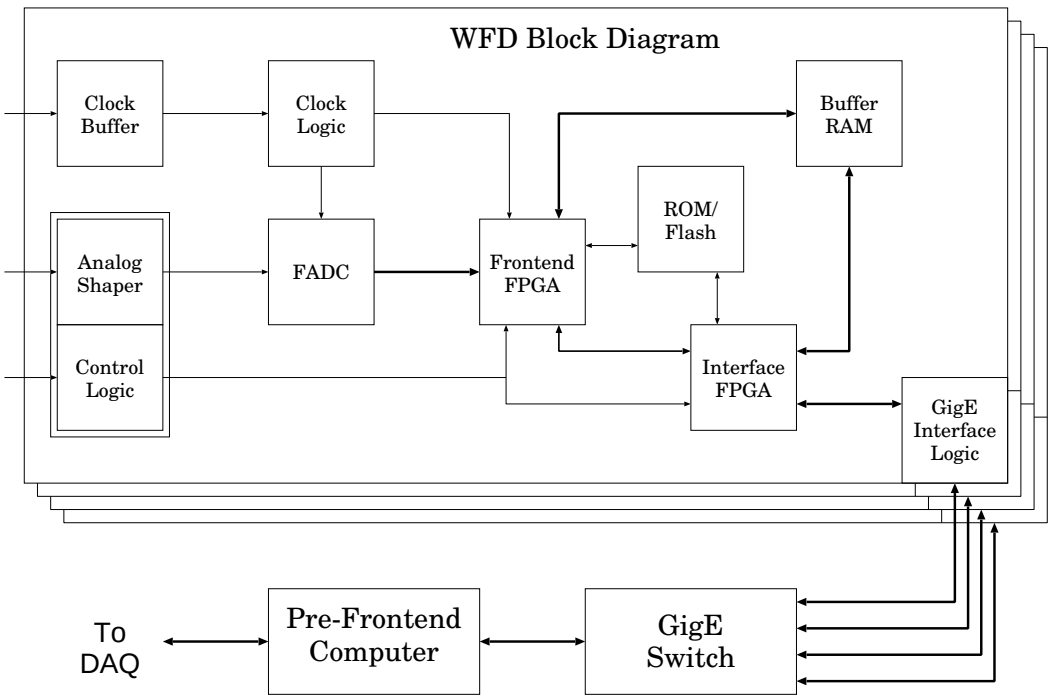

FIG. 41: A block diagram of the hybrid waveform digitization system.

The time structure of PMT pulses requires digitizing the output data stream at 500 MHz with an 8 bit flash digitizer. We will continuously digitize these signals, recording 600 μs of data per calorimeter segment per fill. Having every sample of each fill permits simultaneous extraction of T-method, Q-method, and other derived data streams from one digitization record. Ideally, we would simply send all of these raw data to persistent storage. With 24 calorimeters, however, the total raw data rate is 3-5 GB/s (depending on segmentation), significantly too great a rate to store completely. The DAQ system needs to reduce this, to of order 50-100 MB/s; the final value will of course depend on details of the DAQ system and the available FNAL network infrastructure and data storage resources at the time the experiment is run. To meet this challenge, the hybrid digitization system will operate in two stages: a simple hardware digitizer to record the data, and "pre-frontend" computers to perform all triggering, data selection, and packaging tasks. The hybrid system will present a configurable set of packaged data streams (*e.g.* T/Q-method datastreams) to the DAQ system for collation and storage.

Each WFD hardware channel will consist of analog and clock input stages, a 500 MHz flash digitizer, buffer memories, the communication interface, and various support modules (firmware PROMS, programming and test ports, LED feedback, synchronization hardware,

etc.). These will be tied together with one or more FPGAs to move the data at high speed between the various functional blocks (see Figure 41). Minimizing the duration of the design life cycle is of great importance, and we approach this in part by using off-the-shelf technologies whenever possible:

- We intend to use standard DDR computer memories in a bank switched configuration, instead of more expense FIFO memories. This allows simultaneous storage of the current fill while reading out the previous fill. It also permits use of previously written and debugged memory controller firmware.

- Every channel will operate independently (although multiple channels may be carried on one physical circuit board, they should share no processing or interface resources); this simplifies the firmware for setup and communications, as well as simplifying replacement of failed channels.

- The boards will be mounted in VME-style crates to supply the large quantities of power needed, but the communications interface will be Gigabit (or faster) ethernet. Again, debugged firmware modules are readily available, and custom interconnect topologies can be implemented with inexpensive commercial hardware. We may even consider UDP or TCP transport instead of using raw ethernet communications.

- The raw data can be compressed before transport if necessary. We will utilize a standard algorithm (such as the LZ77 algorithm embodied in the ubiquitous gzip library) to minimize implementation and debugging costs.

As each WFD channel is independent, while positrons will typically deposit energy in multiple calorimeter segments, triggering decisions must be made globally over each calorimeter. In the past, we might have performed this task in a separate analog module which would then force digitization in each WFD channel. Recent advances in multicore and parallel computation (embodied at the consumer level, for instance, in the popular Intel Core2 CPU architecture) and practical parallel programming techniques will allow us to perform this task cost effectively with off-the-shelf hardware and software written in a high level language. For our needs, General Purpose Graphics Processing Units (GPGPUs), consisting of multiple high-speed floating point units with hundreds of cores per die, are becoming readily available at low cost. The available programming interfaces, such as NVIDIA's CUDA,

AMD's Stream, and the developing OpenCL standard hide the complexity of data transfer and core scheduling, permitting relatively simple access to these massively parallel resources.

Each calorimeter station, then, will have a dedicated "pre-frontend" computer that will perform WFD readout and triggering for a given calorimeter. This pre-frontend will decompress and reformat the WFD data to optimize computation speed. It will then perform a number of parallel computations over each calorimeter:

- For the T-method, equal-time samples must be summed over all calorimeter segments, triggers identified, and "data islands" formatted and written to a data stream.
- For the Q-method, blocks of consecutive samples must be combined and summed across calorimeter segments. Successive fills can being summed together to further reduce the data rates.
- A potential new approach to pileup correction sums multiple successive fills before performing the T-method triggering decisions. This additional "Pileup T-method" stream could be easily derived from multiple recorded streams, and saved along with the standard T-method data set.
- Occasionally, entire fill records should be stored for detailed studies of, for instance, gain and pedestal stability.

Each of these potential computations, and others that are identified in the future, can be independently formatted, packaged and presented to the DAQ system for persistent storage. By performing all of this high level physics in software we can defer the actual specification of the final data streams until very late in the experiment, once physics studies and data acquisition performance tests have been performed.

E. Clock Systems

A time base having 0.01 ppm absolute accuracy and stability over several months is not difficult to obtain; vendors such as Precision Test Systems and Agilent provide inexpensive synthesizers driven by ovenized oscillators which meet that specification. In the MuLan experiment, for instance, the 500 MHz system clock which drove the WFDs was generated with an Agilent E4400 synthesizer. Extensive comparisons with external standard oscillators,

both before, during, and after the experiment, confirmed the stability and accuracy claims of the manufacturer. The long term stability of such devices can be economically extended to cover the multiyear duration of this experiment by slaving the master synthesizers to a common GPS-disciplined 10 MHz frequency standard.

Similar synthesizers will be used in the present experiment to drive the various acquisition and NMR systems and we point out that any errors in the master clock cancel out in the ratio ω_a/ω_p. We have extensive experience in distributing similar clock signals in other precision experiments, using low skew linear fanout and amplifier modules from companies such as Miniciruits. The final component of the clock system design is a robust blinding methodology; we hide the absolute clock frequencies from the ω_a and ω_p analysis teams until the analysis is completed. These are well understood techniques with very low design and implementation risks.

F. Data Acquisition

By comparison to E821 the New $g-2$ Experiment will record about 21× the decay electrons at ∼1.5× the rate per fill and ∼6× the rate per second. Moreover, the experiment will record the signals from the individual calorimeter segments rather than the calorimeter-segment sums, and record T-method datasets (comprising digitized pulses islands), Q-method datasets (comprising digitized fill periods) and other derived datasets. In addition, the new readout must incorporate the new straw counter arrays and account for the different beam time structure.

The new data acquisition must handle both very high data rates (∼80 MB/sec) and very large raw data volumes (∼1 PB total). It must transfer both the event data from various detector sub-systems to the mass storage devices and the experimental parameters from the various diagnostic sub-systems to an experiment database. Moreover, the readout system must be deadtime-free during the measuring periods in order to avoid any distortions of the time spectrum of the decay positrons. Finally, the DAQ must be flexible enough to use for the installation, testing, diagnostic and production phases of the experiment.

The DAQ (see Fig. 42) will be implemented as a modular, distributed acquisition system on a parallel, layered processor array using multi-threaded PC's, a Linux platform and a multi-layered Gbit network. A frontend (FE) layer will be responsible for the readout of

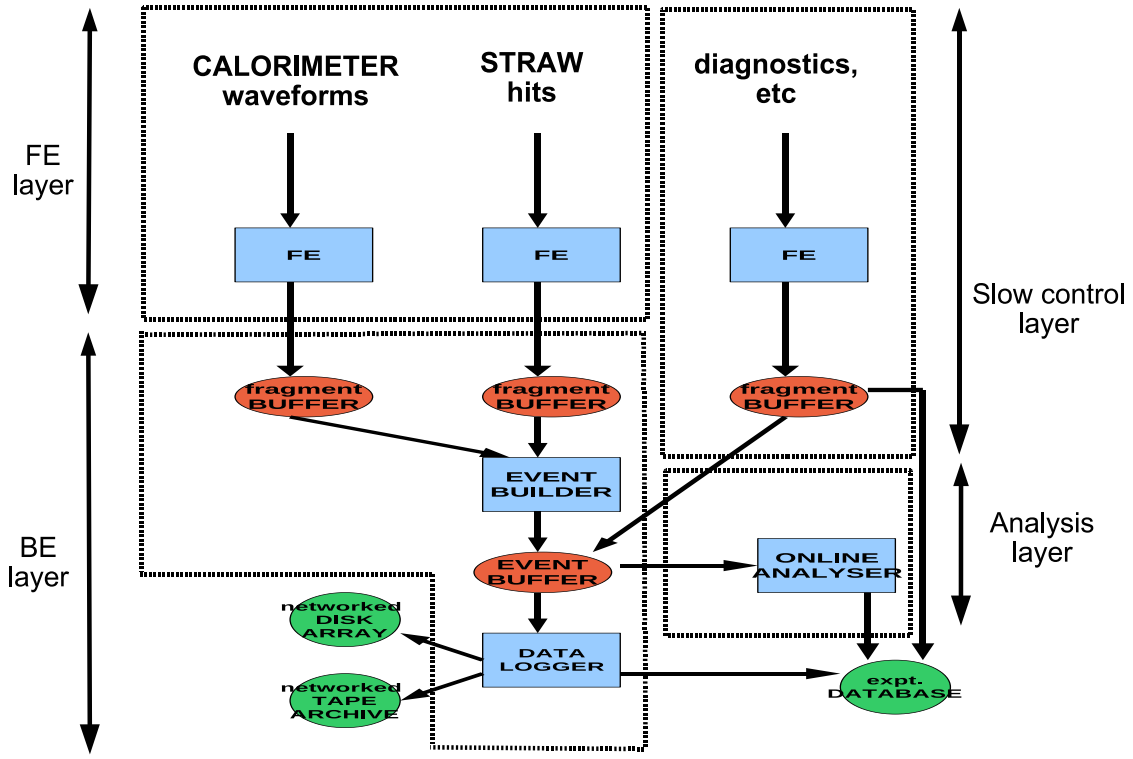

FIG. 42: Schematic layout of the anticipated DAQ system.

the calorimeter segment waveforms, straw counter hits and other detector sub-systems. The backend (BE) layer will be responsible for both the assembly of data fragments into complete events and the permanent storage of the complete events. A slow control layer will be responsible for the control and monitoring of diagnostic instrumentation associated with the ring, detectors and other sub-systems. Finally, an online analysis layer will be responsible for the integrity-checking and basic histogramming that ensures the overall quality of recorded data.

The primary source of high-rate data is the twenty-four calorimeters. As described earlier, each calorimeter segment is instrumented with one waveform digitizer channel that transmits packets of 500 MHz, 8-bit, continuous digitization (CD) data to so-called pre-FE processors. These pre-FE processors derive the Q/T-method data-streams and transmit the resulting derived databanks over the FE network to the FE layer of the data acquisition. We expect

a total rate of calorimeter Q/T-method data of roughly 80 MB/sec.

A second source of high-rate data are the straw counter arrays. We envisage a straw counter readout system based on commercial VME multi-hit TDCs and VME-to-PCI interfaces that deliver their data to a dedicated FE processor on the FE network. We expect a total rate of straw counter data of several MB/sec.

The backend layer will receive data fragments from the various frontend processors across the frontend network, assemble the event fragments into complete events, and copy the events to mass storage. Each event will represent a time-ordered history of the calorimeter, straw counter, and other detector data for one entire fill. For mass storage we propose to store one copy of the data on the Fermilab tape archive (*i.e.* the Fermilab Enstore system or its future equivalent) and one copy of the data on a large disk array (*e.g.* a BlueArc storage node or its future equivalent). The event building will utilize backend local memory segments for temporary buffering of event fragments and the data logging will utilize backend local disks for temporary buffering of complete events.

The slow control layer is essential for careful monitoring of systematic issues and will incorporate the readout of instrumentation such as HV controls, current monitors, temperature sensors, field probes and scalars. The slow control readout will operate in periodic mode and be asynchronous to the beam cycles, DAQ cycles, *etc.* The slow control data will be written to both the mass storage devices and the experimental database.

The online analysis layer will provide the integrity checks and diagnostics plots that ensure the quality of recorded data. The online analysis system will be resident on a dedicated network and receive events as 'available' from the backend layer (in order to avoid the introduction of unnecessary deadtime). The system will provide for both local and remote access to the experimental data.

G. Systematic uncertainties on ω_a

In this section we consider the primary systematic errors on the ω_a analysis, which totaled 0.19 ppm in the final run of E821. [149] Our goal in the New $g-2$ Experiment is a factor of 3 reduction for a total of $\leq$ 0.07 ppm. This goal can be met by incorporating a suite of improvements to the experiment. Here, we briefly outline the plan to reduce the largest sources of systematic error: gain changes, lost muons, pileup, coherent betatron oscillations,

and the uncertainty associated with the electric field and pitch corrections. Table XIII lists the final E821 uncertainties and projections for improvements in the New $g-2$ Experiment. The traditional T method analysis is assumed because uncertainties can be reliably projected based on our considerable experience in these analysis efforts. Since the Q method is new, we have not included its positive and partially independent impact on the final statistical result, nor are we able to fully project associated systematics. One key attractive feature of the Q method is pileup immunity; there is no correction necessary so that systematic uncertainty is absent. Comparing the analysis results using both T and Q methods will provide a valuable confirmation that systematic errors are understood.

1. Gain changes and energy-scale stability

The hardware gains of the detectors were determined to be stable to ≈0.15% from early to late times within a storage ring fill. This limit was established by plotting the average energy for each $(g-2)$ period versus time after the PMTs were switched on. The gating circuitry in the base that allowed the PMTs to be turned off to avoid the initial burst of pions entering the ring, also resulted in a variation in the gain. For gain variations like this one, where the time constant is long compared to the $(g-2)$ oscillation period, the coupling to the ω_a frequency is small and after correction the residual systematic error is less than 0.02 ppm.

If the gain oscillates at a frequency ω_a, with an amplitude that varies in time, and with a phase that differs from that of the ω_a oscillation of the positron sample, then a direct error on the measured value of ω_a is produced. The average rate at which energy is deposited into the calorimeters oscillates with frequency ω_a, and therefore any rate dependence in the gain of the detectors produces gain oscillations. We were able to demonstrate that the gain dependence on rate was small enough that its effect on ω_a was typically less than 0.03 ppm. In the new experiment, the slightly increased beam rates will be offset by increased detector segmentation. In E821, a UV-laser system was used to periodically pulse the scintillator in the detectors and thus monitor the complete gain and reconstruction chain during data collection against an out-of-beam reference counter. Unfortunately, the light distribution system included too many branches and only one upstream reference detector. Small fluctuations cascaded so that gain stability could be monitored to no better than a

few tenths of a percent. At PSI, we have recently built and used a simplified version of this system, which monitors hardware gains at the sub-0.1% level by having a monitor on a parallel level to that seen by the detectors. We intend to incorporate a similar system in the New $g-2$ Experiment to largely eliminate this uncertainty.

The greater contribution to the gain systematic error came from artificial gain oscillations at the ω_a frequency, introduced by the data reconstruction software. Here, the "energy-scale" stability is related to software reconstruction of waveforms. When a signal was above the WFD hardware threshold, a pre-set minimum number of sequential WFD samples was recorded. These data were fit offline for the peak plus linear background to deduce the energy and time of the positron. But, if the trigger pulse was followed or preceded closely by another pulse, both pulses were fit together with a common background term, and the fitting region becomes longer compared to that used for a single pulse. The fitted energy was found to depend slightly on the length of the fitting region and the fitting samples were fixed in number by hardware. Because the data rate oscillates at frequency ω_a, and is higher at early than at late decay times, it follows that the fitting region length oscillates at ω_a and is, on average, longer at early times compared to late times. This produces a small, effective gain oscillation with frequency ω_a whose amplitude decreases with time, leading to a systematic error on ω_a. Given the current capabilities in data throughput, the new electronics will record all samples in place of isolated islands, thus removing the source of this reconstruction bias. In summary, the larger of the gain systematic pieces will be eliminated by design and the smaller contribution will be monitored more precisely.

2. Lost muons

"Lost muons" refers to muons that escape the storage ring before they decay. These losses were about 1% per lifetime at early decay times and decrease to about 0.1% at later decay times in the BNL experiment. One consequence of losses is that, in a fit to the data, the lifetime is not quite correct. This is a slow change in the spectrum, having no ω_a frequency component; therefore the correlation to ω_a in the fit is small. However, even though the correlation is small, neglecting muon losses in the fit in E821 would have shifted the ω_a frequency by 0.18 ppm and resulted in a very poor χ^2 from the fit. By monitoring the muon losses with hodoscopes on the front of 14 of the calorimeters in E821, the muon loss profile

was constructed and the resulting uncertainty was held to better than 0.03 ppm. In the upgraded experiment, all 24 calorimeters will incorporate muon sensitive detectors, straws or scintillator, allowing muon losses to be monitored around the entire ring. Furthermore, an open-ended inflector will reduce scattering of muons entering the storage ring, resulting in better storage efficiency and consequently smaller muon losses. Finally, muon losses can be greatly reduced when an effective "scraping" strategy is employed. During scraping, the stored muon orbit is shifted so that outliers in the phase space are lost on collimators during the first 20 μs after injection. In the 2nd half of the final E821 run, this technique resulted in an order of magnitude reduction in the losses during the ω_a fitting period.

The muon losses entry in Table XIII arises mainly from the uncertainty in the possible difference between the average phases for stored and lost muons. For example, one source of muons, carrying a different phase and potentially lost at a higher rate, are those created after the momentum-selecting slit just upstream of the inflector. These muons, born from pion decay in that short region, have a different phase compared to those captured in the decay channel (the later muons did not go through the final dipole bend, which precesses the muon spin). In a 900-m long decay channel as we assume at FNAL, the population of muons born in the last turn into the storage ring will be essentially negligible and will be dwarfed fractionally by those born in the long AP2 decay channel. While this uncertainty can almost be eliminated, we include a small estimate here of 0.02 ppm for smaller possible contributions to the fitting.

3. Pileup

The error due to pileup scales linearly with rate in each segment of the detectors. The effective size of the segment depends on the geometric extent of the shower. A simulation was used to demonstrate that the new W/SciFi calorimeters, having 20 or 35 independent segments, and a smaller Moliere radius, will provide an effective five-fold reduction in the intrinsic pileup. With no further improvements, and the proposed factor of up to 3 increase in data rate, the pileup error would be reduced by at least 3/5 to 0.048 ppm. While we could accept this level of error, some improvement is desirable and achievable.

In the past, an artificial pileup spectrum was constructed from individual pulses in the data, then subtracted from the raw spectrum. In the pileup construction, it is necessary to

use pulses with pulse heights below as well as above the hardware threshold. Because of the relatively high hardware threshold and limited storage of the E821 WFD system, those pulses below threshold were only found by searching during the relatively short period of continuous WFD digitization following the trigger generated by the presence of a large pulse above threshold. Consequently, the sample size for pileup events was limited and somewhat biased, since they had to always ride on the tails of larger pulses. In the new data WFD and data acquisition scheme, it will be possible to significantly improve the pileup construction process. Continuous digitization, with local software sorting of data streams including T-method, Pileup T-method and Q-method datasets, is anticipated. Pulses of all heights can be searched for independent of whether there is a nearby large pulse that fired a hardware trigger.

In E821, signals from four detector segments were combined before WFD digitization. Any mismatch in the relative timing of these signals can lead to variation in the pulse shape of the sum. In addition, the scintillator fiber in the calorimeters was strung radially, causing the pulse shape to depend slightly on the radial entrance position into the detector. These variations in the pulse shape hampered efforts to handle pileup, both in the fitting of two nearby peaks, and in the process of constructing the pileup spectrum. The pulse shape is expected to be more stable in the new design, because each segment will be individually digitized. In addition, the E821 WFDs were composed of two 200 MHz ADCs that sampled the pulse shape out of phase and were later stitched together to form a 400 MHz record. The upgraded experiment will employ single phase 500 MHz WFDs based on a similar design that we have already successfully used in muon lifetime experiments at PSI.

The contribution of pileup to the error in ω_a for E821 was divided into three components. The first two are correlated and add linearly. The third is not correlated so it is added in quadrature to the other two.

1. Pileup efficiency, 0.036 ppm. This is due to an estimated 8% uncertainty in the amplitude of the constructed pileup spectrum.

2. Pileup phase, 0.038 ppm. This is the error due to the uncertainty in the phase of the constructed pileup spectrum.

3. Unseen pileup, 0.026 ppm. This is the error due to pulses so small that they cannot be reconstructed and therefore they are not included in the pileup construction.

We expect that the lower rate per detector segment in the new experiment, coupled with the new full-energy data stream will lead to a comprehensive pileup correction with minimal uncertainty. We assign up to 0.04 ppm here to account for any difficulties in the anticipated analysis. As mentioned earlier, the Q method is complementary to the traditional T method and has different sources of systematic errors. The most significant difference is the effect of pileup—it is greatly reduced for the Q method.

4. Coherent betatron oscillations

The average position and width of the stored beam can vary as a function of time as the beam alternately focuses and defocuses in the ring. This imposes an additional time structure on the decay time spectrum because the acceptance of the detectors depends on the position and width of the stored muon ensemble.

The CBO frequency lies close to the second harmonic of ω_a, so the difference frequency $\omega_{\rm CBO} - \omega_a$ can be quite close to ω_a, causing interference with the data fitting procedure and thereby causing a significant systematic error. This was recognized in analyzing the E821 data set from 2000. In the 2001 running period the electrostatic focusing field index was adjusted to minimize this problem. This greatly reduced the CBO systematic uncertainty. We will follow this tuning strategy again.

In addition, several efforts are underway to reduce the CBO effect even further. They include:

1. Improve the kicker pulse shape to better center the beam on orbit.

2. Use active RF schemes at very early decay times to reduce the amplitude of the CBO (see Appendix B).

3. Use an octupole E or B field at very early decay times to damp out the CBO amplitude (see Appendix B).

4. Increase the vertical size of the detectors. This reduces losses of positrons passing above or below the detector, reducing sensitivity of the detector acceptance to beam position and width.

The combined efforts should reduce the CBO uncertainty by a factor of 2 to 0.04 ppm.

5. Electric field and pitch correction

With a vertical magnetic field B_y and radial electric field E_r, the precession frequency is given by

$$\omega_a = -\frac{q}{m}\left[a_\mu B - \left(a_\mu - \frac{1}{(\gamma^2-1)}\right)\beta E_r\right]. \tag{39}$$

If B_y and E_r vary with position, the time averages $\langle B_y\rangle$ and $\langle E_r\rangle$ should be used. At exactly the magic momentum the effect from E_r is zero. Muons of slightly higher momentum δp have an equilibrium orbit

$$x_e = \frac{R_o}{1-n}\cdot\frac{\delta p}{p}.$$

As they oscillate about this equilibrium orbit they experience a mean electric field $\langle E_r\rangle = n\,(\beta B_y/R_0)\;x_e$ and their deviation from the magic momentum is proportional to x_e. This leads to a correction to ω_a proportional to x_e^2. In this experiment n is measured from the observed horizontal betatron frequency, and the distribution of muons with respect to x_e is found from the modulation of counting rate by the rotation frequency of the muon bunch. The observed value of $< x_e^2 >$ was confirmed by simulation. The correction is 0.46 ppm.

With electric focusing, the plane in which the muon spin is precessing oscillates vertically, exactly following the oscillation of the muon momentum. When the orbit is inclined at angle ψ to the horizontal, ω_a is reduced by the factor $(1-\frac{1}{2}\psi^2)$. If ψ_m is the angular amplitude of the vertical oscillation, the average over the ensemble of muons is $(1-\frac{1}{4}\langle\psi_m^2\rangle)$ where the brackets indicate an average over the muon population, $\langle\psi_m^2\rangle = n\langle y_m^2\rangle/r_o^2$ where y_m is the amplitude of the vertical oscillation.

Information on $\langle\psi^2\rangle$ is obtained by simulation in which a representative set of muons is tracked around the ring from the inflector exit, via the kicker magnet, for many turns. The discrete quadrupole structure and aperture defining collimators are included as well as the calculated deviations from a pure quadrupole field. The pitch correction is +0.29 ppm.

A combined (correlated) electric field and pitch correction uncertainty of 0.05 ppm was used in E821. We expect to improve on our knowledge of the electric field and pitch corrections by use of a new muon traceback system that can better image the beam motion versus time at a number of azimuthal positions around the ring. Furthermore, our simulation effort has improved, which is essential to some of these corrections. It is certainly feasible to reduce the uncertainty on these important corrections and we estimate a final combined error of 0.03 ppm.

TABLE XIII: The largest systematic uncertainties for the final E821 ω_a analysis and proposed upgrade actions and projected future uncertainties for data analyzed using the T method.

E821 Error	Size [ppm]	Plan for the New $g-2$ Experiment	Goal [ppm]
Gain changes	0.12	Better laser calibration and low-energy threshold	0.02
Lost muons	0.09	Long beamline eliminates non-standard muons	0.02
Pileup	0.08	Low-energy samples recorded; calorimeter segmentation	0.04
CBO	0.07	New scraping scheme; damping scheme implemented	0.04
E and pitch	0.05	Improved measurement with traceback	0.03
Total	0.18	Quadrature sum	0.07

6. ω_a systematic uncertainty summary

Our plan of data taking and hardware changes address the largest systematic uncertainties and aims to keep the total combined uncertainty below 0.07 ppm. Experience shows that many of the "known" systematic uncertainties can be addressed in advance and minimized, while other more subtle uncertainties appear only when the data is being analyzed. Because we have devised a method to take more complete and complementary data sets, we anticipate the availability of more tools to diagnose such mysteries should they arise. Table XIII summarizes this section.

IX. PARASITIC MEASUREMENT OF THE MUON ELECTRIC DIPOLE MOMENT

As has been discussed earlier, the magnetic moment of the muon is a sensitive probe for new, TeV-scale interactions. If the new interactions also contain CP-violating phases, these phases will give rise to an electric dipole moment (EDM) of the muon. Contrary to the muon magnetic moment, there is no EDM expected in the standard model at a measurable level and thus any signal indicates new sources of CP violation beyond the standard model [130]. As noted in several places, the search for extra sources of CP violation is strongly motivated since the CP violation observed in the quark sector so far is insufficient to explain the matter dominance of the universe [131].

If the CP-violating phases of the new interactions are independent of lepton flavor, the muon EDM will be related to the electron EDM by simple mass scaling. In this case, the current electron EDM limits rule out the ability to discover a muon EDM with the $g-2$ experiment proposed here. However, as discussed below, a muon EDM measurement performed with the proposed experiment could potentially extend the exclusion of flavor-dependent CP-violating interactions by 2 orders of magnitude. This would probe models with non-trivial mass scaling such as Randall-Sundrum extra dimensions that allow for a muon EDM within 1 order of magnitude of the current limit [132].

The phenomenology of a muon EDM is described in detail in Ref. [15, 133]. The muon dipole moment is related to the muon spin by

$$\vec{d_\mu} = \frac{q}{2m}\eta_\mu \vec{s}$$

with η_μ playing a similar role to the g factor for the magnetic moment. The muon precession receives components from both the anomalous magnetic moment, a_μ, and η_μ. At the magic momentum we have

$$\vec{\omega}_a = -\frac{q}{m}a_\mu \vec{B},$$

$$\vec{\omega}_{\rm EDM} = -\frac{q}{2m}\eta_\mu \left(\vec{\beta}\times\vec{B} + \frac{\vec{E}}{c}\right) = -\frac{\eta_\mu}{2mc}\vec{F}.$$

Although the muons are in a uniform magnetic field, in the muon rest frame, the muon sees a large motional electric field in the horizontal plane. This gives rise to a torque on the muon spin vector that will act to tilt the precession plane away from the vertical direction

by an angle

$$\delta = \tan^{-1}(\eta_\mu \beta / 2a_\mu).$$

The modulation in the vertical plane is sinusoidal and 90° out of phase with the a_μ modulation.

The E821 collaboration has recently published a measurement of the muon EDM by including an up-down asymmetry, offset by 90° in the ω_a fit yielding an upper limit of $|d_\mu| < 1.9 \times 10^{-19}$ e cm [15] which is a factor of 5 improvement over the previous best limit [134]. Results of the fit are displayed in Fig. 43. The measurement was performed in part using straw-tube tracking detectors [135] that were designed to determine the muon beam distribution within the storage ring and instrumented in front of one of the 24 calorimeter stations.

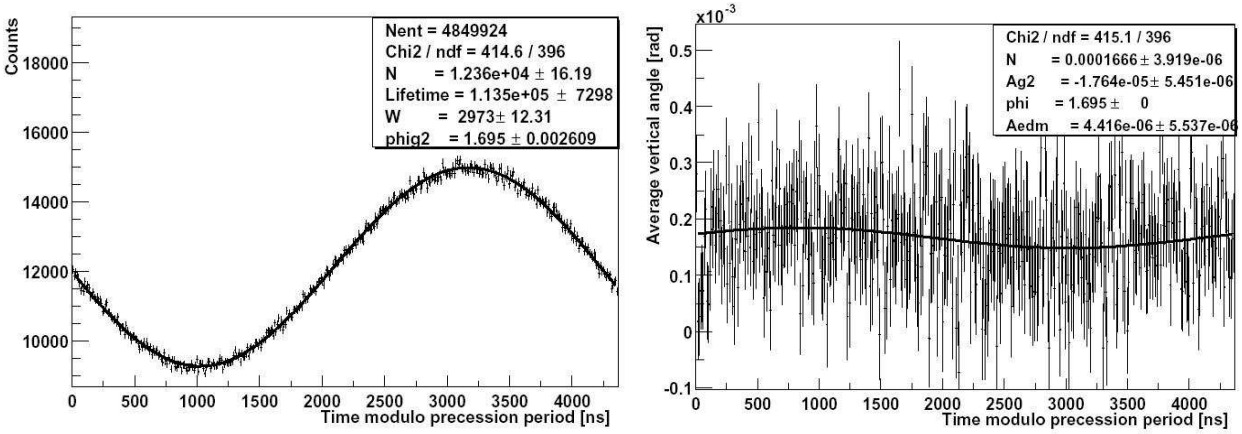

FIG. 43: Data recorded by the E821 traceback system. The left distribution is the number of tracks versus time modulo the precession frequency. The right distribution is the average vertical angle of the tracks versus time also modulo the precession period.

A. E821 Traceback System

There are three main components to performing the $g-2$ measurement: measurement of the precession frequency; measurement of the magnetic field; and measurement of the spacial distribution of muons within the field. The muon spacial distribution can be mapped by measuring the positron trajectories and extrapolating back to the point where the trajectory is tangent to the muon orbit. In E821, this was accomplished using a straw tracking system.

The system consisted of eight, three-layer straw planes, split equally between vertical and horizontal configurations as shown in Fig. 44. One of the 24 scallops in the $g-2$ ring was truncated to allow these chambers to be placed in front of one of the calorimeter stations and outside of the vacuum chamber. The decay point of the muon was required to be known within 3 mm in both the radial and vertical position, which led to a requirement of better than 100 μm position resolution per straw [135]. Similar requirements are needed for the experiment proposed here.

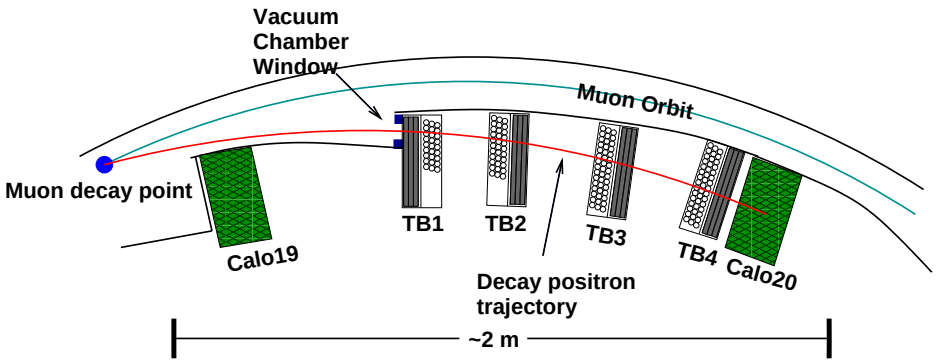

FIG. 44: Top view of the E821 traceback straw tracking system.

B. Improved Traceback System

There were a few known limitations to the E821 traceback system which can be remedied in the next experiment. As shown in Fig. 44, one of the 24 scallops was truncated and a small mylar window was installed defining the acceptance of the tracking volume. This acceptance means that the muon beam is imaged between 1 and 2 meters in front of the first track measurement. Beam elements such as collimators were present between the imaged muon decay region and the tracking volume further limiting acceptance. The momentum acceptance of the system was also not well matched to the 1-2 GeV positrons that have the maximum asymmetry for an EDM. The truncation of the scallop also lead to a very different acceptance for the calorimeter station behind the straws and this calorimeter station was eventually excluded from the final a_μ measurement.

All of the above limitations can be removed by placing tracking detectors inside the beam pipe in the scallop region as shown in Fig. 45. In particular, the muon decay region can be imaged much closer to the first tracking station and the acceptance can be maximized for 1-

to 2-GeV positrons. Several planes of $X-Y$ straws can be placed within the vacuum. The high voltage, signal, and gas systems can be serviced using ports that already exist in the vacuum chamber as shown in Fig. 45. Three scallop regions have a clear line of sight to the muon beam. The other 21 are blocked by the quadrupoles, kickers, or other beam elements. We intend to instrument all three to allow for higher statistics and the ability to image the muon beam in more than on place around the ring.

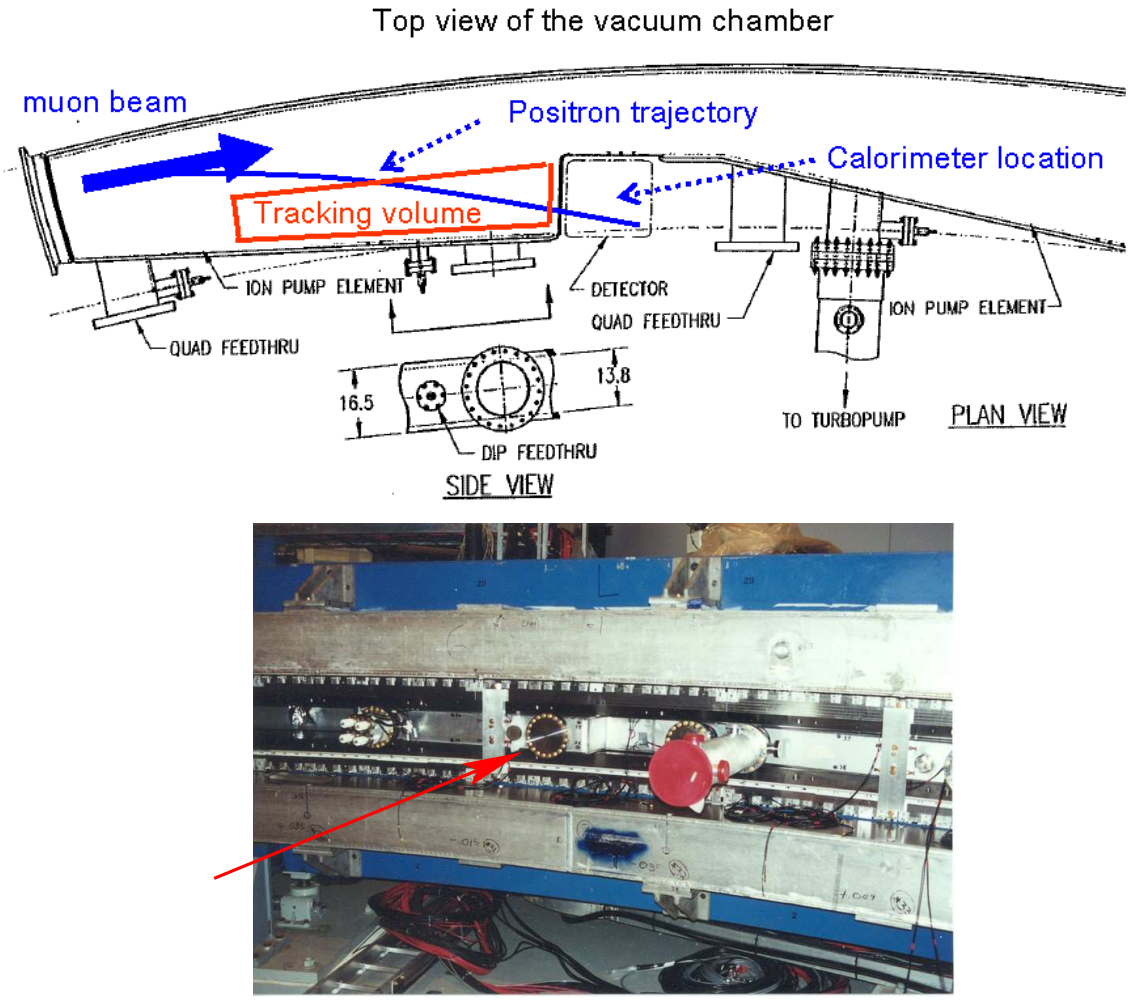

FIG. 45: Top: Top view of the beam pipe indicating the position of the tracking volume. Bottom: picture of available ports.

Design and production of the tracking system will be a joint effort of Fermilab and PNPI (St. Petersburg). An R&D program is currently underway at Fermilab to demonstrate the feasibility of such a tracking system. The program is a collaboration of Fermilab scientists

working on $g-2$ and the Mu2e experiment that also intends to use straws within their vacuum chamber. Scientists from the Fermilab Geant4 team are also collaborating with Boston University on the simulation effort and are interfacing straw detector simulations into the existing Geant4 $g-2$ ring simulation. Two Fermilab postdocs have also joined the effort and will gain hardware experience working on the straw effort while performing analysis of Tevatron data. This program builds largely on experience gained from the CKM R&D program to develop straws in vacuum [136].

X. COLLABORATION, TIMELINE AND BUDGET

A. Collaboration

We have formed a new collaboration to carry out this measurement, which represents a healthy ratio of former E821 collaborators along with strong new institutions. Fortunately, much of the expertise built up in E821 is represented and still available to us. We retain senior experts in the collaboration who cover all of the different technical areas. New institutions bring creative input and additional technical capabilities. These groups include the host laboratory—Fermilab—and new university groups at James Madison, Kentucky, Massachusetts, Michigan, Regis, and Virginia. New international groups include KEK and Osaka from Japan, KVI-Groningen from The Netherlands, Frascati and Rome from Italy, and PNPI from Russia. The Muons Inc. team has also joined the effort. In some cases, experienced younger E821 collaborators are associated with their new institutions. The names listed on the proposal masthead are mainly senior physicists. As the experiment develops, we expect postdocs and students to sign on; indeed, with funding approval, we will immediately begin a vigorous campaign to enlist the talents of young people. We are proud that E821 offered a rewarding experience for dozens of postdocs and graduate students and we intend to welcome young physicists in the new effort.

B. Timeline Overview

A technically driven timeline for expeditiously mounting the $g-2$ has been outlined in Figure 46. Mounting the experiment at Fermilab for a factor of four improvement in the measurement of a_μ will require moving the storage ring and subsystems from BNL to FNAL, preparing a 3 GeV muon beam with some modifications to the existing accelerator complex, and delivering that beam to a new experimental hall where the experimental apparatus will be reassembled.

The lynchpin that anchors the critical path in Figure 46 is the shutdown of Tevatron Run II operations, currently scheduled to conclude at the end of FY2011. Once pbar production has ceased, the excavation required to connect the AP1 line to a new building located just SE of the AP0 target hall can begin without concern for disrupting Tevatron operations or the need for radiation-training of the civil construction contractors. The Project Definition

Report from FESS requires a 9-month period from the start of construction until beneficial occupancy can take place. In order to be ready to break ground shortly after the Tevatron shuts down, the final design and engineering must be completed in the 12 months leading up to the construction start. The building engineering and construction phases are indicated in red in Figure 46.

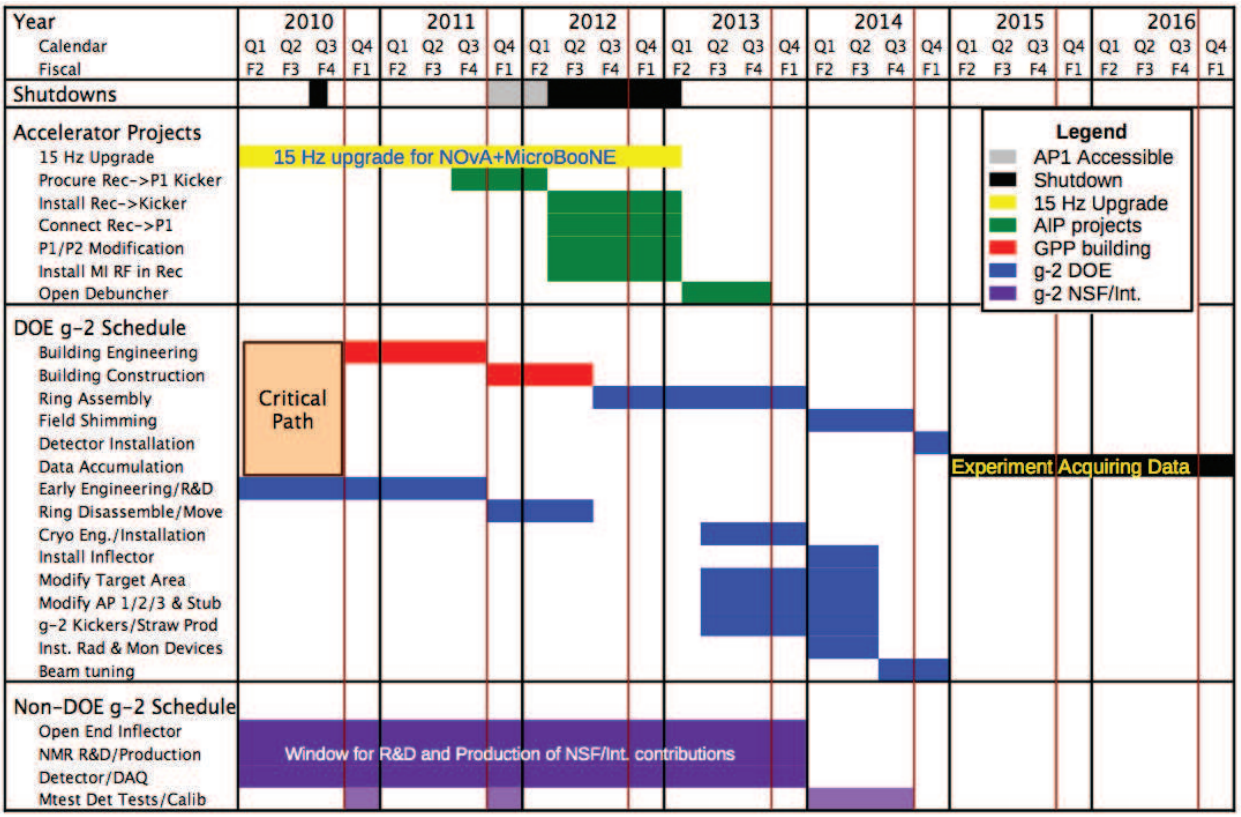

FIG. 46: Overview of timeline for the muon $g-2$ experiment. Project items are broadly divided into accelerator upgrades (green), construction of beam tunnel and building (red), $g-2$ specific DOE-funded tasks (blue), and tasks funded through non-DOE sources (purple). A technically-driven critical path is shown that would enable data acquisition to begin at the end of 2014.

Once the building is in place, reconstruction of the storage ring can begin. From detailed consultation with Brookhaven engineers and technicians responsible for the initial construction of the storage ring, it is expected that reassembly of the ring will take 18 months assuming a team of 5 technicians. Once the ring is assembled and functional, precision shimming of the magnetic field will take 9 months. After a 3 month period in which detectors are installed, electronics are cabled, and the DAQ is initialized, the experiment

will be ready to take data. With the above considerations, a total of 30 months is required between beneficial occupancy of the building and the start of data acquisition. The block of sequential critical path items is indicated on Figure 46 with $g-2$ project-specific DOE costs highlighted in blue.

With the critical path defined, the relative timeline for other project elements can be established. Although a more detailed WBS is under development, the remaining blue items in the timeline shown in Figure 46 show the estimated duration for other major elements, how they are ordered relative to the critical path, and where they fall with respect to the fiscal year outlay. Each of the remaining blue elements in Figure 46 is summarized below.

- **Early Engineering and R&D:** This is a catch-all category intended to include all aspects of the project that need support in FY2010/FY2011 in order to make design decisions. Efforts under this category include:
  - Establishing a project management office to produce the required WBS and CD documentation.
  - Finalizing all engineering required for moving the storage ring, especially with respect to the design of lifting fixtures and technical specifications for the Skycrane operations.
  - Working with BNL expertise to finalize disassembly and reassembly plans.
  - Modeling the AP0 targeting to understand if a more cost-effective target solution, similar to that used in the BNL experiment, can be used in place of the Li lens.
  - Establishing a test stand to explore the current capabilities of the Li lens system when pulsed at a higher rep rate but lower current.
  - R&D to develop the in-vacuum straw tube technology required for the simultaneous measurement of the μ electric dipole moment in the $g-2$ storage ring.
  - Early shipping of subsystems where ongoing R&D or FNAL-based refurbishment is required.
  - Producing a benchtop test station to characterize the performance of design improvements to the $g-2$ electromagnetic kickers.
  - Developing a preliminary design for a cryogenic delivery system.

- **Ring Disassembly and Transport:** During this 9 month period the storage ring yoke, superconducting coils, and cryogenic connections will be disassembled and prepared for transport. Any remaining subsystems or beamline elements will also be disassembled and prepared for shipping. The 600 tons of magnet steel will be shipped by barge along with the superconducting coils, where the duration of the voyage is expected to be about 1 month. For obvious reason,the barge delivery is required before ring construction can begin, thus dictating the placement in the timeline.

- **Cryo Engineering and Installation:** During this period the final engineering and construction of the cryo delivery system must be completed in order to power the magnet and be ready for the field shimming.

- **Inflector Installation:** The inflector is the final piece of the magnet/cryo system to be installed. Final shimming of the magnetic field will also require the inflector to be operational.

- **Modify Target Area:** During this time period any modifications to the target area need to be performed. Pending the outcome of future design work, this could include:

  - Replacing the Li lens with a more conventional doublet/triplet set of focussing quads.
  - Replacing the single-turn Pmag bending magnet with a multi-turn magnet.
  - Adjusting some of the upstream/downstream shielding.

- **Modify AP 1/2/3 & Beamline Stub:** During this time approximately 80 elements needed to be installed in the various beamlines that form the pion decay channel and provide the muon delivery into the storage ring.

- $g-2$ **Kicker and Straw Production and Installation:** The production of the improved kickers and the straw chambers needs to take place in FY2013, so that the scalloped vacuum vessels can be assembled and installed prior to shimming the magnetic field. Connections outside the storage ring to power supplies and readout electronics can take place during the shimming process.

- **Install Radiation and Beam Monitoring Devices:** These devices will be required before beam tuning can begin.

- **Beam Tuning:** A final stage of tuning beamline elements, adjusting targeting, and characterizing the beam profile will be required before data acquisition can begin in earnest.

While the above list is by no means exhaustive, it does present an overall picture of the project-specific tasks. There are many other subsystems not discussed explicitly in this document but that have been included in the 18 month assembly plan, e.g. installing storage ring quadrupoles, vacuum chambers, NMR probes and trolley system, vacuum components, etc.

In parallel to the DOE project-specific costs, work on the detectors, DAQ, and new inflector will proceed in parallel by our NSF-funded university groups and international partners.

1. Compatibility with other Fermilab experiments

In the NOvA era, it is assumed that the Booster will be upgraded to provide beam at 15 Hz. This is required in order to run any experiments requiring additional protons at 8 GeV, e.g. MicroBooNE, $g-2$, and Mu2e. The Booster already operates at a 15 Hz frequency but requires some upgrades to be able to load beam into the Booster on every cycle, most importantly planned upgrades to the RF system. NOvA will require 10 Hz from the Booster leaving 5 Hz available for other 8 GeV programs to run parasitically with no impact on the high-energy (120 GeV proton beam) neutrino program. An estimation of the beam available in this era can be taken from the MiniBooNE experiment. Currently MiniBooNE collects $2\,\mathrm{x}\,10^{20}$ protons on target (POT) per year using slightly less than 2 Hz from the Booster. This leads to an estimation of $1.1\,\mathrm{x}\,10^{20}$ POT/year$\cdot$Hz. Running the Booster at 15 Hz will require losses to be better controlled to avoid radiation limits. This can be accomplished in several ways, recently a new set of corrector magnets were installed in the Booster to help reduce losses. Also, the Booster typically gains an additional 10% in protons per pulse by wrapping an extra turn or two from the Linac. Since losses become non-linear with these extra turns, the turns in the 15 Hz era may have to be backed off. To be conservative we assume a total of $4\,\mathrm{x}\,10^{20}$ POT/year are available for other experiments to run in parallel with the NOvA program.

Experiment	Total Beam Request
MicroBooNE	$6.7\,\mathrm{x}\,10^{20}$ POT
$g-2$	$4.0\,\mathrm{x}\,10^{20}$ POT
Mu2e	$7.2\,\mathrm{x}\,10^{20}$ POT

TABLE XIV: Beam requests for 8-GeV protons running parasitically with NOvA.

By comparison, the beam demands of the relevant experiments are relatively modest. As shown in Table XIV, the total requested beam for the MicroBooNE, $g-2$, and Mu2e experiments is $18\,\mathrm{x}\,10^{20}$ POT. A tentative timeline for the data acquisition periods of each of the three experiments is shown in Figure 47. With two years per experiment, the integrated POT demands can be more than met.

Of course it is always possible that delays in experimental schedules, revised estimates for beam, problems with the Booster intensity, or physics discoveries could result in an extension of one or more of the experiments in question. It is worth considering how the experiments might run in parallel if needed. For MicroBooNE and $g-2$, the procedure is straight-forward. Beam can be shared on a pulse-by-pulse basis. This is evident because $g-2$ uses the same injection line from the Booster to the Recycler as NOvA. Since MicroBooNE and NOvA share beam on a pulse-by-pulse basis, MicroBooNE and $g-2$ can do the same.

For $g-2$ and Mu2e the situation is not so simple. Both experiments use very different beams in the Debuncher. In the case of $g-2$, a 3.1 GeV secondary muon beam is circulated in the clockwise direction, while Mu2e uses an 8 GeV primary proton beam circulating in the opposite direction. Beam cannot be shared on a pulse-by-pulse basis. However, the experiments can run in turns if needed with less than two weeks downtime for switchovers. This may seem like a disadvantage, but in precision beam experiments this mode of running is often very advantageous. It allows for periods of time where the data analysis can catch up and insight from that analysis can be used to modify experimental conditions for better control of systematic errors. In fact, these type of downtimes were an integral part of the success of the BNL $g-2$ experiment, which ran four months of every year it operated. Even if the two experiments do not overlap in their data acquisition, it would probably be best to run $g-2$ interleaved with scheduled shutdowns in which Mu2e can have unhindered access for installation.

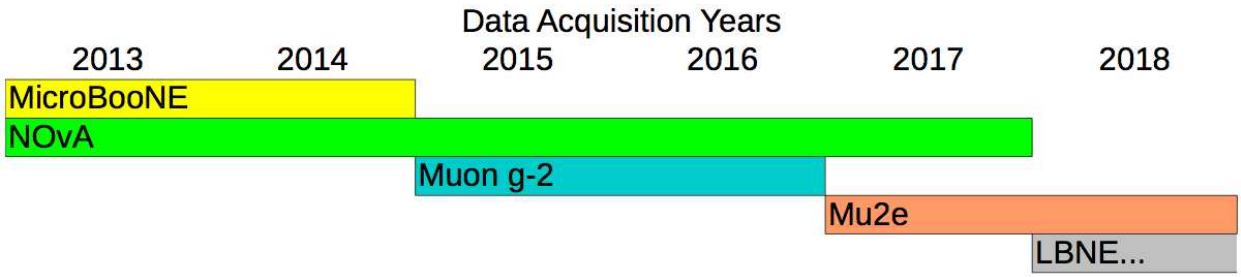

FIG. 47: Tentative timeline for experiments after the 2012 shutdown. The 15 Hz upgraded Booster can meet the needs of MicroBooNE, Muon $g-2$, and Mu2e with 2 year runs for each experiment.

C. Cost Overview

The costs for the $g-2$ have been heavily scrutinized over the last year and are comparatively well-understood with respect to a typical pre-CD0 experiment. All costs have been assessed using standard laboratory practices and fully-loaded labor rates. The collaboration submitted an initial estimated Total Project Cost (TPC) of \$34.3M to the March 2009 Fermilab PAC. This was broadly divided into 3 categories: general accelerator upgrades (\$10.7M), $g-2$ specific DOE costs (\$19.8M), and NSF/international contributions (\$3.8M). The costs were assessed based on a preliminary civil construction assessment from Facility Engineering Services Section (FESS) at Fermilab, consultation with Brookhaven engineers and shipping companies, recommendations from Fermilab experts with considerable experience in accelerator projects, and other cost analysis performed by the collaboration. An independent review panel was formed within the lab to provide a second evaluation of all associated costs. The results of the review were reported to the directorate during the summer of 2009 with a substantially higher TPC of \$55.3M. The primary differences were due to assessing costs associated with project management (+\$3M), a new evaluation of the building costs from FESS (+\$4-8M), extra contingency added to accelerator improvements (+\$10M), added detector system contingency (+\$2M), and a few extra items added by the collaboration since the proposal (+\$2M). Due to the large uncertainties in the FESS civil estimates and the contingencies associated with accelerator improvements, in the latter half of 2009 additional resources were devoted by the laboratory to develop a more full understanding of the costs. With a large amount of work from FESS engineers and accelerator physicists at

Category	Cost	Contingency	Non-DOE	DOE
Building & Tunnel Connection	5240	25%		6550
Accelerator Upgrades	6876	36%		9317
$g-2$ Experiment	17208	48%	5786	19669
Totals	29324	41%	5786	35536

TABLE XV: Cost breakdown of the \$41.3M TPC. Costs have been divided into three categories: accelerator upgrades, civil construction of a new building and connecting beamline tunnel, and $g-2$ specific experimental costs. DOE HEP costs have been separated from other sources of funding that include the support of university groups by other agencies, D&D funding pledged by Brookhaven, and international contributions. It should be noted that the DOE cost of \$35.5M includes a duplication of \$5M present in the approved Mu2e experimental proposal, thus the total incremental cost to DOE HEP to add $g-2$ to the program is \$31M.

the lab, a final TPC of \$41.3M was established and the collaboration and the independent review committee agree to better than 10%, well within the stated contingencies.

The costs can broadly be defined in three categories: general upgrades to the accelerator complex, civil construction of a new building with a short tunnel connection to the existing P1 tunnel, and experimental costs specific to $g-2$. This categorization is useful for separating items specifically needed by $g-2$ from items that can be considered more general laboratory improvements. The cost breakdown in these categories is given in Table XV. The costs have also been subdivided by funding source, with DOE HEP costs separated from others. Average contingencies for each category are shown. The relatively small 25% contingency of the building and tunnel connections are a reflection of the detailed work performed by FESS engineers in developing an initial Project Definition Report (PDR) with a total cost of \$6.5M. A space waiver to allow a new building to be constructed has already been requested and granted by the DOE. The result of the PDR is a high-quality experimental hall in a very desirable location at the laboratory with a 30-ton overhead crane, a 70' x 80' footprint, and a connection bringing a secondary muon beam to the surface.

The accelerator upgrades listed in Table XV include moving an RF system from the Main Injector to the Recycler to allow Booster bunches to be subdivided, development and construction of a kicker to extract protons from the Recycler to the P1 transfer, building

a connecting line between the Recycler and the P1 line, and controlling losses in the P1 line when transporting a high-intensity 8 GeV proton beam. The last two elements are common to the Mu2e experiment. A nearly identical proton kicker is also needed by the Mu2e experiment to be installed in the Debuncher, so the development costs are beneficial to both experiments. The overall contingency for all four accelerator upgrades is 35% with a total cost of $9.3M.

The final category in Table XV includes all items specific to the $g-2$ experiment at Fermilab. The costs to DOE HEP have been separated from other funding sources. A total of $5.8M is expected to be funded through the support of university groups by other agencies and international contributions, and also includes a pledge of $1M from BNL D&D funds to begin decommissioning the storage ring. The DOE HEP portion totals $19.7M and includes moving the storage ring, rebuilding the experiment at FNAL, project management, and $g-2$ specific accelerator modifications. The average contingency is still somewhat conservatively set at 41% and is expected to come down as design work progresses.

1. Costing details

A more detailed description of the costs associated with various components of the project is provided in Table XVI. A description of each task is given in the list below.

- **g−2 conventional facilities:** Includes the cost for constructing a new building to house the storage ring and a short tunnel connecting the P1 beamline to the new building. The building has a 70' x 80' footprint high bay, 30-ton overhead crane, temperature control to ±2°F, and a floor stabilized by 4' caissons to support the 600 tons of magnet steel. An attached counting house and utility room are also included. The cost estimate is taken from a detailed initial PDR produced by FESS.

- **Recycler RF:** Installation of an RF system in the Recycler that is currently use for Tevatron operations in the Main Injector. Enables the Recycler to further subdivide bunches taken from the Booster. Costing performed by FNAL accelerator experts.

- **Recycler extraction kicker:** R&D and construction of a pulsed kicker to extract 8 GeV proton bunches from the Recycler. A similar system is required by the Mu2e

Building & Tunnel Connection	**Cost**	**Cont.**	**Total**
$g-2$ conventional facilities	5240	25%	6550
Total	**5240**	**25%**	**6550**
Accelerator Upgrades	**Cost**	**Cont.**	**Total**
Recycler RF	3022	17%	3536
Recycler extraction kicker	711	50%	1066
Recycler to P1 transfer*	2043	50%	3065
Prepare P1/P2/AP1 lines*	850	50%	1275
Open Debuncher aperture*	250	50%	375
Total	**6876**	**36%**	**9317**
g−2 Experiment (DOE-HEP)	**Cost**	**Cont.**	**Total**
New replacement target	43	50%	64
Li lens (costed) or 2 rad-hard quads	733	50%	1100
PMAG (pulsed or DC rad hard)	425	50%	638
Quads in AP2	400	75%	700
Debuncher, AP3 & Beamline stub	1050	75%	1838
Radiological issues	67	50%	100
Diagnostics	300	50%	450
Moving ring ($1M also in D&D)	2209	75%	3865
Recon ring & maintenance	3000	50%	4500
Cryo for $g-2$ experiment	1270	50%	1905
Inflector installation	504	19%	600
Kicker modification	570	42%	809
Fermilab straw detectors	385	30%	500
Project management	2000	30%	2600
Total	**12956**	**52%**	**19669**
g−2 Experiment (Other)	**Cost**	**Cont.**	**Total**
Detector/electronics/straws/DAQ	3066	30%	3986
Inflector	462	30%	600
Field probes	154	30%	200
Moving ring (BNL D&D)	571	75%	1000
Total	**4253**	**36%**	**5786**

TABLE XVI: Details of the cost estimate (all monetary units in $k). Description of each item and the corresponding cost analysis are presented in the text. *Items that are also required for the approved Mu2e Experiment.

experiment, so that R&D expense can be shared. Costing performed by FNAL accelerator experts.

- **Recycler to P1 transfer:** A connection between the Recycler and the P1 beamline needs to be established. Cost of the transfer line is adopted from the NOvA project where a similar transfer line is being built for injection into the Recycler from the Booster.

- **Prepare P1/P2/AP1 lines:** Currently the transmission efficiency of these beamlines is about 90% and will need to be improved in order to transport a higher-intensity proton beam. Also needed for the Mu2e experiment. Costing performed by FNAL accelerator experts.

- **Open Debuncher aperture:** In order to match the acceptance of the storage ring for the secondary muon beam, limiting apertures from cooling systems in the Debuncher need to be removed. This is also needed by the Mu2e experiment in order to limit losses from circulating the primary 8 GeV proton beam in the Debuncher. Costing performed by FNAL accelerator experts.

- **Li lens or 2 rad-hard quads:** The amount costed assumes that the current Li lens focussing system will have to be tested and modified to accommodate the lower-energy but higher repetition rate needed by $g-2$. A less expensive option of using two radiation hard quadrupoles, similar to the focus used at BNL, is still under study. Costing performed by pbar target experts.

- **New replacement target:** In the event that the Tevatron II run ends with no spare Li lens targets, a replacement target will need to be produced. Becomes irrelevant if radiation hard quadrupole solution is deployed. Cost well-established from Tevatron experience.

- **PMAG:** Currently the target area uses a radiation hard single turn magnet to bend the beam out of the target area. Effort is needed to understand whether the existing magnet can be pulsed at a higher rate or can just be run in a DC mode. A cheaper alternative for a more conventional, several turn, radiation-hard DC magnet is being explored. Costing performed by pbar target experts.

- **Quads in AP2:** Need 30 magnets installed with two additional power supplies. Costing based on typical installation costs. A large contingency of 75% has been assigned to cover uncertainties in installation difficulties.

- **Debuncher, AP3, & Beamline Stub:** Need a total of 65 magnets installed with four additional power supplies added. A large contingency of 75% has been assigned to cover uncertainties in installation difficulties.

- **Radiological Issues:** The muon beam in the experimental hall is not a high radiation area but will still require some monitoring and an interlock system to the high-bay area.

- **Diagnostics:** Instrumentation of the beamline with SWICs and other diagnostics.

- **Moving ring:** Costs based on quotes from shipping and skycrane companies, along with consultation with Brookhaven engineers and technicians.

- **Recon ring & maintenance:** A detailed reconstruction plans has been developed with Brookhaven engineers and technicians. Labor is based on original WBS documentation from the BNL assembly updated for modern labor costs.

- **Cryo for g−2 experiment:** Assumes cryogenic needs of the storage ring will be met using existing Tevatron systems. Detailed quote from FNAL cryogenic engineers.

- **Inflector installation:** Additional expenses to install inflector and connect to cryo system not part of the previous line item.

- **Kicker modification:** Kickers within the storage ring need to be modified to produce a higher amplitude, shorter duration pulse. Cost estimate assumes a test stand where a design is tested with half-length kicker electrodes, and the construction of additional kickers.

- **Fermilab straw detectors:** Development and construction of in-vacuum straw detectors at Fermilab. Provides for monitoring of the decay electrons from the stored muons and a measurement of the muon EDM. R&D beneficial to Mu2e where a similar system using longer straws is envisioned.

- **Project management:** Costs based on the Minerva and MicroBooNE current project management costs.

- **Detectors/electronics/straws/DAQ** Costs based on prototype calorimeters already assembled and tested at the Mtest facility. Also includes estimations from university groups for electronics and DAQ needs.

- **Inflector:** Design and construction of an open-ended inflector to allow better beam transport into the storage ring. Cost based on quote from Japanese group responsible for construction of original inflector.

- **Field probes:** Refurbishment of NMR probes used in the field measurements. Costs obtained from collaborators responsible for the BNL NMR system, now at KVI.

2. Fiscal year outlay

The funding profile required for the experiment to be ready for data in 2014 is shown in Figure 48, and has been created based on projecting the various components of the timeline shown in Figure 46. The costs in FY2010 are modest and are centered around early R&D efforts that were previously discussed in Section X B. In FY2011 the costs start to ramp up as FESS has requested $1.5M to finalize engineering designs and procure long lead-time items. Also in FY2011, several R&D efforts continue and the ring starts to be disassembled. FY2012 is the peak in the funding profile for several reasons. That is the year in which the accelerator complex is shutdown and it is most convenient to perform the accelerator upgrades needed in the Main Injector tunnel. In order to maintain the critical path, it is also the year in which the building and tunnel are constructed, the storage ring and subsystems are completely disassembled and shipped, and ring assembly begins. Throughout the following two years, FY2013 and FY2014, the ring is reassembled, cryogenic connections are made, and subsystems are completed and installed. Where possible, line items have been shifted into these years to reduce the fiscal burden in the more immediate years.

It is useful to consider how the fiscal year outlay in Figure 48 would be affected by a delay in the funding scenario. A delay in funding would result in the critical path shown in Figure 46 slipping. The red and blue profiles in Figure 48 could be extended with the

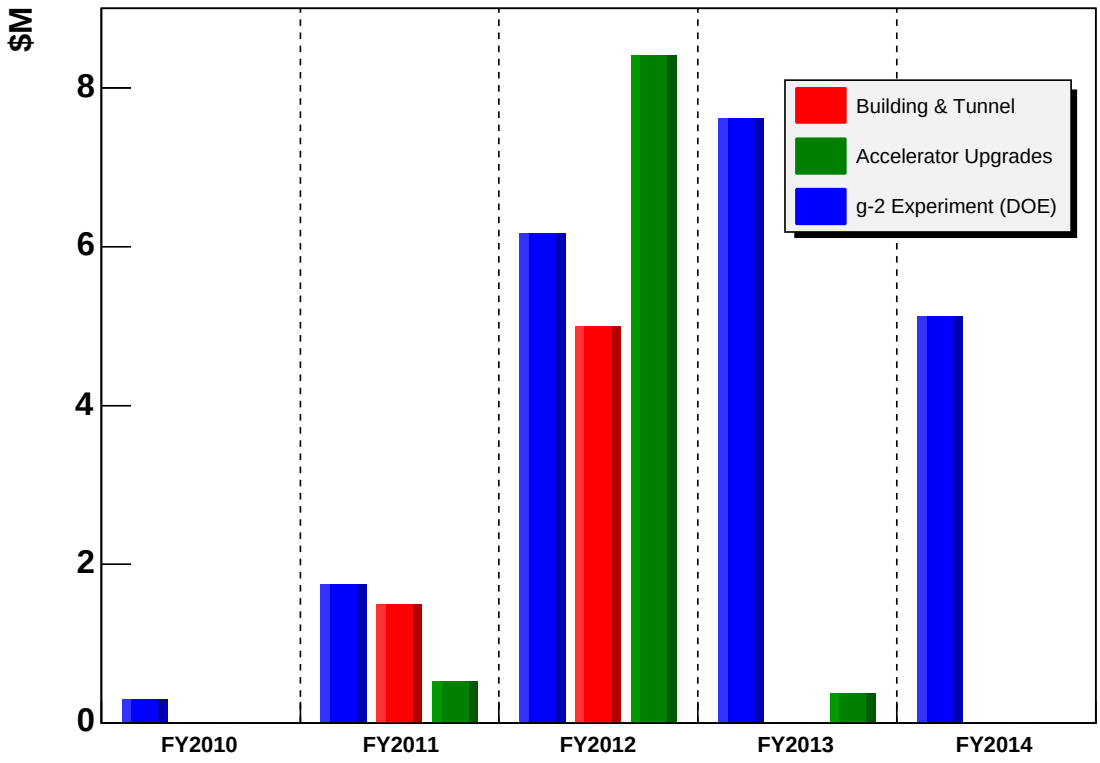

FIG. 48: Expenditures by fiscal year required for the experiment to be ready for data acquisition at the end of 2014. Expenditures have been divided into similar categories as presented in Tables XV and XVI. The \$1M in D&D pledged from BNL is included in the blue profile. Funding profiles for $g-2$ sources from agencies in support of university groups and international contributions are not shown.

main drawback being a delay in the first physics results by a commensurate amount. It is also the case that a delay in $g-2$ could create more of an overlap with Mu2e startup, however, any delay in $g-2$ due to funding constraints is likely to create the same delay in the Mu2e schedule. A delay in the accelerator upgrades (shown in green) results in a different complication. Most of these upgrades require access to the Main Injector tunnel and would be most conveniently performed during the long shutdown schedule in 2012 for NOvA upgrades. Performing the upgrades later would require an additional shutdown.

XI. SUMMARY OF THE REQUEST

We propose to improve the current measurement of the muon anomalous magnetic moment a_μ by a factor of 4. Combined with expected progress on the theoretical value, a 0.14 ppm result will nearly triple the sensitivity of the measurement to standard model extensions. The present suggestion from the final E821 result of a standard model violation may be contradicted, or verified, but whether the new result agrees with the standard model or not, it will place important constraints on candidate models of new physics—especially in the context of eagerly anticipated results from the LHC.

In this proposal, we have identified a timely and cost-effective method of using the Fermilab beam complex in the post-Tevatron era to produce custom, high-intensity bunches of muons that can be injected into the existing superconducting storage ring. While a major task will be the relocation of the ring from Brookhaven to Fermilab, it is work carrying relatively low risk. The proposed experiment builds on the considerable expertise developed over more than 20 years in the design, construction, data taking and analysis efforts from E821. The collaboration has been re-invigorated with many strong new groups who will work in concert with experts from the previous measurement. The physics motivation is compelling and promises to continue to provide unique insight into fundamental questions in high-energy physics.

[1] James P. Miller, Eduardo de Rafael and B. Lee Roberts, Rept. Prog. Phys. **70**, 795-881, 2007.

[2] A. Höcker and W.J. Marciano, Particle Data Group, Review *THE MUON ANOMALOUS MAGNETIC MOMENT* Updated July 2009, http://pdg.lbl.gov/

[3] M. Davier, et al., Eur. Phys. J. C (2010) 66: 127136.

[4] M. Davier, A. Hoecker, B. Malaescu, C.Z. Yuan, Z. Zhang, Eur. Phys. J. C66 1-9, (2010).

[5] CMD2 Collaboration, V. M. Aulchenko et al., JETP Lett. 82, 743 (2005); CMD2 Collaboration, R. R. Akhmetshin et al., JETP Lett. 84, 413 (2006); CMD2 Collaboration, R.R. Akhmetshin et al., Phys. Lett. B 648, 28 (2007).

[6] SND Collaboration, M. N. Achasov et al., JETP Lett. 103, 380 (2006).

[7] KLOE Collaboration, F. Ambrosino et al., Phys. Lett. B 670 285 (2009).

[8] BABAR Collaboration, B. Aubert et al., Phys. Rev. Lett. 103:231801 (2009).

[9] See, for example, R. Lafaye, T. Plehn, M. Rauch, D. Zerwa, arXiv:0709.3985; and, P. Bechtle, K. Desch, M. Uhlenbrock, P. Wienemann, arXiv:0907.2589.

[10] Joaquim Prades, Eduardo de Rafael and Arkady Vainshtein, *Hadronic Light-by-Light Scattering Contribution to the Muon Anomalous Magnetic Moment*, in Adv. Series on Direcction in High Energy Physics Vol 20, p. 303-318, World Scientific, 2009 "Lepton Dipole Moments", B.L. Roberts, W.J. Marciano (eds); and arXiv:0901.0306v1 [hep-ph]

[11] G.W. Bennett, et al., (Muon $(g-2)$ Collaboration), Phys. Rev. D **73**, 072003 (2006).

[12] CODATA recommended values of the fundamental physical constants: see update of μ_μ/μ_p in physics.nist.gov/cuu/Constants/index.html.

[13] W. Liu *et al*, Phys. Rev. Lett. **82**, 711 (1999).

[14] R. McNabb *et al*, Nucl. Inst. Meth., **602**,Issue 2, 396-402 (2009).

[15] G.W. Bennett *et al.* (Muon (g-2) Collaboration), Phys. Rev. D80, 052008 (2009).

[16] J. Schwinger, Phys. Rev. **73**, 416 (1948).

[17] Eduardo de Rafael *Present Status of the Muon Anomalous Magnetic Moment*; To appear in the proceedings of 14th High-Energy Physics International Conference in Quantum Chromodynamics (QCD 08), Montpellier, France, 7-12 Jul 2008. e-Print: arXiv:0809.3085.

[18] G. Charpak, F.J.M. Farley, R.L. Garwin, T. Muller, J.C. Sens, and A. Zichichi, Phys. Lett.

1, 16 (1962).

[19] J. Bailey et al., Nuovo Cimento **A9**, 369 (1972).

[20] J. Aldins, S.J. Brodsky, A.J. Dufner and T. Kinoshita, Phys. Rev. D **1**, 2378 (1970).

[21] J. Bailey et al., Nucl. Phys. **B150**, 1 (1979).

[22] The $g-2$ Collaboration: R.M. Carey et al., Phys. Rev. Lett. **82**, 1632 (1999).

[23] The $g-2$ Collaboration: H.N. Brown et al., Phys. Rev. D **62**, 091101 (2000).

[24] The $g-2$ Collaboration: H.N. Brown et al., Phys. Rev. Lett. **86**, 2227 (2001).

[25] The $g-2$ Collaboration: G.W. Bennett et al., Phys. Rev. Lett. **89**, 101804 (2002); Erratum-ibid. **89**, 129903 (2002).

[26] The $g-2$ Collaboration: G.W. Bennett et al., Phys. Rev. Lett. **92**, 161802 (2004).

[27] K. Hagiwara *et al*, Phys. Rev. **D66**, 010001 (2002).

[28] T. Kinoshita and M. Nio, *Phys. Rev. D* **73**, 053007 (2006).

[29] T. Aoyama, M. Hayakawa, T. Kinoshita, M. Nio, and N. Watanabe, *Phys. Rev. D* **78**, 053005 (2008).

[30] D. Hanneke, S. Fogwell and G. Gabrielse, Phys. Rev. Lett. 100, 120801 (2008).

[31] T. Kinoshita, in *Lepton Dipole Moments*, ed. B. Lee Roberts and William J. Marciano, Advanced Series on Directions in High Energy Physics, Vol. 20, World Scientific, 2010 p. 69.

[32] A. Czarnecki, B. Krause and W.J. Marciano, Phys. Rev. Lett. **76** (1996) 3267.

[33] S. Peris, M. Perrottet and E. de Rafael, Phys. Lett. **B355** (1995) 523.

[34] A. Czarnecki, B. Krause and W. Marciano, Phys. Rev. **D52** (1995) R2619.

[35] A. Czarnecki, W.J. Marciano and A. Vainshtein, Phys. Rev. **D67** (2003) 073006. A. Czarnecki, W.J. Marciano and A. Vainshtein, Phys. Rev. **D67** (2003) 073006.

[36] Andzrej Czarnecki and William J. Marciano in *Lepton Dipole Moments*, ed. B. Lee Roberts and William J. Marciano, Advanced Series on Directions in High Energy Physics, Vol. 20, World Scientific, 2010 p. 11 and references therin.

[37] http://tau08.inp.nsk.su/

[38] http://www.hep.manchester.ac.uk/TAU2010

[39] http://bes.ihep.ac.cn/conference/phispi09

[40] Thomas Teubner, International Workshop on e+e- collisions from Phi to Psi, Frascati, Nuclear Physics B (Proc. Suppl.) **181182**, 20 (2008).

[41] J. Prades, E. de Rafael and A. Vainshtein in *Lepton Dipole Moments*,ed. B. Lee Roberts and

William J. Marciano, Advanced Series on Directions in High Energy Physics, Vol. 20, World Scientific, 2010 p. 303 and references therein.

[42] Eduardo de Rafael, private communication, 2010.

[43] G. Amelino-Camelia, et al., (KLOE-2 Collaboration) arXiv:1003.3868v1 [hep-ex] March 2010.

[44] Graziano Venanzoni, private communication, March 2010.

[45] Michel Davier, private communication (2009).

[46] M. Passera, W.J. Marciano and A. Sirlin, PHIPSI2009, Beijing 2009, arXiv:1001.4528 [hep-ph] Jan. 2010.

[47] F. Jegerlehner, http://www.lnf.infn.it/conference/phipsi08/ International Workshop on e+e- collisions from Phi to Psi, Frascati, 7-10 April, 2008, and Nuclear Physics B (Proc. Suppl.) **181182**, 26 (2008).

[48] M. Passera, W.J. Marciano and A. Sirlin, Phys. Rev. **D 78**, 013009 (2008).

[49] S. Binner, J.H. Kühn and K. Melnikov, Phys. Lett. **B 459**, 279 (1999).

[50] S. Actis, et al., (Working Group on Radiative Corrections and Monte Carlo Generators for Low Energies), arXiv0912.0749, Dec. 2009, submitted to Eur. Phys. J. **C**.

[51] K. Hagiwara, A.D. Martin, D. Nomura and T. Teubner, Phys. Lett. **B649** 173 (2007).

[52] M. Davier, hep-ph/0701163v2, Jan. 2007.

[53] F. Jegerlehner, Acta Phys. Polon. B **38**, 3021 (2007) [arXiv:hep-ph/0703125].

[54] Zhiqing Zhang, Muon $g-2$: a mini review, arXiv:0801.4905v1 [hep-ph], Jan. 2008.

[55] KLOE collaboration (F. Ambrosino et al.), Phys. Lett. **B669**, 223-228 (2008).

[56] M. Davier, TAU'08, Novosibirsk, 22-25 September 2008.

[57] R. Alemany, M. Davier and A. Höcker, Eur.Phys.J. **C2** 123 (1998).

[58] M. Davier and A. Höcker, Phys. Lett.**B435**, 427 (1998).

[59] M. Davier, S. Eidelman, A. Höcker, and Z. Zhang, Eur. Phys J. **C 27** 497 (2003). See K. Hagiwara, A.D. Martin, D. Nomura, and T. Teubner Phys. Lett. **B557**, 69 (2003) for an independent analysis of the e^+e^- data.

[60] Arkady Vainshtein, private communication.

[61] Topical Workshop on The Muon Magnetic Dipole Moment; Oct. 2007 School of Physics and Astronomy, The University of Glasgow. See: www.ippp.dur.ac.uk/old/MuonMDM/.

[62] T. Blum, Phys. Rev. Lett. **91**, 052001-1 (2003).

[63] T. Blum, Nucl. Phys. Proc. Suppl. **129**, 904-906,2004, and arXiv hep-lat/0310064,

[64] T. Blum, private communication, February 2009.

[65] T. Kinoshita and W.J. Marciano in *Quantum Electrodynamics* (Directions in High Energy Physics, Vol. 7), ed. T. Kinoshita, (World Scientific, Singapore, 1990), p. 419.

[66] F. Ambrosino et al., (KLOE Collaboration), Phys. Lett. **B670**, 285 (2009).

[67] S. Müller for the KLOE Collaboration, PHIPSI2009, Beijing 2009

[68] G. Amelino-Camelia, et al., (KLOE2 Collaboration), arXiv:1003.3868v1 [hep-ex] March 2010.

[69] M. Davier, A. Höcker, B. Malaescu, C.Z. Yuan and Z. Zhang, arXiv:0908.4300v2 [hep-ph] Feb. 2010.

[70] M. Davier, A. Höcker, G. López Castro, B. Malaescu, X.H. Mo, G. Toledo Sánchez, P. Wang, C.Z. Yuan and Z. Zhang, arXiv0906.5443v3 [hep-ph] Dec. 2009.

[71] Andrzej Czarnecki and William J. Marciano, Phys. Rev. **D64** 013014 (2001).

[72] M. Davier and W.J. Marciano, Ann. Rf. Nucl. Part. Phys. **54**, 115 (2004).

[73] The articles listed in the SPIRES citations to Ref. [24] contain many different models beyond the standard model.

[74] E. Eichten, et al., Phys. Rev. Lett. **45**, 225 (1980), K. Lane, arXiv hep-ph/0102131, 2001.

[75] T. Appelquist and B. A. Dobrescu, "Universal extra dimensions and the muon magnetic moment," Phys. Lett. B **516** (2001) 85 [arXiv:hep-ph/0106140].

[76] M. Blanke, A. J. Buras, B. Duling, A. Poschenrieder and C. Tarantino, JHEP **0705** (2007) 013 [arXiv:hep-ph/0702136].

[77] Friedrich Jegerlehner, The Anomalous Magnetic Moment of the Muon, Springer Tracts in Modern Physics Vol. 226.

[78] H. Davoudiasl, J. L. Hewett and T. G. Rizzo, Phys. Lett. B **493** (2000) 135 [arXiv:hep-ph/0006097].

[79] S. C. Park and H. S. Song, Phys. Lett. B **506** (2001) 99 [arXiv:hep-ph/0103072].

[80] C. S. Kim, J. D. Kim and J. H. Song, Phys. Lett. B **511** (2001) 251 [arXiv:hep-ph/0103127].

[81] M. L. Graesser, Phys. Rev. D **61** (2000) 074019 [arXiv:hep-ph/9902310].

[82] K. Cheung, W. Y. Keung and T. C. Yuan, Phys. Rev. Lett. **99** (2007) 051803 [arXiv:0704.2588 [hep-ph]].

[83] J. A. Conley and J. S. Gainer, arXiv:0811.4168 [hep-ph].

[84] D. McKeen, arXiv:0912.1076 [hep-ph].

[85] C. M. Ho and T. W. Kephart, arXiv:1001.3696 [hep-ph].

[86] T. Hambye, K. Kannike, E. Ma and M. Raidal, Phys. Rev. D **75** (2007) 095003 [arXiv:hep-ph/0609228].

[87] E. O. Iltan, arXiv:0901.0544 [hep-ph].

[88] M. Pospelov, Phys. Rev. D **80** (2009) 095002 [arXiv:0811.1030 [hep-ph]].

[89] R. Essig, P. Schuster and N. Toro, Phys. Rev. D **80** (2009) 015003 [arXiv:0903.3941 [hep-ph]].

[90] D. W. Hertzog, J. P. Miller, E. de Rafael, B. Lee Roberts and D. Stöckinger, arXiv:0705.4617 [hep-ph].

[91] J. M. Smillie and B. R. Webber, JHEP **0510** (2005) 069 [arXiv:hep-ph/0507170].

[92] B. C. Allanach *et al.*, *Proc. of the APS/DPF/DPB Summer Study on the Future of Particle Physics (Snowmass 2001)* ed. N. Graf, Eur. Phys. J. C **25** (2002) 113 [eConf **C010630** (2001) P125].

[93] R. Ruiz de Austri, R. Trotta and L. Roszkowski, JHEP **0605** (2006) 002 [arXiv:hep-ph/0602028]; JHEP **0704** (2007) 084 [arXiv:hep-ph/0611173]; JHEP **0707** (2007) 075 [arXiv:0705.2012]; B. C. Allanach, C. G. Lester and A. M. Weber, JHEP **0612** (2006) 065; B. C. Allanach, K. Cranmer, C. G. Lester and A. M. Weber, JHEP **0708**, 023 (2007); J. R. Ellis, S. Heinemeyer, K. A. Olive, A. M. Weber and G. Weiglein, JHEP **0708** (2007) 083; S. Heinemeyer, X. Miao, S. Su and G. Weiglein, JHEP **0808**, 087 (2008).

[94] J. R. Ellis, K. A. Olive, Y. Santoso and V. C. Spanos, Phys. Lett. **B 565** 176 (2003); John Ellis, Keith A. Olive, Yudi Santoso, and Vassilis C. Spanos, Phys. Rev. **D71** 095007 (2005), and references therein.

[95] N. Arkani-Hamed, G. L. Kane, J. Thaler and L. T. Wang, JHEP **0608**, 070 (2006) [arXiv:hep-ph/0512190].

[96] R. Lafaye, T. Plehn, M. Rauch and D. Zerwas, arXiv:0709.3985 [hep-ph].

[97] C. F. Berger, J. S. Gainer, J. L. Hewett, B. Lillie and T. G. Rizzo, arXiv:0712.2965 [hep-ph].

[98] M. Alexander, S. Kreiss, R. Lafaye, T. Plehn, M. Rauch, and D. Zerwas, Chapter 9 in M. M. Nojiri *et al.*, arXiv:0802.3672 [hep-ph].

[99] G. Ross and M. Serna, arXiv:0704.1248 [hep-ph].

[100] S. P. Martin and J. D. Wells, Phys. Rev. D **67**, 015002 (2003) [arXiv:hep-ph/0209309].

[101] C. F. Berger, J. S. Gainer, J. L. Hewett and T. G. Rizzo, arXiv:0812.0980 [hep-ph].

[102] N.V. Mokhov, "The Mars Code System User's Guide", Fermilab-FN-628 (1995); N.V. Mokhov, S.I. Striganov, "MARS15 Overview", Fermilab-Conf-07/008-AD (2007), in Proc.

of Hadronic Shower Simulation Workshop, Fermilab, September 2006, AIP Conf. Proc. 896, pp. 50-60 (2007); http://www-ap.fnal.gov/MARS/

[103] For information about the Fermilab Proton Plan, see: `http://www-accel-proj.fnal.gov/Proton_Plan/index.shtml`.

[104] C. Bhat, J. MacLachlan, "RF Requirements for Bunching in the Recycler for Injection into the g-2 Ring,"Beams-doc-3192 (28 Aug 2008).

[105] Conventional

[106] J. Theilacker, Internal Memo, 21 Aug 2008.

[107] F. Krienen, D. Loomba and W. Meng, Nucl. Inst. and Meth. **A 283**, 5 (1989).

[108] A. Yamamoto, et al., Nucl. Instrum. and Methods Phys. Res. **A491** 23-40 (2002).

[109] G.T. Danby, et al., Nucl. Instr. and Methods Phys. Res. **A 457**, 151-174 (2001).

[110] E821 - Technical Design Report

[111] R. Prigl *et al*, Nucl. Instrum. Meth. **A374**, 118 (1996).

[112] R. Prigl, PhD Thesis, U. Heidelberg (1994).

[113] A.P. Grossmann, PhD Thesis, U. Heidelberg (1998).

[114] S.I. Redin, PhD Thesis, Yale University (1999).

[115] H. Deng, PhD Thesis, Yale University (2002).

[116] G. Danby *et al*, Nucl. Instrum. Meth. **A457**, 151 (2002).

[117] A. Yamamoto *et al*, Nucl. Instrum. Meth. **A491**, 23 (2002).

[118] E. Efstathiadis *et al*, Nucl. Instrum. Meth. **A496**, 8 (2003).

[119] X. Fei, V.W. Hughes, and R. Prigl, Nucl. Instrum. Meth. **A394**, 349 (1997).

[120] Superintendent of Documents, *LORAN-C User's Handbook*, U.S. Government Printing Office #050-012-00331-9, 1992.

[121] P.J. Mohr and B.N. Taylor, Rev. Mod. Phys. **72**, 351 (2000).

[122] S. I. Redin *et al.*, Nucl. Instrum. Meth. A **473**, 260 (2001).

[123] P. Neumayer, Diploma Thesis, U. Heidelberg (1999).

[124] Paul Scherrer Instutut Experiment R-99-07, *A Precision Measurement of the Positive Muon Lifetime using a Pulsed Muon Beam and the μLan Detector.*

[125] Paul Scherrer Instutut Experiment R-97-05, *Precision Measurement of Singlet μp Capture in Hydrogen.*

[126] D.W. Hertzog *et al.*, Nucl. Instrum. Methods Phys. Res. **A294**, 446 (1990).

[127] S.A. Sedykh *et al.*, Nucl. Inst. Methods Phys. Res. **A455** 346 (2000)

[128] J. Ouyang *et al.*, Nucl. Instrum. Methods Phys. Res. **A374**, 215 (1996).

[129] For example, see C. Fabjan, "Calorimetry in high-energy physics", Experimental Techniques in High-Energy Nuclear and Particle Physics, 2nd Ed., World Scientific Publishing Co., T. Ferbel, Ed., (1991), 257.

[130] M. Raidal *et al.*,Eur. Phys. J. C**57**, 13 (2008).

[131] P. Huet, E. Sather, Phys. Rev. D**51** 379 (1995).

[132] E.O. Iltan, Eur. Phys. J. C**54**, 583 (2008).

[133] M.J. Sossong, *A Search for an Electric Dipole Moment of the Positive Muon,* Univ. of Illinois (Urbana) thesis, UMI-31-13195 (2005).

[134] J. Bailey *et al.*, j. Phys. G**4**, 345 (1978).

[135] M. Sossong *et al.*, submitted to Nucl. Int. Meth. A

[136] C. Kendziora *et al.*, Fermilab-Pub-02-241-E, submitted to Nucl. Int. Meth. A

[137] J.L. Flowers, B.W. Petley, M.G. Richards, Metrologia **30** (1993) 75; K. Jackowski, M. Jaszunski, B. Kamienski, M. Wilczek, J. Magn. Reson. **193** (2008) 147.

[138] U. Rohrer, http://pc532.psi.ch/optics.htm

[139] V. Lebedev, http://www-bdnew.fnal.gov/pbar/organizationalchart/lebedev/OptiM/optim.htm

[140] Y.K. Semertzidis, Nucl. Instrum. Methods Phys. Res. **A503** 458-484 (2003)

[141] This section was adapted from Yuri F. Orlov and Yannis K. Semertzidis, Muon $g-2$ Note 431, January 21, 2003.

[142] This section was adapted from a preprint by I.A.Koop, A.V.Otboev, E.A.Perevedentsev, P.Yu.Shatunov and Yu.M.Shatunov of the Budker Institute for Nuclear Physics, Novosibirsk.

[143] L.D.Landau, E.M.Lifshitz, "Mechanics", Moscow "Nauka" (1988)

[144] A.N.Dubrovin, "MERMAID user guide", Novosibirsk (1994).

[145] E.A.Perevedentsev et al., Preprint BINP, Novosibirsk (1980)

[146] Saint-Gobain Crystals and Detectors, 12345 Kinsman Road, Newbury, OH 44065.

[147] Marketech International, 4750 Magnolia Street, Port Townsend, WA 98368.

[148] At Fermilab, the beam energy of the Booster is typically quoted as "8 GeV" and refers to the kinetic energy. The momentum per proton is 8.889 GeV/c.

[149] Other small uncertainties raise the cited total to 0.21 ppm. These additional errors are upper limits that will improve with increased statistics of the sample and thus will not change our

projections significantly.

APPENDIX A: REPORT FROM THE PAC AND LETTERS FROM THE DIRECTORATE

Fermilab

Fermi National Accelerator Laboratory
P.O.Box 500 • Batavia, Il.• 60510-0500
630-840-3211 FAX 630-840-2900

Director's Office

April 2, 2009

Prof. David Hertzog
Physics Department
University of Illinois
Urbana-Champaign IL 61801

Prof. Lee Roberts
Physics Department
Boston University
Boston MA 02215

Dear David and Lee,

Thank you for the proposal for a New (g-2) Experiment at Fermilab, which we have given the designation P-989, and the presentation at the recent Physics Advisory Committee (PAC) meeting. The PAC appreciated the value of making this "text-book measurement", and was impressed that the experiment could be done for a significantly lower cost than had been thought earlier. The PAC wrote:

The Committee considered the proposal to improve the high-precision measurement of the muon (g-2) by a factor of four to 0.14 ppm. The muon (g-2) experiments are highly significant due to the accurately calculated value predicted in the standard model (SM), and the sensitivity to a variety of new physics effects at high-mass scales which could result in a deviation from the SM prediction. Although the ultimate limit to the comparison with the SM expectation may be uncertainties in the theory (particularly the light-by-light contribution), the past work at BNL, a tour-de-force demonstration of experimental particle physics technique, was limited primarily by statistics to the 0.54 ppm level (with 0.46 ppm from statistics).

In the present proposal, the improvement in precision possible at Fermilab comes mainly from obtaining increased statistical precision due to improvements to the pion capture and transport aspects of the experiment. The versatile Fermilab beam complex would be used parasitically during high-energy neutrino production, and muons will be injected and stored in the muon storage ring relocated from BNL. Data would be acquired within two years of running. In addition, the collaboration proposes to make several substantial reductions in systematic uncertainties.

This is an opportune and excellent proposal which is well motivated and represents a technically sound incremental advance over previous work. Realizing the goal would result in an important step forward for fundamental physics measurements, which fits well with Fermilab's other future efforts in precision muon physics at the Intensity Frontier.

The Committee recommends that the opportunity presented by this relatively low-cost and high-quality project be pursued. It would be useful to perform an impact and technical evaluation to understand the implications for other aspects of the Fermilab program, and to validate the cost and schedule estimates, which are significantly reduced from what the Particle Physics Project Prioritization Panel (P5) considered. Also, it would be useful to develop mechanisms to draw upon the technical expertise developed at BNL over many years during the previous (g-2) experiment.

I am happy to have received this encouragement, and congratulate you and your collaborators on the interest in the possibility of a New (g-2) Experiment at Fermilab. We are forming a review committee to evaluate the cost estimate you presented and consider possible conflicts with other parts of the Fermilab program. I trust that we can call upon you and your collaborators to help in this process. We will be in touch about this in the near future.

Again, thank you for your pursuit of making this measurement at Fermilab.

Sincerely,

Piermaria Oddone

cc:
Y. Kim
P. Garbincius
S. Holmes
R. Kephart
G. Bock
J. Appel
R. Dixon
V. White
G. Apollinari
C. Hogan
V. Shiltsev
L. Bauerdick
S. Dawson
M. Procario
J. Whitmore
D. Lissauer
D. Levy
F. Bernthal

Fermilab

Fermi National Accelerator Laboratory
P.O.Box 500 • Batavia, Il.• 60510-0500
630-840-3211 FAX 630-840-2900

Director's Office

December 1, 2009

Prof. David Hertzog
Physics Department
University of Illinois
Urbana-Champaign IL 61801

Prof. Lee Roberts
Physics Department
Boston University
Boston MA 02215

Dear David and Lee,

Thank you for the update on the proposal for a New (g-2) Experiment at Fermilab (P-989). I also thank Lee for his presentation at the recent Physics Advisory Committee (PAC) meeting. The PAC continues to appreciate the value of this "text-book measurement", and was impressed by the work done to better understand and, where possible, lower the cost of the experiment. In response to my charge, the PAC wrote the attached comments and advice.

I am happy to have received this continuing encouragement from the PAC, and will work with the DOE on the possibility of a New (g-2) Experiment at Fermilab. In the meantime, as recommended by the PAC, you should explore the possibilities for even wider international participation, and the financial and in-kind support of the experiment that should come with the interest in making this measurement. We should stay in touch about our contacts as the possibilities develop.

Again, thank you for your pursuit of making this measurement at Fermilab.

Sincerely,

Piermaria Oddone

cc:
Y. Kim
S. Holmes
R. Kephart
G. Bock
J. Appel
R. Dixon
V. White
G. Apollinari
M. Lindgren
C. Hogan
V. Shiltsev
L. Bauerdick
R. Van Kooten
M. Procario
J. Whitmore
D. Lissauer
D. Levy
F. Bernthal

Excerpt from Physics Advisory Committee Comments and Recommenations, November 2009

P-989 Design and Cost Update for New g-2 (Hertzog/Roberts)

The New g-2 Collaboration reviewed its proposal for an improved measurement of g-2 of the muon, with considerable cost-savings obtained by moving the E821 storage ring from BNL to Fermilab. It would use the beam from the Booster before the start of the Mu2e experiment and following the 15-Hz upgrade in a way so as not to interfere with any other efforts of the pre-Project-X program. The proponents presented updates on the current theoretical understanding and a revised cost estimate.

As stated by the HEPAP Particle Physics Project Prioritization Panel (P5) in its 2007 report, "there is an excellent physics case for this classic experiment." However, the g-2 experiment was given a relatively low priority by P5. Since the report, several things have changed. The cost is now significantly less than thought at that time. Also, the P5 report noted that the g-2 experiment could be pursued at JPARC in Japan with only a modest investment from the US. For technical reasons, that particular option is no longer present, and it appears that the experiment won't be done in the foreseeable future if it isn't done at Fermilab. This presents a window of opportunity. There are no other competing experiments in the same time frame. Making the measurement at JPARC using ultra-cold muons is under consideration, but it is only in a very preliminary conceptual design phase. P-989 offers the possibility for a continued leadership role on g-2 in the US, and the Japanese g-2 community has joined the Fermilab proposal. The timing of the new g-2 experiment fits well with the Fermilab program, and offers the possibility for near-term physics results after the end of the Collider program.

There have been significant advances in the theoretical understanding of g-2, although the uncertainty on the light-by-light contribution remains a worry. There is a worldwide effort to reduce the theoretical uncertainty from hadronic contributions. The addition of new experimental input of the measured low-mass hadronic spectrum provides an improved theoretical prediction. Further measurements from Frascati, Novosibirsk, BEPC, and the *B* factories are promising, including a potential low-mass two-photon mass spectrum measurement. The Collaboration expects to achieve a four-fold decrease in the total g-2 measurement uncertainty, and a 5-sigma measurement (for the same central value and no further improvements in the precision of the theoretical prediction). Well-motivated improvements in detector systems should allow for further reduction in experimental systematic uncertainties, and may allow the measurement of the electric dipole moment (EDM) of the muon in a first phase of such a program. The physics interest in the g-2 result is strong, as witnessed by the large number of recent citations of the BNL g-2 results. Almost any model of new physics will result in a contribution to g-2 and a deviation from the Standard Model prediction.

P-989 is being proposed by a strong and experienced collaboration of highly competent physicists in this field, using a well-tested technique. A notable reinforcement of the effort is the securing of the promise from BNL of technical support with specialized experience with the E821 experiment. The Committee believes that the experiment could achieve the proposed sensitivity.

The Committee appreciates the excellent work involved in producing the detailed project cost estimates by the Collaboration and Fermilab. These project cost estimates are on a much firmer footing than previously.

The experiment meets the criteria for Stage I approval. However, the Laboratory currently has very limited available resources (both financial and human) to execute P-989. The proponents should be strongly encouraged to pursue commitments of substantial funding from non-DOE sources. The experiment would produce important physics and would be the start of a precision muon program at the Laboratory. There is the potential for the experiment to continue into the Project-X era, thereby increasing the diversity of the Project-X physics program. The Committee recommends that the Laboratory clarify with DOE the prospects for obtaining support for P-989.

APPENDIX B: MUON KICKER, ELECTRIC QUADRUPOLES AND BEAM DYNAMICS

1. Introduction: The Kicker and Quadrupoles

The incoming bunched beam from the AGS is kicked on orbit by a fast muon kicker consisting of three identical pulse-forming networks and kicker magnets [118]. The ring is a weak-focusing storage ring with electrostatic quadrupoles that provide the (weak) vertical focusing. Both the kicker and quadrupoles worked well enough in E821 to permit the 0.54 ppm measurement, but will need to be upgraded and re-furbished for the new experiment.

The geometry of the quadrupole high-voltage leads inside of the vacuum chamber must be re-configured to further reduce trapped electrons that lead to sparks. In addition, the lead configuration outside of the vacuum chamber where the high voltage feed-throughs are located also must be changed to make them more reliable. The quadrupole support structures inside of the vacuum chamber will need to be re-furbished, and the side insulators replaced, but all of these changes represent modest improvements and will not be discussed further in this proposal.

The fast muon kicker worked adequately during the running period of E821, but there are several maintenance items, and upgrades that are necessary. The repetition rate of 18 Hz in the Fermilab experiment is 4 times higher than was possible at BNL and will require modifications to the modulators to remove the additional heat. The AGS delivered a maximum of 12 proton bunches, with 33 ms between bunches, and a 2.7 s macro cycle time. The bunch spacing at Fermilab will be 11 ms between bunches, with 24 expected in a 1.33 s cycle. We expect to introduce cooling, and perhaps other modifications.

The measured absolute injection efficiency in E821 was lower than expected. Scans of the number of stored muons as a function of kicker high voltage did not plateau, indicating that a larger kick could store (perhaps significantly) more muons. We are examining the kicker pulse-forming network, to try to determine how to increase the peak current, and reduce the pulse-width, which should lead to a higher storage efficiency. While the rate calculations in this proposal do not assume any additional factor from the kicker, we are actively studying how to increase the number of stored muons per fill of the ring.

A detailed full Geant4 based simulation program has been developed at Boston University,

both to model the performance of the E821 kicker, and to determine what parameters could be improved to produce a more efficient kick. The simulation models the transporting of muons through the inflector, the kick, and the final storage of muons on orbit. All known nonuniformities in the storage and inflector magnetic fields are modeled. Additionally, the time dependence of the kicker and quadrupole fields are modeled. The program is now working, and is beginning to be used to answer physics questions.

2. Beam Dynamics in the Ring

The storage ring is a weak focusing ring, with the field index $n < 1.0$ determined by the strength of the electrostatic quadrupole field. In the limit of a continuous quadrupole field, the stored muons execute simple harmonic motion radially (x) and vertically (y) with the frequencies given by

$$f_y = f_C\sqrt{n} \simeq 0.37 f_C; \qquad f_x = f_C\sqrt{1-n} \simeq 0.929 f_C, \tag{B1}$$

where f_C is the cyclotron frequency, and the field index n is given by

$$n = \frac{\kappa R_0}{\beta B_0}\,. \tag{B2}$$

The numerical values are for $n = 0.137$. The frequencies in the ring are given in Table XVII.

Quantity	*Expression*	*Frequency*	*Period*
f_a	$\frac{e}{2\pi mc}a_\mu B$	0.23 MHz	4.37 μs
f_c	$\frac{v}{2\pi R_0}$	6.7 MHz	149 ns
f_x	$\sqrt{1-n}f_c$	6.23 MHz	160 ns
f_y	$\sqrt{n}f_c$	2.48 MHz	402 ns
$f_{\rm CBO}$	$f_c - f_x$	0.477 MHz	2.10 μs
$f_{\rm VW}$	$f_c - 2f_y$	1.74 MHz	0.574 μs

TABLE XVII: Frequencies in the $g-2$ ring. CBO = coherent betatron oscillation; VW =vertical waist; a, c refer to spin precession ω_a and cyclotron frequencies respectively.

The quadrupoles in the storage ring have four-fold symmetry as shown in Fig. 49. The

kicker region is indicated by K1-3, which are three identical sections, each driven by a separate pulse-forming network.

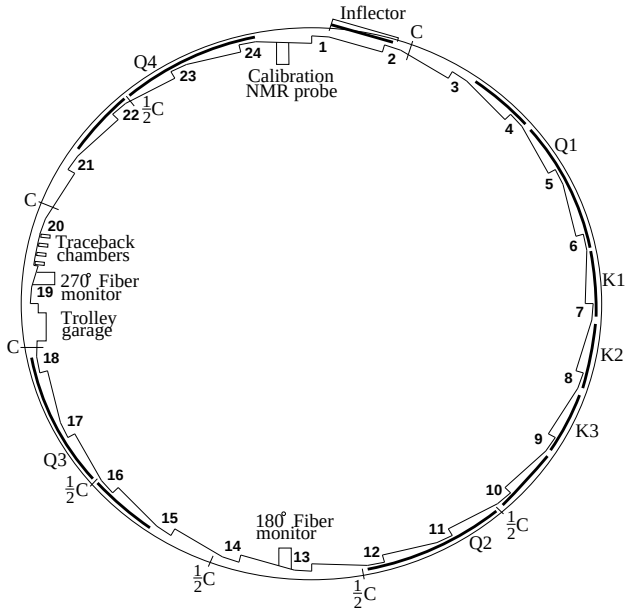

FIG. 49: The $(g-2)$ storage ring layout. The 24 numbers represent the locations of the calorimeters at the end of the scalloped vacuum chamber. The electrostatic quadrupoles have four-fold symmetry (Q1-Q4), and the kicker section consists of three identical sections, each 1.8 m long (K1-K3). Collimators are either full-aperture (C) or half-aperture ($\frac{1}{2}$C) collimators.

3. The Fast Muon Kicker

The E821 kicker, described in Ref. [118], makes use of a current pulse traveling along two parallel conductors with cross-overs at each end so that the current runs in opposite directions in the two plates. The 80-mm high kicker plates are 0.75-mm thick aluminum, electron-beam welded to aluminum rails at the top and bottom, which support the assembly and serve as rails for the 2-kg NMR trolley. The entire assembly is 94-mm high and 1760-mm long. This plate-rail assembly is supported on Macor insulators that are attached to Macor plates with plastic hardware forming a rigid cage, which is placed inside of the vacuum chamber. `OPERA` calculations indicated that aluminum would minimize the residual eddy currents following the kicker pulse, and measurements showed that the presence of this

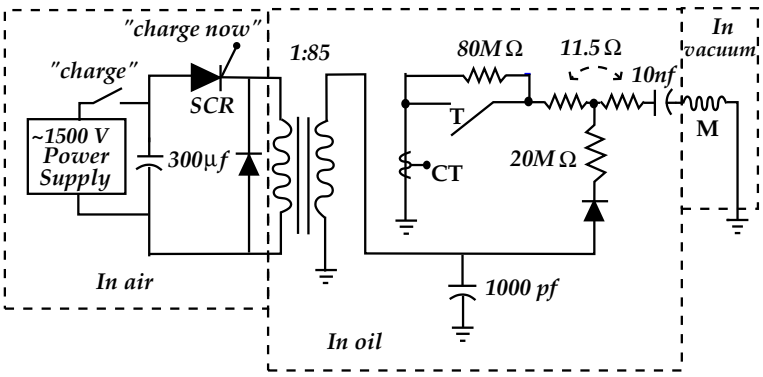

FIG. 50: The (Ideal) Circuit of the Kicker. Stray inductance and capacitance are not shown. The inductor labeled **M** represents the kicker magnet, **T** represents an English Electric Valve deuterium thyratron, **CT** is a current transformer which gives the current waveform.

aluminum assembly would have a negligible effect on the storage ring precision magnetic field.

The kicker circuit can be approximated as an underdamped LCR circuit as shown in Fig. 50. The current on the plates is of the form:

$$I(t) = I_0 e^{-\frac{\gamma}{2}t} \sin(2\pi f_d t + \phi_d) \tag{B3}$$

where

$$f_d = \frac{1}{2\pi}\left(\frac{1}{LC}\right)^{\frac{1}{2}}\left\{1 - \frac{R^2 C}{4L}\right\}^{\frac{1}{2}} = \frac{1}{2\pi}\sqrt{\frac{1}{LC} - \frac{R^2}{4L^2}}, \tag{B4}$$

and the width and peak current are given by

$$\gamma = \frac{R}{L} \qquad \text{and} \qquad I_0 = \frac{V_0}{2\pi f_d L}. \tag{B5}$$

The values of these parameters for the simple LCR circuit are given in Table XVIII. For critical damping, $R_{\text{Critical}} = 25.3\ \Omega$.

In each circuit, an initial voltage of ~ 90 kV on the capacitor results in a current-pulse amplitude of approximately 4200 A. Figure 51 shows the pulse from one of the networks superimposed on a schematic representation of the time and width of the muon bunch as it passes the location of a single kicker section. While a square-wave current pulse—bracketing the injected bunch and turning off completely before the next revolution—would be ideal, the actual pulse waveform acts both positively and negatively on the bunch during the first five turns in the ring. The injection efficiency is estimated to be $3 - 5$ percent.

TABLE XVIII: The values of the elements and some properties of the simple circuit. Note that the 1.6 μH inductance is the estimated inductance of the whole kicker circuit. τ_0 is the undamped period, τ_d is the damped period, and τ is the decay time of the waveform.

Quantity	*Value*	*Quantity*	*Value*
R	11.5 Ω	L	$\sim$ 1.6 μH
C	10 nF		
f_0	1.258×10^6 Hz	τ_0	795 ns
γ	8.06×10^6 s^{-1}	$\tau = 2\frac{L}{R}$	248 ns
f_d	1.082×10^6 Hz	τ_d	924.3 ns

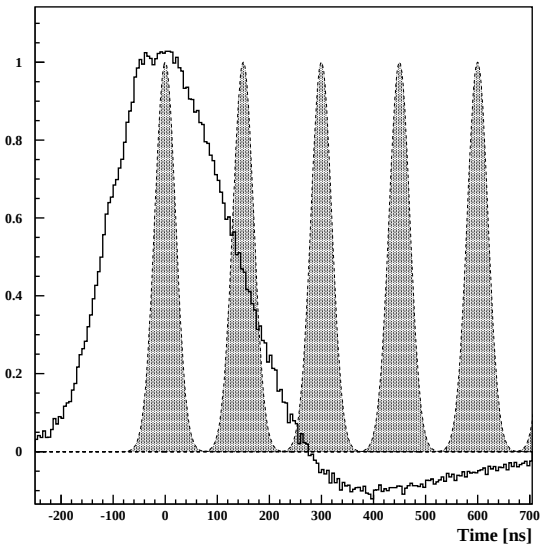

FIG. 51: The trace is a sample kicker current pulse from one of the three kicker circuits. The periodic pulses provide a schematic representation of the unmodified muon bunch intensity during the first few turns. The vertical axis is in arbitrary units.

a. Kicker R&D

There are two issues that we will address for the new experiment: The cooling issue mentioned above; and the need to provide a larger kick. The former has some challenges, because

of the instantaneous heating from rapid pulsing, but some scheme of forced circulation of the oil with a heat exchanger or radiator should be adequate.

More difficult is increasing the peak current of the kicker pulse, which is limited by the inductance of the circuit, as can be seen from Eq. (B5). In the kicker design, great care was taken to reduce all inductances, and a peak current of $\sim$ 4000 A was obtained. Any significant reduction in inductance would increase the peak current, so we have looked at all aspects of the kicker pulse-forming network.

The simplest step that could be taken is to halve the length of the kicker plate. This would require that the number of pulse-forming networks would have to be doubled, but that would be a small price to pay for significantly more stored muons. A full-scale straight kicker prototype was built for E821, and is still intact.

We are now planning to ship the prototype kicker to Fermilab to conduct the *half-kicker* test. The kicker prototype will be setup in the old pbar kicker area in the Wilson Hall basement which contains all the necessary infrastructure and is no longer in use. After cleaning and re-assembly, the baseline parameters of the kicker will be measured, and compared to the E821 performance. Then the magnet will be removed from the vacuum chamber, the length of the plates will be reduced by a factor of two, and re-installed into the vacuum chamber. The kicker parameters will then be re-measured to determine if the half-kicker scheme is indeed a feasible option.

The R&D program will be carried out by Fermilab PPD scientists led by B. Casey including part time PPD technical support. Fermilab is also actively recruiting a post doc to lead this effort as a well defined hardware project. Retired Brookhaven technician/engineer Dave Warburton, who originally worked on the $(g-2)$ kicker system has agreed in principle to join the effort as a consultant, especially to help in the moving and initial set-up at Fermilab. His participation will require support from the Laboratory, both for travel and salary. Roberts, who led the BNL kicker team and worked closely with Warburton will also be involved in this test.

The arrangement of the kicker conductors is less than optimal. Eddy currents in the vacuum chamber above and below the kicker plates reduce the effective field seen by the muon beam, and in the present design the field is highest at the edge of the aperture where there are fewer muons. We would also like to explore the possibility of different conductor geometries, which might significantly improve the kicker field strength at the center of the

aperture. Significant expertise in OPERA exists at Fermilab, and preliminary discussions have been held with Chris Jensen of the accelerator department about a different geometry.

b. Geant4-based simulations of injection and storage

A detailed full Geant4 simulation of the entire $g-2$ storage ring has been developed at Boston University that models the entire chain of transporting the muons through the inflector, the kick, and the final storage of muons on orbit. All known nonuniformities in the storage and inflector magnetic fields are modeled. Additionally, the time dependence of the kicker and quadrupole fields are present. Beam scraping has also been put into the simulation program. The scraping issues discussed in the next sections will be studied to optimize the scraping scheme.

The simulation reproduces the measured collective beam motions of the stored muon distributions. We are working to reproduce and understand the storage process itself: there are many interactions between inflector, quadrupole, and kicker settings that control the final stored muon distributions. We aim to reproduce the full end-to-end muon dynamics in E821, and seek ways to improve the stored muon fraction. The simulation will be a powerful tool in supporting both the kicker and open-ended inflector R&D programs. The simulation is installed on $g-2$ computers at Fermilab and is now the basis for all future simulation work.

4. Beam scraping after injection

One of the systematic errors which must be improved in the new experiment comes from muon losses out of the storage ring which result from processes other than muon decay. In E821 we reduced these losses by scraping off particles on the edge of the storage volume. Scraping is defined as the creation of a gap of several mm between the beam and the collimators that will either eliminate altogether or drastically reduce particle losses during data collection time. This was achieved by asymmetrically powering the electrostatic quadrupoles during and after injection for 10-15 μs and scraping the beam on collimators placed around the ring. This asymmetry caused the beam to be lifted and moved sideways during this scraping time. At the end of the scraping period, the beam was returned to the

equilibrium orbit with a 5 μs time constant. While losses were reduced from 0.6% per muon lifetime in the ring with no scraping to 0.2% with scraping, we will need to do better in the new experiment.

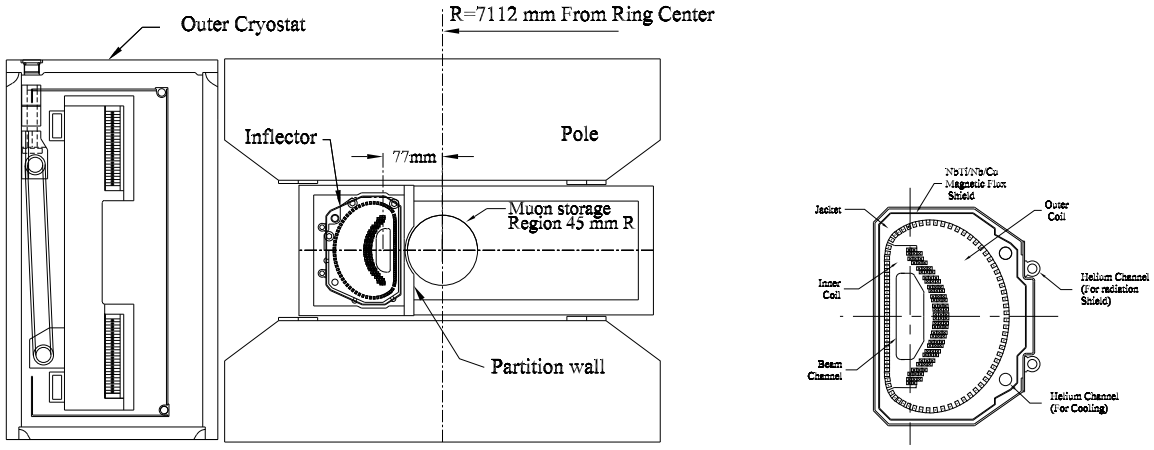

(a) (b)

FIG. 52: (a) The geometry of the inflector exit and the muon storage volume. (b) The cross section of the inflector.

Because of the small inflector size relative to the storage volume, shown in Fig. 52, the phase space in the ring is not uniformly filled. This causes the bunched beam to oscillate coherently both vertically and horizontally in the storage ring. For a detector at a fixed point in azimuth, the apparent radial motion of the beam is the difference frequency between the cyclotron frequency and the horizontal betatron frequency given in Eq. B1. The inflector image is re-formed every betatron wavelength, so that this "waist" in the beam also moves around the ring with the difference frequency between the the cyclotron frequency and twice the radial (vertical) betatron frequency. Since the detector acceptance depends on the radial position of the muon when it decays, the coherent radial betatron oscillations (CBO) amplitude-modulate the time spectrum. The modulation effect decreases in the time due to the "natural" chromaticity of the betatron oscillations, which slightly mix up phases of the particle oscillations. In E821 we measured a decoherence time of about 100 μs for the CBO, and the muon lifetime was 64.4 μs .

In the new experiment we wish to reduce the CBO effects, and to improve the scraping of the beam. Two approaches to reduce the coherent betatron motion and scrape the beam

have been proposed:

1. Using a RF dipole field during the time immediately after injection to first drive the coherent betatron oscillations to scrape the beam, and then to reverse the phase to damp the CBO. This technique would get rid of the main CBO but not the "waist" motion in the beam.

2. A scheme which causes a fast phase mixing in the betatron tune through the introduction into the machine lattice of a nonlinear focusing element such as an octupole. Preliminary studies indicate that the CBO modulation can be minimized by applying this field during less than a hundred turns after injection. This will also serve the purpose of scraping the beam simultaneously with the CBO decoherence.

5. Oscillating Dipole Method of Scraping

In E821 we have estimated the horizontal CBO amplitude at injection both directly and indirectly[141]. The first method involved the fiber beam monitors (see Fig. 53) which consist of eight 0.5 mm diameter scintillating fibers which are inserted into the beam to measure the profile. The signal from a single vertical and single horizontal fiber are shown in Fig. 54 where the beam motion across the fiber is clearly seen. The measured CBO amplitude was found to $\simeq 7$ mm with a frequency $\omega_{CBO} = \omega_C(1 - \sqrt{1-n}) \simeq 470$ KHz.

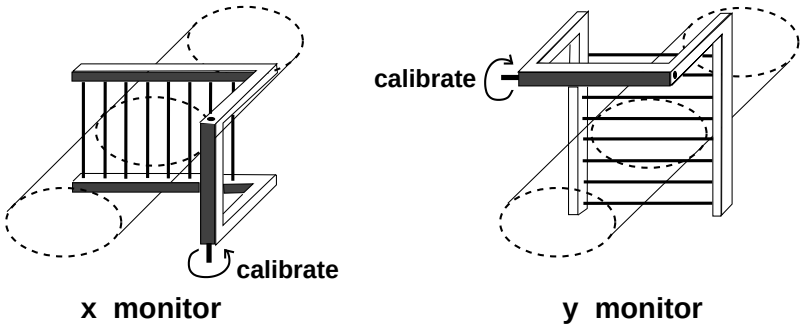

FIG. 53: A sketch of the x and y fiber beam monitors. The fibers are 0.5 mm in diameter. For calibration, the entire "harp" rotates into the beam so that all fibers see the same beam intensity.

This beam CBO manifested itself, among other ways, as a modulation of the number of detected positron by the electromagnetic calorimeters with an amplitude of $\simeq 1\%$. Monte

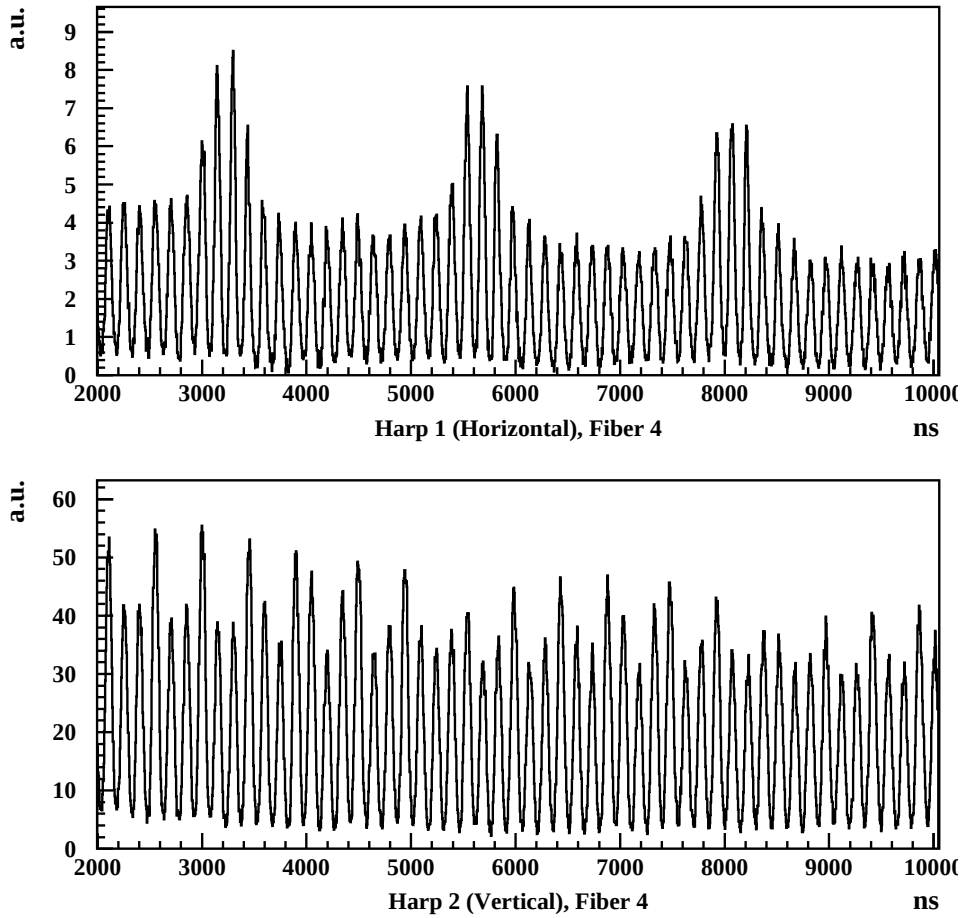

FIG. 54: The phototube output from a single x and y fiber. The CBO frequency (horizontal) and VW frequency (vertical) are clearly seen (see Table XVII).

Carlo studies showed that an amplitude of $\simeq 7$ mm for the CBO would cause that modulation amplitude. Vertically the CBO amplitude is much smaller but still visible from the data at early times. With similar beam injection conditions the CBO has a well defined frequency, amplitude and phase. We propose to use this fact to both scrape the beam and eliminate the horizontal and vertical CBO of the beam due to the motion of the beam center.

This proposal uses a set of four plates, with $ell = 1$ m long azimuthally and placed in the configuration of the quadrupole plates in the g-2 ring. We will then apply a voltage difference between the opposite plates with a frequency equal to the horizontal (horizontal plates) and vertical (vertical plates) CBO. For scraping the beam we will apply the voltage in phase with the beam CBO phase to increase the CBO amplitude. To eliminate the CBO the phase will be opposite. To estimate the voltage needed we will consider here the horizontal

CBO, but the same method can be applied for the vertical CBO. The functional form of the horizontal dipole electric field, $E_x(t)$, is

$$E_x(t) = E_{x0}\, f(s)\, \cos\left(\omega_{CBO} t + \theta_0\right), \tag{B6}$$

where $f(s) = 1$ for the space between the plates and 0 outside them. We take as $t = 0$ the time the muon beams enter the electric plates for the first time. Then the equation of motion can be written as

$$\ddot{x} + \omega_C(1-n)x = \omega_C^2 R \left(\frac{eE_{x0}}{\beta B}\right) f(t) \cos(\omega_C(1-\sqrt{1-n}t + \theta_0)) \tag{B7}$$

where $\beta \equiv v/c$ and

$$f(t) = \begin{cases} 1, \ Tq < t < \left(Tq + \frac{l}{\nu}\right), \ q = 0, 1, \cdots N \\ 0, \quad \text{otherwise} \end{cases} \tag{B8}$$

Where $T \simeq 149$ ns, the cyclotron period of the ring. The exact solution of equation 3 with $f(t)$ given by Eq. B8 is

$$x = a(t)e^{i\omega_x t} + a^*(t)e^{-i\omega_x t} \tag{B9}$$

$$a = a_0 - ie^{i\theta_0} \frac{N+1}{4\sqrt{1-n}} \left(\frac{E_{x0} l}{\beta B}\right) \left[1 + \frac{e^{i2\theta_0}[1 - e^{-i2\omega_C(1-\sqrt{1-n}T(N+1))}]}{N+1[1 - e^{-i2\omega_C(1-\sqrt{1-n})T]}}\right]. \tag{B10}$$

where $a_0 = (x_{max}/2)e^{i\alpha}$ corresponds to $t = 0$ and defines the electric field phase θ_0. After $N+1$ turns we get Eq. B10 which for large $N > 10$ simplifies to

$$a = a_0 - ie^{i\theta_0} \frac{N+1}{4\sqrt{1-n}} \left(\frac{E_{x0} l}{\beta B}\right), \tag{B11}$$

where B is the storage ring dipole magnetic field. For $x_{max} = 0.7$ mm, $N = 60$ (i.e. about $10\,\mu$s), $n = 0.142$, and $B = 1.45$ T we need $E_{x0} \simeq 0.9$ kV/cm at the CBO frequency of $\simeq 470$ KHz. For a plate separation of 10 cm it means a voltage amplitude of $\simeq 9$ KV across the opposite plates horizontally driven at 470KHz, which is quite reasonable.

The expected beam losses after scraping the beam are going to be dominated by the vertical scraping since it is expected that horizontally we wouldn't need to scrape more than $\simeq 7$ mm oscillation of the beam at injection. Horizontally we would therefore just wait of the order of 5μs for the beam to scrape off the collimators after which we would apply the voltage estimated above to eliminate it. Vertically we would need to apply a voltage for about $5\,\mu$s after injection in phase with the natural one so that we induce an overall vertical

oscillation of the order of 5 mm after which we will flip the sign of the phase to eliminate it. The total beam losses induced by this method of scraping for a beam gap of 5 mm vertically and 7 mm horizontally are estimated to be less than 20%.

6. Pulsed Octupole Method to Remove the CBO

This method effects a fast phase mixing by an introduction of a nonlinear focusing element in the machine lattice[142]. The nonlinearity induces a dependence of betatron tunes on amplitudes of transverse oscillations ($\frac{\delta Q}{\delta a^2}$).[143] The CBO modulation could be minimized during a few tens of turns in the storage ring. Using a time (up to 100 turns) to apply a pulsed closed orbit distortion can make the CBO vanish while simultaneously scraping the beam.

The rectangular symmetry of the vacuum chamber permits one to install an octupole coil inside the vacuum chamber. The coil can be wound around an area of 6 cm radius as shown in Fig. 55, while the beam has $r = 4.5$ cm. In a preliminary design, a coil length of 2 m was chosen, located in a section free from electrostatic focusing and kickers. The field lines have been calculated by the computer code MERMAID.[144]

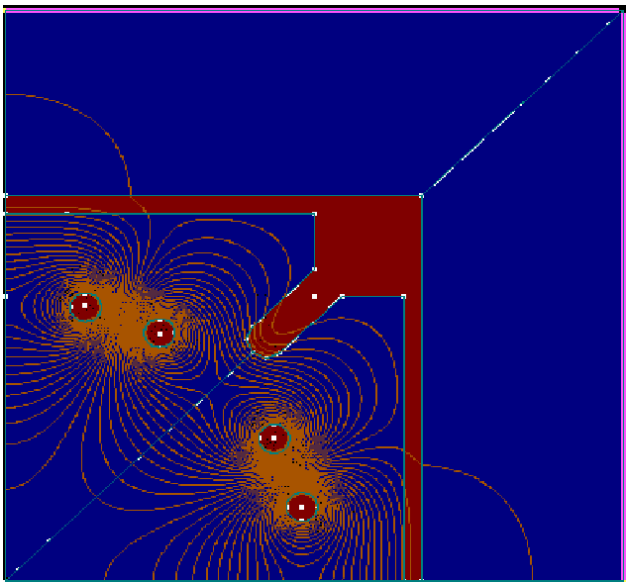

FIG. 55: Octupole coil in vacuum chamber and magnetic field lines

Particle tracking was done with electrostatic focusing of the $g-2$ ring for different octupole field strengths, and for several residual horizontal angles after the kicker. The RING code

was used for the tracking,[145] for 10000 particles. The initial phase-space distributions were assumed to be uniform in both the vertical and radial directions. The muons were tracked for 100 turns. The initial and stored phase space distributions are shown in Figs. 56.

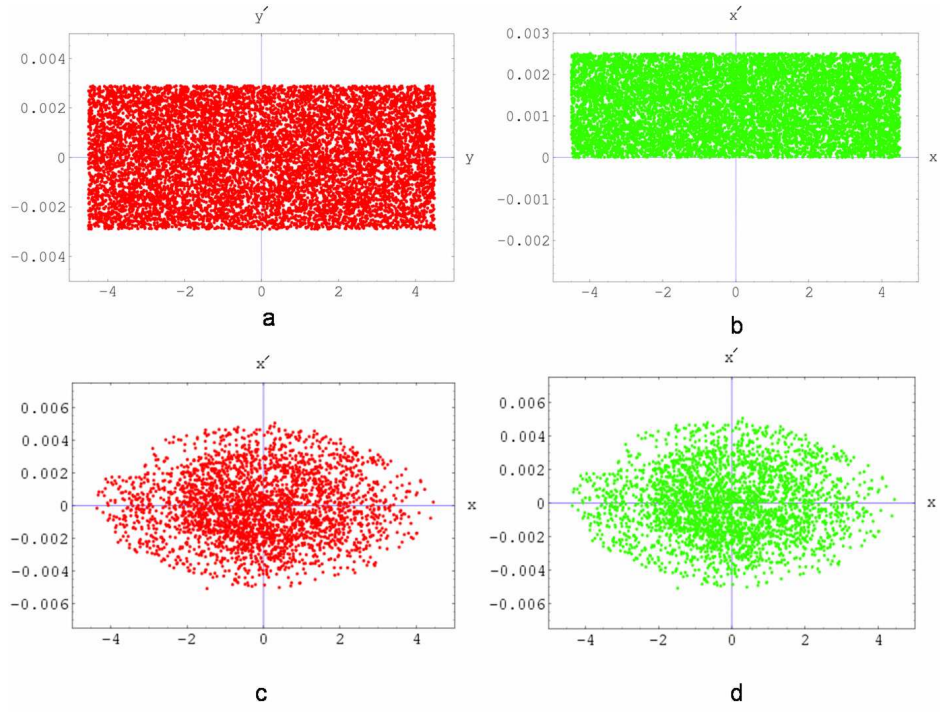

FIG. 56: Initial and final phase distributions. (a) Initial vertical distribution. (b) Initial radial distribution. (c) Stored radial distribution. (d) Stored radial distribution.

During tracking, the amplitude of the CBO was evaluated after each turn by the expression:

$$A = \sqrt{\frac{(1+\alpha_x^2)\langle x\rangle^2 + 2\alpha_x\beta_x\langle x\rangle\langle x\prime\rangle + \beta_x^2\langle x\prime\rangle^2}{\beta_x} + \frac{(1+\alpha_y^2)\langle y\rangle^2 + 2\alpha_y\beta_y\langle y\rangle\langle y\prime\rangle + \beta_y^2\langle y\prime\rangle^2}{\beta_y}}, \tag{B12}$$

where $\langle x\rangle\langle x\prime\rangle, \langle x\rangle^2, \langle x\rangle\langle x\prime\rangle, \langle x\rangle^2$ are average over the ensemble coordinates and angles and their squared values. α and β — are corresponding Twiss parameters.

Fig. 57 shows the CBO amplitude versus turn number N, for different octupole strengths. One can see an octupole gradient of 0.8 G/cm^2 greatly reduces CBO amplitude by the 30-th turn. The tracking shows that neither this reduction factor, nor the amplitude beating after the octupole is removed, depend on the residual angle. About 50% of the beam is lost using this method.

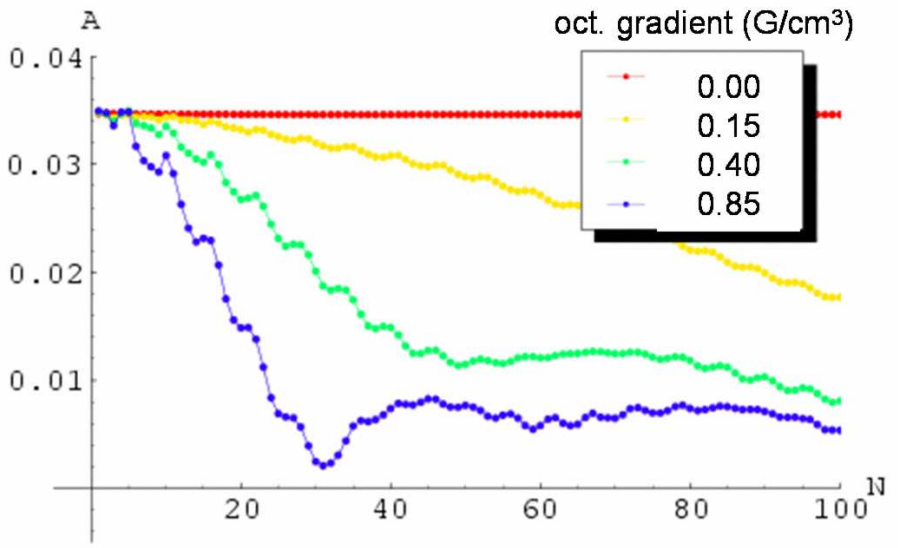

FIG. 57: Behavior of the CBO amplitude as a function of turn number and octupole strength.

Calculations show that to provide the optimal octupole gradient of 0.8 G/cm^2, a pulse current of 2.5 kA is needed. This will need to be a pulsed octupole, since the octupole field, as well as any magnetic fields induced by eddy currents in the vacuum chamber or other conductors nearby, must be negligible before data collection can begin. Simulations used both a square (ideal) current pulse and a sinusoidal one, and little difference was found compared to the rectangular one. The parameters of an LCR pulse generator are, Voltage V=1.3 kV, Capacitance C$\approx 1\mu F$, Period T$\approx$ 10 μsec. The octupole coil can be made from water-cooled copper pipe of 1 cm in diameter. The energy dissipated in such a coil per pulse is about 1 J.

An alternative electrostatic octupole is able to do the same, but its realization looks from practical point of view much more difficult, because of the symmetry imposed by the trolley rails which go all the way around inside the vacuum chamber with four-fold symmetry.

APPENDIX C: NEW CALORIMETERS

The basic material design requirements for a new calorimeter are largely unchanged; it must be dense, fast, and non-ferromagnetic. Additionally, the new calorimeter must be segmented transversely with respect to the incoming positron, so that simultaneous events can be distinguished 4 out of 5 times. Building new Pb/SciFi calorimeters with fibers running longitudinally (i.e., rotated by 90 degrees) is one possible solution. The downstream face of the detector would be a fiber / lead grid that could be readout in small and independent segments. Members of our Collaboration have built detectors of this type in the past, with incoming photons nearly co-linear with the fiber direction. This re-oriented Pb/SciFi option is attractive in principle, but there are two drawbacks. First, the downstream space is limited by the existing vacuum chamber structures. A shorter detector would be required to allow for space for the readout system. Second, simple simulations using $\rho_M = 2.5$ cm, which corresponds to existing Pb/SciFi construction template, and the requirement that showers be separated by at least $2\rho_M$, indicate a pileup separation factor of no better than 3 (the simulation uses the actual distribution of positrons on the calorimeter face, see Fig. 58). The goal of the new detectors is to separate simultaneous showers by a factor of about 5. To do so requires the detector to have a smaller Moliere radius.

We have designed and built a detector made of alternating layers of 0.5-mm thick tungsten (W) plate and 0.5-mm-diameter plastic scintillator fiber ribbons. A NIM paper has been published reporting the experience with construction and the performance in beam tests [14]. Based on these tests, and since the time of the original proposal submission to Fermilab, we have produced a much 10-times larger, essentially full scale, prototype, which is currently being prepared for test beam time at Fermilab in May 2010. We briefly summarize some of the interesting findings from our studies.

The prototype module is $4 \times 6 \times 17$ cm^3. The calculated radiation length is 0.69 cm and the Moliere radius is 1.7 cm. Both are much smaller than the Pb/SciFi design used in E821. The fiber ribbons are oriented vertically so that the positrons, which are curling inward, must cross W layers and initiate showers. The full sized detector will be made as one monolithic structure with dimension 15 cm high by 21-cm radial. The 11-cm depth represents more than 15 X_0. Fibers will be either gathered into small bundles on the downstream side forming individual "segments" or a direct array of lightguide couplers will be attached to provide

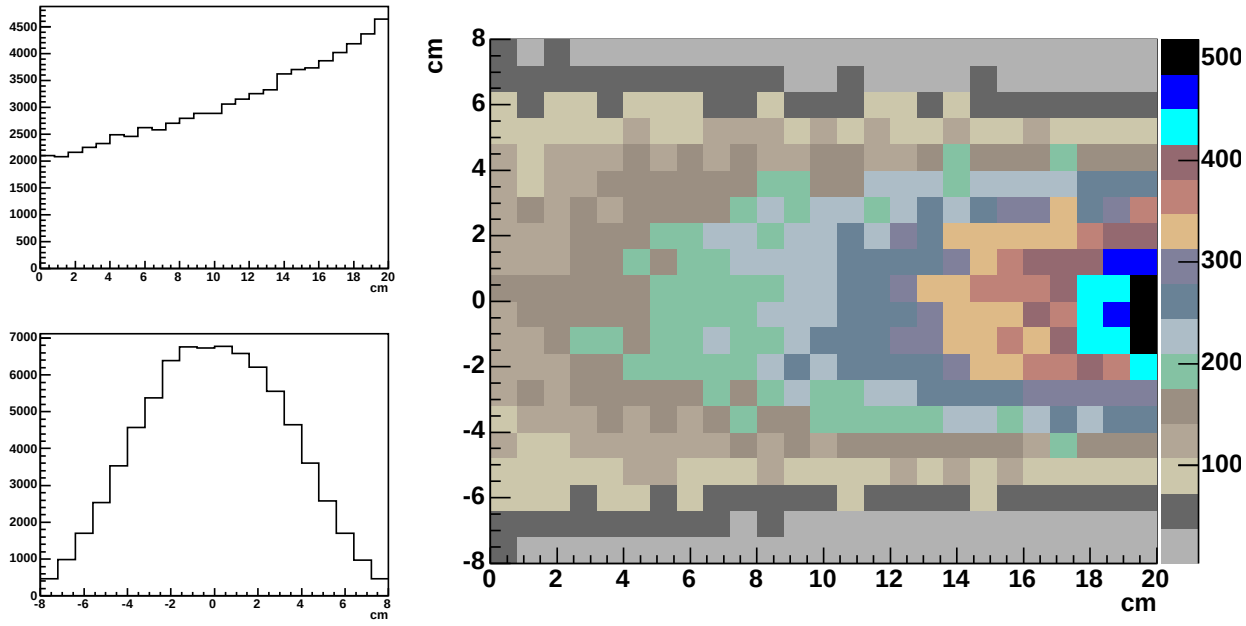

FIG. 58: Right panel: Hit position of positrons on calorimeter front face from from Geant4 simulation. Top left panel: radial distribution; storage ring edge is at large x values. Bottom left: vertical distribution.

the segmentation. At the present time, we are planning on using a 5×7 array of 3×3 cm^2 segments, although the readout can easily be changed later since the detector is made as one large monolithic structure.

The prototype is shown in Fig. 59a, and a full conceptual design array of (here with only 4×4 cm^2 readout modules) is shown in Fig. 59b; 24 such arrays are required for the proposed muon $(g-2)$ experiment.

We have developed a simple and effective assembly procedure for these modules that will assure consistent uniformity of the completed modules. Quotes [146, 147] have been obtained for the fiber ribbons and flat tungsten plates, required for the full production of 24 calorimeter modules. The total cost of the material components for the calorimeter modules is approximately \$0.5M; construction is roughly 1 technician-year.

The prototype used 0.5-mm diameter BCF-20, "green-emitting" scintillating fibers obtained from Saint-Gobain Crystals [146]. These fibers were conveniently available owing to a large production for an independent project. They arrived as 12-cm wide by 17.5-cm long "ribbons." Each ribbon came as a self-contained structure with the individual 0.5-mm fibers

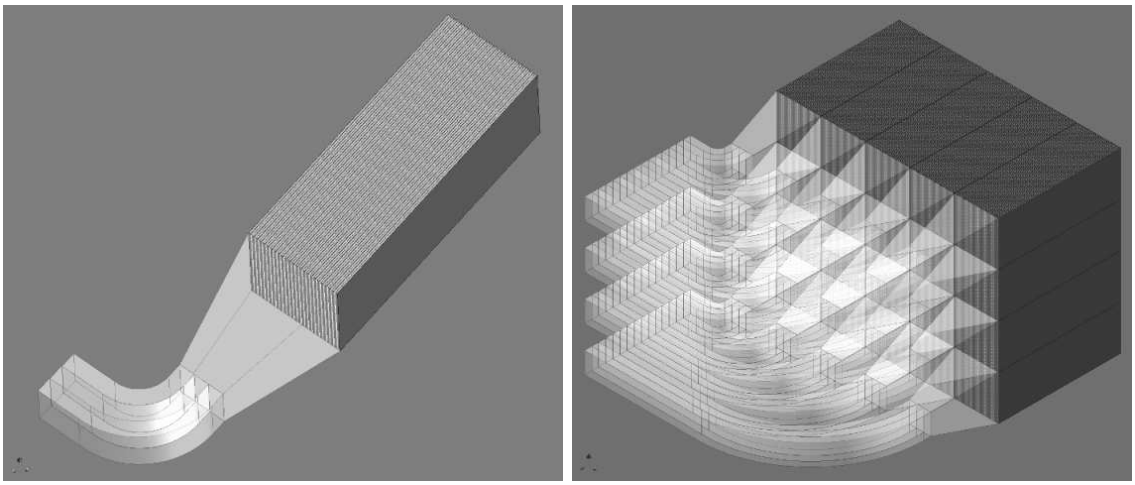

(a)Prototype module and guide (b)Proposed array of 20 modules

FIG. 59: a) Prototype $4 \times 6 \times 17$ cm^3 module and b) Array sketched with only twenty 4×4 cm^2 readout modules to illustrate how lightguides might curl toward the $(g-2)$ storage ring center if conventional PMTs are used for the readout.

held adjacent by a coating of a polyurethane-acrylic blend cement. We split each ribbon into two 6-cm wide strips to match the tungsten plate widths. The fibers are coated with a $10-15$ μm thick white extra mural absorber for better light transmission. The new prototype, and the final production modules, uses BCF-10 "blue" fibers, which better match the quantum efficiency of the readout device.

The W/SciFi detector was first tested at the Paul Scherrer Institut (PSI) and at the Meson Test Beam at Fermilab. The focus of the test beam measurements was on calorimeter linearity and energy resolution. While neither beamline was optimized to provide a small momentum resolution or spot size, sufficient performance information was obtained to compare measurement to Geant4 based Monte Carlo simulations.

The typical $(g-2)$ energy threshold for including events is $1.8-2$ GeV; positrons are only accepted above this threshold. A resolution of $\sim 10\%$ (defined as σ/E for a simple Gaussian fit) would give an acceptable performance for this threshold in a future $(g-2)$ experiment. The response of the prototype tungsten detector is shown in Fig. 60 for 2 GeV electrons impacting at 5 degrees with respect to the fiber axis. An entrance cut is made using beamline wire chamber information to select the central 15 mm by 30 mm (width by height) of the 40- by 60-mm detector face. Even with no corrections for leakage into side detectors, or adjustments for sub-optimal light collection, or beam momentum uncertainty,

the resolution at $10.1 \pm 0.3\%$ meets the experimental goal.

Our goal is to understand the intrinsic sampling resolution of this detector and compare it to simulation. While the stochastic term is mainly determined by the sampling fluctuations intrinsic to the active-to-absorber material ratio and the effective layer thickness, additional contributions enter from photo-statistics. A 5% contribution exists from photo-statistics, because the measured photoelectron (pe) yield is 400 pe/GeV. This is a smaller light yield than we would expect had the lightguide been better matched in area to the photomultiplier tube and if blue fibers were used instead of green (higher quantum efficiency). Two factors that scale with energy contribute to resolution degradation—the transverse leakage, and the momentum uncertainty of the test beam. The leakage can be explored with data cuts and simulation; the $\Delta P/P$ is unknown but estimated to be a few percent. In Fig. 61, we plot the FNAL data fit to

$$\frac{\sigma(E)}{E} = \sqrt{\frac{A^2 + \Delta_{pe}^2}{E} + B^2}. \tag{C1}$$

Here $A/\sqrt{E}$ represents the intrinsic sampling term, $\Delta_{pe}/\sqrt{E}$ is the photo-statistics uncertainty, and B is a linear term. The term Δ_{pe} is fixed at 5% and E is given in GeV. The upper curve is a fit based on data where a 25 mm "wide cut" in the entrance width of the beam was used, while the lower curve is a fit based on a 5 mm "narrow cut." The change affects both the sampling and the constant term as they are not easily separable, given the statistics. The narrow cut result minimizes, but does not eliminate, the leakage, resulting in $A_{meas} = 11.8 \pm 1.1\%$ and $B_{meas} = 3.7 \pm 1.3\%$ for the stochastic and constant terms, respectively.

The sampling fluctuation component can be predicted using a complete Geant4 model. A plot of this resolution versus energy for simulated electrons impacting on the module center at a 5-degree angle is shown in Fig. 62. Three curves are presented representing a high-statistics "pencil beam" with a 1 mm spot size in both dimensions, as well a separate simulation with data-like cuts of 5- and 25-mm entrance widths, which match the narrow and wide definitions for the data. The most appropriate comparison to data is the narrow cut, which yields $A_{sim} = 10.6 \pm 0.8\%$ and $B_{sim} = 2.9 \pm 1.1\%$ for the stochastic and constant terms, respectively. The B term is representative of the leakage, since no $\Delta P/P$ uncertainty contributes for Monte Carlo. If we deconvolute the leakage contribution from the B term in the data, a $\Delta P/P$ of $\approx 2.3\%$ is implied, which is not unreasonable.

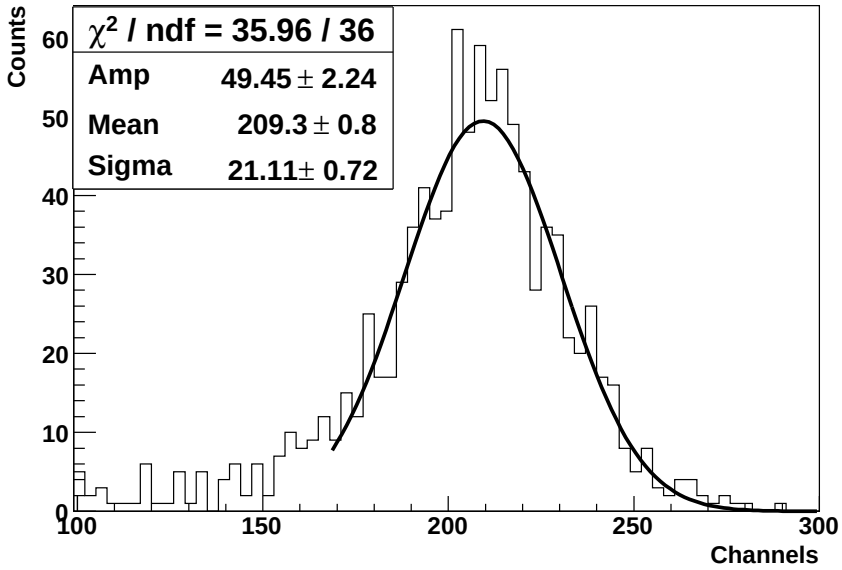

FIG. 60: Example raw W/SciFi detector ADC data for a 2 GeV electron beam impacting at a 5 degree incidence. A modest containment cut of 15 mm width is made.

The simulation is, not surprisingly, somewhat better than the actual prototype—$A_{sim} = 10.6 \pm 0.8\%$ vs. $A_{meas} = 11.8 \pm 1.1\%$. Detector construction imperfections can contribute, as would non-uniform light collection in the guide. However, to explore this comparison more completely requires a larger test module with improved readout and a better controlled test beam environment. Note, that we carefully checked the Geant4 cut parameters, but found no dependence on them that altered our results.

Based on these studies, we built a $15 \times 15 \times 11$ cm^3 module with 25 individual readout lightguides. It will be ready for test beam measurements schedule for May 2010 in the MTest beam at Fermilab. We are also working with an updated Geant4 model, simulating the new prototype, with its 3×3 cm^2 readouts. A representation of the geometry is shown in Fig. 63 and a top-down view of a shower in this material is shown in Fig. 64. Additionally, we have carried out a comprehensive clad-fiber and lightguide simulation and optimization program and built and measured several different styles of guides for optimum and uniform light collection. The latter project served as the Senor Thesis for an Illinois undergraduate. The readout plan for the test module is to use a set of Electron Tube 29-mm (1-1/8 in) PMTs whose basic characteristics are understood. We used these in the muon lifetime experiment MuLan at PSI, which is now complete. The similar 10-stage XP-2972 from

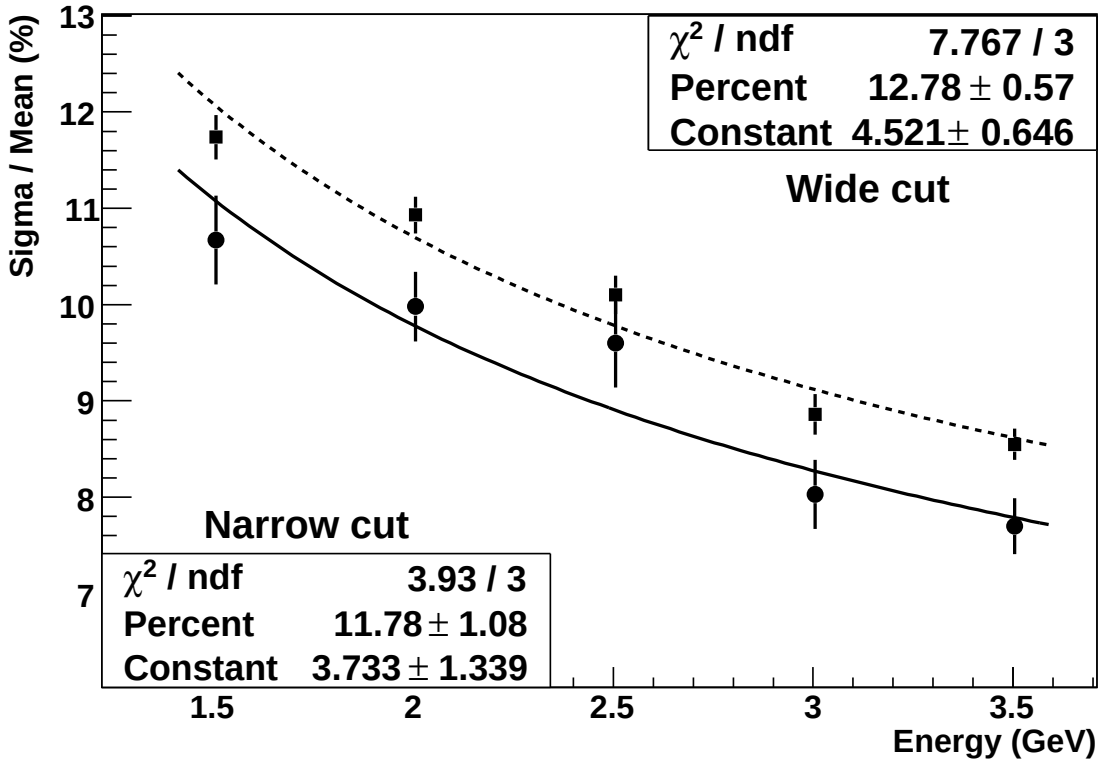

FIG. 61: Measured resolution at 5-degree impact angle versus energy. The upper curve (dotted) is a fit to data obtained requiring a 25-mm-wide entrance cut. The lower curve (solid) is a fit to data obtained using a 5-mm-wide entrance cut. The"Percent" term represents the intrinsic sampling term (A in the text); a 5% photo-statistics stochastic term has been removed in the fit function.

Photonis is a good candidate for the New $g-2$ Experiment because of the high light yield from the calorimeter modules. Both tubes were carefully evaluated by us and feature similar important characteristics: low noise, high gain, no detectable after-pulses. We will have to design a robust, rate-dependent base as the initial rate of up to a few MHz is higher than what can be comfortably handled by the stock resistor divider network in the simplest provided commercial bases. For E821, a gated base was developed that allowed the PMT to be "turned off" during injection and turned back on within 1 μs after injection. Depending on the level of hadronic flash, we may need to incorporate this gating feature—therefore, we will plan to do so in our design.

The rapid development of silicon photomultiplier tubes (SiPMs) and their packaging into relatively large arrays provides a very attractive option for $g-2$.These SiPMs are very fast

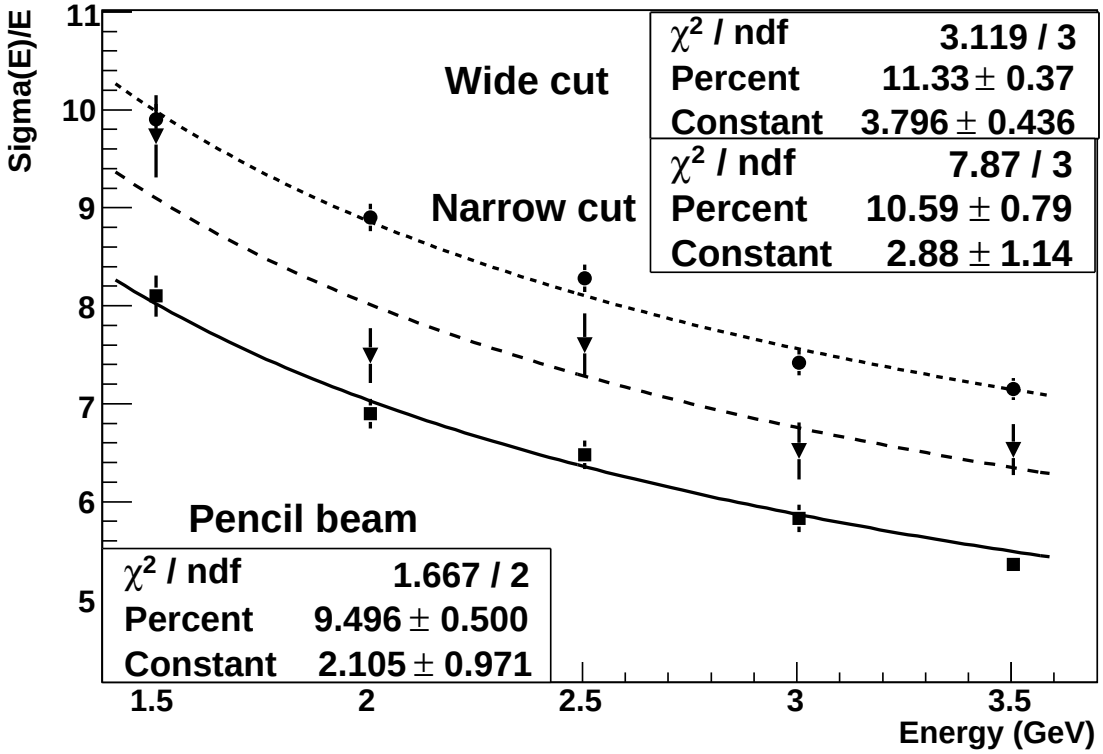

FIG. 62: Fits to resolution versus energy in the central module of an array of W/SciFi modules. Three entrance width cuts are imposed: 25 mm (dotted), 5 mm (dashed), and 1 mm "pencil" (solid).

and they can be mounted onboard, in the magnetic field, thus avoiding the costly and clumsy development of lightguides and external housing. We have acquired two 6×6 mm^2 SiPM arrays from Hamamatsu for testing purposes and we have developed a lightguide that tapers from the 3×3 cm^2 back-face area to the small SiPM device. One or two of these special readout channels will be includes in the new prototype array. A special development of a waveform digitizer board, optimized for SiPMs by having the low voltage controller onboard and fed through the signal line to the SiPM, has been made by Fermilab physicist Paul Rubinov. Paul has kindly agreed to help us with this development to see if the SiPM readout might work for the whole $g-2$ experiment.

One new detector has been added to the planned system since the submission of the original proposal. It is a fine segmented scintillator hodoscope to be mounted on the front face of each calorimeter. The E821 experiment did have such systems on most calorimeters

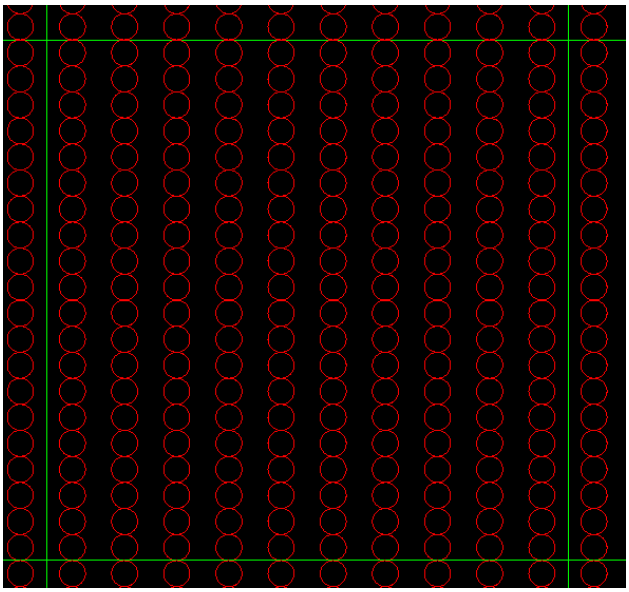

FIG. 63: Geant4 representation of the fibers in the W/SciFi calorimeter. The green lines are spaced 1 cm apart. The simulation contains the fibers shown in the red circles, as well as the tungsten plates in the large gaps and glue in the remaining space around the fibers.

and they proved to be invaluable in making muon loss monitors and in establishing the beam vertical profile. Originally, the plan was to have an "in air" straw system, as part of the overall traceback chambers; however we will not put traceback chambers on all stations and the hodoscope offers a less costly and time-wise, faster, signal to establish a trigger for the straw timing and for possible use in a new muon loss monitor. These scintillator strips will very likely be read out with onboard SiPMs, which are ideal for such a problem. The strips can be seen in Fig. /reffig:shower, just in front of the calorimeter block.

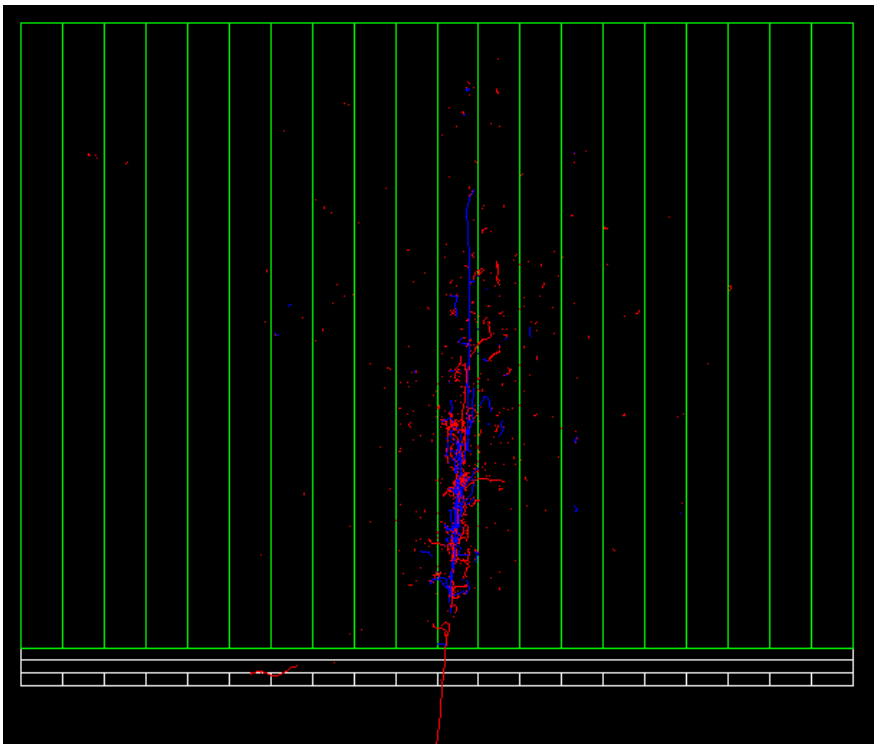

FIG. 64: Simulation using Geant4 of a 2 GeV electron striking the W/SciFi calorimeter at 5-degrees. The electron first passes through a scintillating hodoscope, then showers in the calorimeter into photons (here invisible), electrons (represented by red tracks) and positrons (the blue tracks). The green parallel lines are spaced 1 cm apart and serve to set the scale for the size of the shower in the calorimeter.